2020

Enhancing the Sensing Capability for An Optical Feedback Interferometer

Yuxi Ruan
University of Wollongong

UNIVERSITY
OF WOLLONGONG
AUSTRALIA

Enhancing the Sensing Capability for An Optical Feedback Interferometer

Yuxi Ruan

This thesis is presented as part of the requirement for the conferral of the degree:

Doctor of Philosophy

This research has been conducted with the support of the Australian Government Research Training Program Scholarship

University of Wollongong

School of Electrical, Computer and Telecommunications Engineering

March 2020

Abstract

The lasers diodes (LD) experiencing external optical feedback are known to demonstrate complex dynamics, which may give rise to negative effect on the LD performance, e.g., degrading the modulation response characteristics, enhancing laser intensity noise, etc. Meanwhile, such external optical feedback effect in an LD also enables many applications, e.g., a class of laser interferometry, termed optical feedback interferometry (OFI) or self-mixing interferometry (SMI). As a promising non-contact sensing technology, OFI has attracted intensive research in recent decades due to the merits of minimum part-count scheme, low cost in implementation and ease in optical alignment. In general, the LD operates at a steady state if undergoing a weak level optical feedback from the target. Various OFI-based sensing applications have been reported for such weak optical feedback scenario, including measurement of displacement, velocity, vibration, laser related parameters, thickness, mechanical resonance, etc. Recently, OFI based sensing has been extended to other areas, such as imaging, material parameters measurement, near-field microscopy, chaotic radar, acoustic detection, biomedical applications etc. With the increase of the optical feedback level, an LD will leave the steady state and enter other operational states such as period-one (P1) oscillation, multi-periodic oscillation and chaos, and rich dynamics can then be observed. In recent years, LD dynamics have been investigated and found their various potential applications in optical communications, defence and security, and detection. In this thesis, we focus on enhancing the sensing capability of the OFI system through proposal of new physical configurations and investigation on the LD dynamic.

In Chapter 2, a dual-cavity OFI system is investigated to address the issue of sensitivity

degradation associated with an OFI sensing system due to the weak optical feedback of the target. Following the principle of the single-cavity OFI model, a theoretical model for the dual-cavity OFI is derived from the steady state solutions of the dual-cavity L-K equations. A mathematic expression of the signal enhancement is obtained, elaborating how the feedback strength of the control target and the control cavity length influence the enhancement. The results show that the second cavity can effectively improve the sensing sensitivity without any physical changes on the target to be measured.

Chapter 3 presents theoretical analysis on OFI systems by investigating into the validity of both L-K equations and the OFI model. Traditionally, existing OFI model was derived based on an assumption that the system operates in stable state. With the changes of system parameters, an OFI system can leave the steady state, entering other states and exhibits complicated dynamics, which cannot be described by existing OFI model. In order to tackle this problem, we carried out simulations on the behaviours of L-K equations with respect to variations of a set of system parameters. The results are presented as a bifurcation diagram, showing both dynamic states and optical feedback regimes. Base on the bifurcation diagram, the operational state of an OFI can be further classified into five regions. In each of the regions, the OFI signals generated from both L-K equations are simulated and compared with that from the OFI model. Such study on the validity of OFI model and L-K equations provide a guidance on applying appropriate models when designing OFI based sensing system. In this chapter, we also present a new sensing scheme making use of laser dynamics associated with a dual-cavity OFI system to improve the sensing sensitivity. The second cavity is used to control the laser dynamics and ensure the LD operates at P1 state. While operating on P1 state, the laser intensity

exhibits an oscillation with its amplitude modulated by an OFI signal that generated the LD with a single cavity operating at steady state. It is observed that the modulation depth is remarkably larger than the magnitude of the single-cavity OFI signal. This implies that a dual-cavity OFI system is able to produce a sensing signal at much higher signal-to-noise ratio (SNR) in contrast to the single-cavity OFI system. By adjusting the feedback strength, the system can be set to operate at an optimal working point for sensing and measurement. Such a superior characteristic of the dual-cavity OFI enable us to extend the application to a displacement measurement. A new approach to achieve a sub-nanometre scale displacement sensing is also proposed, which is based on a fringe sub-division algorithm that utilizes the high frequency component of the laser intensity signal and a signal processing technique in the time-domain.

In Chapter 4, we presented a novel technique for the measurement of the linewidth enhancement (α) factor using the relaxation oscillation (RO) frequency of the LD. Based on the fact that the RO frequency of a laser can be changed by external optical feedback, we investigated the relation between the RO frequency and α factor and presented three methods for the measurement of α. In the proposed methods, α can be determined by the RO frequencies only, without needing to know any other internal or external parameters associated with the LD. The methods do not require the external target to move in a symmetric reciprocate manner and they do not rely on analysis the OFI waveform. As the RO can be observed in many types of lasers, the proposed methods are not limited to semiconductor lasers.

Acknowledgments

"A time to build" was my old high school motto, it often reminds me to make full use of every single moment. My four years PhD study has been a challenging, exciting and fruitful journey. Of course, this journey will not be possible without the support and help from many people. First and foremost, praises and thanks to my parents Sunny and Boyang for their unconditional love and care. I also would like to express my gratitude to Professor. Jiangtao Xi and Associate Professor Qinghua Guo for their advises. It is hard to find the rights words to express my thankfulness to Dr. Bin Liu, who provides invaluable guidance throughout my PhD study. My thanks also extended to Bairun Nie and Zhuqiu Chen, for the passion and willingness they have demonstrated when we worked on the research projects.

During the PhD study, apart from my research, I had the opportunities for being a student representative to various student association and university governance bodies. These experiences enhanced my management and leadership skills, also I have meet many great people and made lots of friends. Chuhao Liu, Lingzhi Kang, Yannan Li, Jianye Huang, Yiwen Mao, Yiwei Zhang, and Jin Zhao, give their encouragements, kindness and supports in various circumstances. People come and go but you have left footprint in my heart. Last not the least, Qihao Wu, memories of sad and joy can fade, but your character is seldom forgotten. Good friends are hard to find, harder to leave, and impossible to forget. Looking back these four years, "They were good days, they have been good days".

The famous painting "The Great Wave off Kanagawa" has many interpretations, the one

I most align with, it shows fragile of lives in front of formidable nature. It may due to our ignorance and arrogance, we are seeing and experiencing the disasters that we have never seen before. During the time of writing this thesis, in Australia, the bushfire has burned roughly 25.5 million acres and over 1.25 billion animals have died. The Coronavirus has spread to over 160 countries and more than 170,000 people have been infected. So far, no vaccines has been discovered. These alerts make us to reflect, where our future lies ahead. The world will be a better place, only if we start to be respectful, be generous and be kind. I have always believe there is an almighty upon us, show us hope and mercy in the desperate time. In this difficult moment, May the Almighty help us all, save us all.

Publications

Journals:

[J1]. **Y. Ruan**, B. Liu, Y. Yu, J. Xi, Q. Guo, and J. Tong, "High sensitive sensing by a laser diode with dual optical feedback operating at period-one oscillation," ***Applied Physics Letters,*** vol. 115, no. 1, p. 011102, 2019. [IF: 3.521; JCR: Q1]

[J2]. **Y. Ruan**, B. Liu, Y. Yu, J. Xi, Q. Guo, and J. Tong, "Improving Measurement Sensitivity for a Displacement Sensor Based on Self-Mixing Effect", ***IEEE Photonics Journal***, vol. 10, no. 6, pp. 1-10, 2018. [IF: 2.729; JCR: Q2]

[J3]. **Y. Ruan**, B. Liu, Y. Yu, J. Xi, Q. Guo, and J. Tong, "Measuring Linewidth Enhancement Factor by Relaxation Oscillation Frequency in a Laser with Optical Feedback", ***Sensors,*** vol. 18, no. 11, p. 4004, 2018. [IF: 3.031; JCR: Q2]

[J4]. B. Nie, **Y. Ruan**, Y. Yu, Q. Guo, J. Xi, and J. Tong, "Period-one Microwave Photonic Sensing by a Laser Diode with Optical Feedback", in ***Journal of Lightwave Technology***, doi: 10.1109/JLT.2020.2993320. [IF: 4.162; JCR: Q1]

[J5]. B. Liu, **Y. Ruan**, Y. Yu, J. Xi, Q. Guo, and J. Tong, "Modeling for optical feedback laser diode operating in period-one oscillation and its application", ***Optics Express,*** vol. 27, no. 4, pp. 4090-4104, 2019. [IF: 3.561; JCR: Q1]

[J6]. B. Liu, **Y. Ruan**, Y. Yu, J. Xi, Q. Guo, J. Tong, and G. Rajan, "Laser Self-Mixing Fiber Bragg Grating Sensor for Acoustic Emission Measurement", ***Sensors,*** vol. 18, no. 6, p. 1956, 2018. [IF: 3.031; JCR: Q2]

[J7]. Q. Guo, **Y. Ruan**, J. Xi, L. Song, X. Zhu, Y. Yu, and J. Tong, "3D shape measurement of moving object with FFT-based spatial matching", ***Optics & Laser Technology,*** vol. 100, pp. 325–331, 2018. [IF: 3.319; JCR: Q1]

[J8]. H. Wang, **Y. Ruan**, Y. Yu, Q. Guo, J. Xi, and J. Tong, "A New Algorithm for Displacement Measurement Using Self-mixing Interferometry with Modulated Injection Current", under revision, submitted to ***IEEE Access***.

International Conferences:

[C1]. **Y. Ruan**, B. Nie, Y. Yu, J. Xi, Q. Guo, J. Tong, and Z. Chen, "Achieving high resolution measurement using laser diode operating at period one", *SPIE Future Sensing Technologies*, 12 December 2019, Tokyo, Japan

[C2]. **Y. Ruan**, B. Nie, Z. Chen, Y. Yu, J. Xi, Q. Guo, and J. Tong, "Sensing using Dynamics of a Laser Diode with Dual-Cavity", *OSA Applications of Lasers for Sensing and Free Space Communications*, 29 September–3 October 2019, Vienna, Austria

[C3]. **Y. Ruan**, B. Liu, J. Xi, Q. Guo, J. Tong, and Y. Yu, "Improve Sensitivity for a Self-Mixing Laser Diode Sensor by Applying a Pre-feedback", *4th International Conference on Sensors Engineering and Electronics Instrumentation Advances,* 19 - 21 September 2018, Amsterdam, The Netherlands

[C4]. **Y. Ruan**, B. Liu, Y. Yu, J. Xi, Q. Guo, and J. Tong, "Alpha Measurement Using Laser Dynamics", *IEEE International Frequency Control Symposium*, 22 - 24 May 2018, Olympic Valley, California, USA

[C5]. H. Wang, **Y. Ruan**, Y. Yu, J. Xi, Q. Guo, and J. Tong, "Effect of windowing on a sensing signal generated by self-mixing interferometry", *SPIE Future Sensing Technologies*, 12 December 2019, Tokyo, Japan

[C6]. B. Nie, **Y. Ruan**, Z. Chen, Y. Yu, Q. Guo, J. Xi, and J. Tong, "State Boundaries in a Laser Diode with Optical Feedback and Its Sensing Application", *OSA*

Applications of Lasers for Sensing and Free Space Communications, 29 September–3 October 2019, Vienna, Austria

[C7]. Z. Chen, **Y. Ruan**, B. Nie, Y. Yu, Q. Guo, J. Xi, and J. Tong, "Measuring Linewidth Enhancement Factor by Laser Dynamics", *OSA Laser Applications Conference*, 29 September–3 October 2019, Vienna, Austria

[C8]. B. Liu, **Y. Ruan**, Y. Yu, and J. Xi, "Experimental Observations in a Self-mixing Laser Diode", *OSA Advanced Solid State Lasers*, 29 September–3 October 2019, Vienna, Austria

[C9]. B. Liu, **Y. Ruan**, Y. Yu, J. Xi, Q. Guo, and J. Tong, "Sensing by Dynamics of Laser with Optical Feedback", *4th International Conference on Sensors Engineering and Electronics Instrumentation Advances,* 19 - 21 September 2018, Amsterdam, The Netherlands

[C10]. B. Liu, **Y. Ruan**, L. Cao, Y. Yu, J. Xi, Q. Guo, and J. Tong, "Influence of system bandwidth on self-mixing signal", *SPIE Photonics Asia Conference*, 11 - 13 October 2018, Beijing, China

[C11]. H. Wang, **Y. Ruan**, L. Cao, Y. Yu, J. Xi, Q. Guo, J. Tong and J. Zhang, "Profile measurement using a self-mixing laser diode", *SPIE Photonics Asia Conference*, 11 - 13 October 2018, Beijing, China

[C12]. F. Xia, **Y. Ruan**, Y. Yu, Q. Guo, J. Xi, and J. Tong, "Retrieve the Material Related Parameters from a Self-Mixing Signal Using Wavelet Transform", *IEEE International Frequency Control Symposium*, 22 - 24 May 2018, Olympic Valley, California, USA

Certification

I, Yuxi Ruan, declare that this thesis submitted in fulfilment of the requirements for the conferral of the degree Doctor of Philosophy, from the University of Wollongong, is wholly my own work unless otherwise referenced or acknowledged. This document has not been submitted for qualifications at any other academic institution.

_____

Yuxi Ruan

15th March 2020

List of Acronyms

AM	amplitude modulation
BS	beam splitter
FC	fiber coupler
FM	frequency modulation
LD	laser diode
L-K	Lang-Kobayashi
OFI	optical feedback interferometry
OSC	oscilloscope
P1	period-one
PD	photodiode
PZT	piezoelectric transducer
RO	relaxation oscillation
SMI	self-mixing interferometry
VA	variable attenuator

Table of Contents

List of Figures and Tables

Chapter 1. Introduction

1.1. Background

The lasers diodes (LDs) experiencing external optical feedback are known to demonstrate complex dynamics, it is conceptually interesting as they unveil new and unexpected behavior of the optical system. This phenomenon was first reported in the late 1960s [1]. It was found that if a small proportion of the output beam from a gas maser is reflected back into it by an additional external mirror, then as the phase of the returned radiation changes through 2π , i.e. as the mirror moves through half a wavelength, the intensity of oscillation within that maser is modulated through one cycle. It was noted that it can provide useful information on the fundamental physics of semiconductor lasers, and the feedback induced fast intensity modulation might even be useful for optical communication systems [2, 3]. However, through the 1970s, 1980s and even in early 1990s, the optical feedback induced dynamics was predominantly regarded as a nuisance to applications. A significant motivation to study this effect was to find ways to avoid or control them, and to some extent they still do [4-8]. The reason is that the instability-induced intensity "noise" is much larger than the quantum noise in these lasers. Such enhanced intensity fluctuations were identified to have seriously deteriorating effects, particularly when they fell within the signal bandwidth, and therefore limited the usefulness of semiconductor lasers [9].

Nevertheless, the positive aspects of optical feedback induced dynamics were seen when consideration was given to the spectral properties of semiconductor lasers. The mechanisms for mode selection in semiconductor lasers represent a continuing area for fundamental investigation which has long antecedents in the pioneering work of Bogatov *et al*. [10]. External feedback was shown to enhance longitudinal mode selection and hence could be useful in narrowing the emission spectrum of semiconductor lasers [11]. The intimate connections between the dynamics and spectra of semiconductor lasers were identified in early work [12] and remain an ever-present theme in the development of semiconductor lasers [13]. Another positive aspect is the response of optical feedback in semiconductor lasers can be either sensed via the laser terminal voltage [14] or observing the laser output intensity, thus encapsulate information about the external cavity and the optical properties of the target. This has led to the discovery of a new class of laser interferometry, named Optical Feedback Interferometry (OFI).

1.2. Optical Feedback Interferometry (OFI)

Optical Feedback Interferometry (OFI), also called Self-Mixing Interferometry (SMI) is a promising non-contact sensing technique. Since the first demonstration in 1963, the research on the optical feedback has been carried out under many names, induced-modulation [15], back-scatter-modulation [16], self-coupling [17], and autodyning [18], to name a few. The OFI is based on the optical feedback effect which is the mixing of the intra-cavity electromagnetic wave with an emitted electromagnetic wave reinjected into the laser cavity after interaction in the external cavity. Such effect can cause perturbs to the several laser source properties such as threshold current, emitted power, lasing

spectrum, bandwidth, junction voltage. The optical feedback effect is a remarkably universal phenomenon, occurring in lasers regardless of type. Among others, the effect has been reported in gas lasers [1], semiconductor diode lasers [4, 17, 19], vertical-cavity surface-emitting lasers (VCSELs) [20, 21], mid-infrared [22, 23] and terahertz quantum cascade lasers (THz QCLs) [24, 25], interband cascade lasers [26, 27], fiber and fiber ring lasers [28-30], solid-state lasers [31, 32], microring lasers [33, 34], and quantum dot lasers [35, 36].

The basic structures of a typical OFI is depicted in Fig. 1.1. For an OFI system, a photodiode (PD) is packaged in the rear of the laser diode (LD), the whole unit acts both as the source and the detector, therefore, only one optical path is needed. Due to the optical feedback effect, the modulated laser intensity known as the OFI signal is captured by the PD and displayed on the oscilloscope.

The advantages of OFI-based sensing scheme are summarized as below [20, 37, 38]:

- Optical part-count is minimal. No extra optical interferometer external to laser source is needed, leading to a compact and part-count-saving set-up.
- The OFI signal can be achieved at anywhere on the light path.
- Very weak external optical feedback, e.g. less than 0.1% of the laser emitting intensity, is sufficient to cause optical feedback effect, which means OFI technology is applicable for rough diffusive surfaces.
- Sensitivity is high. The resolution of half laser wavelength ($\lambda_{laser}/2$) can be achieved with fringe-counting and sub-wavelength can be achieved with analog processing.

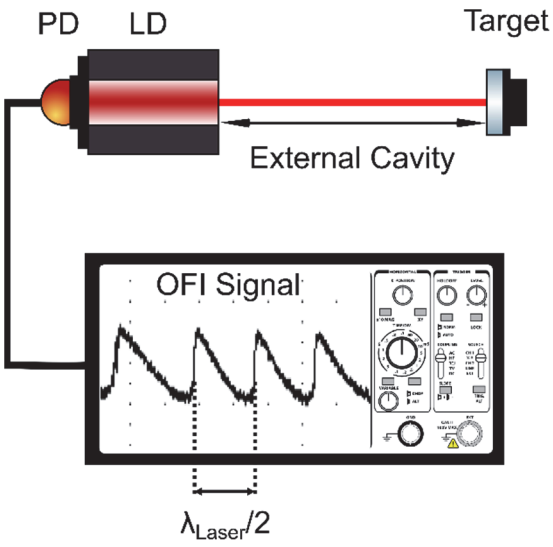

Fig. 1.1: Schematic diagram of Optical Feedback Interferometry system

Due to OFI system's merits of minimum part-count scheme, low cost in implementation and ease in optical alignment, various OFI-based applications have been developed in the industrial and laboratory environment, which can be classified as below:

- Metrology: angle [39-41], balance [42], absolute distance [43-46], displacement [47-51], velocity [52-56], vibration [57-60], etc.
- Physical quantities: mechanic resonance [61], thickness [62, 63], temperature [64, 65], refractive index [66], roughness [67, 68], strain [69, 70], Young's modulus [71, 72], etc.
- Laser parameter: laser linewidth [73-75] , linewidth enhancement factor [76-81].
- Sensing: acoustic emission sensor [82, 83], biological motility [55, 84], CD/scroll sensors [85], confocal microscopy sensor [86, 87], remote echoes sensors [88], etc.
- Imaging [89-92].

1.3. Sensing Theory of OFI

1.3.1. Lang and Kobayashi Equations

The mathematic model for describing the LD with optical feedback was first studied by the Nobel Prize laureate Wills E. Lamb and Martin B. Spencer. They carried out an analysis based on the slowly varying approximation of field amplitude E and phase ϕ of the oscillating field, the model is now called Lamb's equations. They are well suited to Class A lasers such as gas and crystal lasers, in which E and ϕ are decoupled from the density of state N [93], whereas in a semiconductor laser (Class B), a third equation is added to describe N and its dependence on E and ϕ. This modification of Lamb's equations are known as the Lang and Kobayashi (L-K) equations. Lang and Kobayashi focused on the aspects of the basic physics of semiconductor laser which were likely to lead to complex behaviour under conditions of external feedback, such as broad gain spectrum, temperature dependence of material refractive index, carrier-density dependence of the refractive index. In their publication [94], the L-K equations for a single-mode laser described the time evolution of the complex optical field and the carriers. They included the influence of the optical feedback by considering the interference of the laser field with its own coherent delayed field that had propagated once through the external cavity. The L-K equations describe the electric field amplitude $E(t)$, electric field phase $\phi(t)$ and carrier density $N(t)$ as following,

$$\frac{dE(t)}{dt}=\frac{1}{2}\left\{G\left[N(t),E(t)\right]-\frac{1}{\tau_p}\right\}E(t)+\frac{\kappa}{\tau_{in}}\cdot E(t-\tau)\cdot\cos\left[\omega_0\tau+\phi(t)-\phi(t-\tau)\right] \qquad (1.1)$$

$$\frac{d\phi(t)}{dt}=\frac{1}{2}\alpha\left\{G\left[N(t),E(t)\right]-\frac{1}{\tau_p}\right\}-\frac{\kappa}{\tau_{in}}\cdot\frac{E(t-\tau)}{E(t)}\cdot\sin\left[\omega_0\tau+\phi(t)-\phi(t-\tau)\right] \qquad (1.2)$$

$$\frac{dN(t)}{dt} = \frac{J}{eV} - \frac{N(t)}{\tau_s} - G\left[N(t), E(t)\right]E^2(t) \tag{1.3}$$

$\phi(t)$ is given by $\phi(t) = [\omega(t) - \omega_0]t$, where $\omega(t)$ is the instantaneous optical angular frequency for an LD with optical feedback, ω_0 is the unperturbed optical angular frequency for a solitary LD. $G[N(t), E(t)] = G_N[N(t) - N_0][1 - \varepsilon\Gamma E^2(t)]$ is the modal gain per unit time. The LD's intensity or output power is denoted by $I(t) = E^2(t)$. The physical meanings of the symbols appearing in Eq.(1.1)-Eq.(1.3) and the values of the parameters used in this thesis can be found in Table 1-1, which is adopted from [95, 96],

Table 1-1: Physical meanings of the symbols in the L-K equations

	Symbol	PHYSICAL MEANING	Value
LD Internal Parameters	G_N	Model gain coefficient	$8.1\times10^{-13}\,\mathrm{m^3s^{-1}}$
	N_0	Carrier density at transparency	$1.1\times10^{24}\,\mathrm{m^{-3}}$
	ε	Nonlinear gain compression coefficient	$2.5\times10^{-23}\,\mathrm{m^3}$
	Γ	Confinement factor	0.3
	τ_p	Photon lifetime	$2.0\times10^{-12}\,\mathrm{s}$
	τ_s	Carrier lifetime	$2.0\times10^{-9}\,\mathrm{s}$
	τ_{in}	Internal cavity round-trip time	$8.0\times10^{-12}\,\mathrm{s}$
	e	Elementary charge	$1.6\times10^{-19}\,\mathrm{C}$
	V	Volume of the active region	$1\times10^{-16}\,\mathrm{m^3}$
	ω_0	Unperturbed optical angular frequency of a laser diode, $\omega_0 = 2\pi c/\lambda_0$, where c is the speed of light, λ_0 is the wavelength of the LD	
	α	Line-width enhancement factor	
LD External Parameters	J	Injection current	
	κ	Feedback strength	
	L	External cavity length	
	τ	Light round-trip time in the external cavity, $\tau = 2L/c$	

m = meter, s = second, C = coulomb

1.3.2. Mathematical Model of an OFI system

1.3.2.1. Derived from the Three-Mirror model

In order to analyse the behavior of an OFI system, researchers have proposed different system models. In 1988, Petermann [97] presented an Three-Mirror model, which shows that the basic structure of an OFI system can be elegantly illustrated by the three-mirror setup.

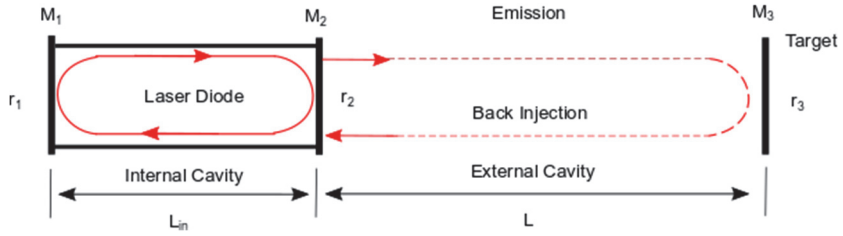

Fig. 1.2: Three-Mirror model of an OFI

As shown in Fig. 1.2, the internal laser cavity is formed a rear facet mirror M_1 and a rear facet mirror M_2 with length L_{in}. The laser intensity amplitude reflectivity of M_1 and M_2 is r_1 and r_2 respectively. The target in the external cavity is illustrated as the third mirror M_3 which has an amplitude reflectivity of r_3. The external cavity length L is the distance between M_2 and M_3. The Three-Mirror model assumed the LD is a Fabry-Perot type laser, the OFI system can be simplified to a laser diode with M_1 and M_3 as shown in Fig. 1.3 [97].

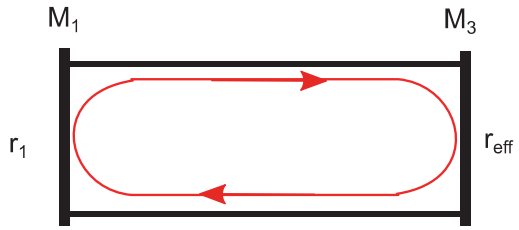

Fig. 1.3: Simplified Three-Mirror model of an OFI system

Assuming $|r_2 r_3| << 1$, i.e. multi-reflection within the external cavity is neglected. Then, the equivalent amplitude reflectivity r_{eff} of M_3 can be expressed as [97, 98]:

$$r_{eff} = A_{eff} e^{-j\phi_{eff}} = r_2 + \left(1 - |r_2|^2\right) r_3 e^{-j\omega_s \tau} \tag{1.4}$$

Where ω_s the laser angular frequency with optical feedback. the optical feedback strength κ describes the coupling rate of re-injected light into the internal cavity length, which is expressed as:

$$\kappa = \eta(1 - r_2^2) r_3 / r_2 \tag{1.5}$$

Where η is the coupling efficiency which accounts for possible loss on re-injection, e.g. mode mismatch, finite coherence length. When $\kappa << 1$, from Eq. (1.4), we can get:

$$A_{eff} = r_2 \left[1 + \kappa \cos(\omega_s \tau)\right] \tag{1.6}$$

$$\phi_{eff} = \kappa \sin(\omega_s \tau) \tag{1.7}$$

since $\kappa \sin(\omega_s \tau) << r_2 \left[1 + \kappa \cos(\omega_s \tau)\right]$ and $\arctan(x) \approx x$ for small x [38].

As the round-trip phase in the laser cavity must be equal to an integer multiple of 2π, we obtain the phase condition of compound cavity of the Three-Mirror model shown as below:

$$-\alpha(g_c - g_{th})d + \tau_{in}(\omega_s - \omega_0) + \phi_{eff} = 2\pi q \tag{1.8}$$

where q is an integer, α is the linewidth enhancement factor of the laser. τ_{in} is the laser roundtrip time in the internal cavity ,expressed as $\tau = 2n_{in}L_{\text{in}} / c$ and ω_0 is the angular frequency of the solitary laser without feedback. g_c and g_{th} are the threshold gain of the laser with and without external feedback respectively [97]. g_{th} can be expressed as:

$$g_{th} = a_s + d^{-1} \ln\left[(r_1 r_2)^{-1}\right] \tag{1.9}$$

where a_s accounts for any optical loss in the internal cavity. Additionally, g_c must satisfy the amplitude condition of the compound cavity [97, 98]:

$$r_1 A_{eff} e^{[(g_c - a_s)d]} = 1 \tag{1.10}$$

Inserting Eq. (1.6) and Eq.(1.9) into Eq.(1.10), we can obtain:

$$g_c - g_{th} = -\frac{\kappa}{d}\cos(\omega_s \tau) \tag{1.11}$$

Then, inserting Eq. (1.7) and Eq.(1.11) into Eq.(1.8) and letting q=0 , i.e. the phase difference is 0 , the phase equation of the OFI system is give as below:

$$\omega_s \tau = \omega_0 \tau - \frac{\kappa}{\tau_{in}} \tau \sqrt{1+\alpha^2} \sin\left[\omega_s \tau + \arctan(\alpha)\right] \tag{1.12}$$

Although, some interesting results can be explained by using the Three-Mirror model, the details related to the physical settings of the phenomena are not be explained.

1.3.2.2. Derived from the Lang and Kobayashi equations

To investigate the more detailed phenomena of the OFI system, in 1995, Donati et al. [99] presented an analytical OFI model by solving the L-K equations with steady state solutions. Compare Three-Mirror model, the L-K equations are point-independent equations. E_s, N_s and ω_s were introduced to represent the stationary solutions of L-K equations for electric field amplitude, carrier density and angular frequency respectively.

The L-K equations are solving by setting $dE(t)/dt = 0$, then Eq.(1.1) becomes,

$$N_s = N_0 + \frac{1}{\tau_p G_N} - \frac{2\kappa \cos(\omega_s \tau)}{\tau_{in} G_N} \tag{1.13}$$

Setting $d\phi(t)/dt = \omega_s - \omega_0$, Eq.(1.2) becomes,

$$\omega_s \tau = \omega_0 \tau - \frac{\kappa}{\tau_{in}} \tau \sqrt{1+\alpha^2} \sin(\omega_s \tau + \arctan \alpha) \tag{1.14}$$

Introducing $\phi_0 = \omega_0 \tau$, $\phi_s = \omega_s \tau$ and $C = \frac{\kappa}{\tau_{in}} \tau \sqrt{1+\alpha^2}$, Eq.(1.14) is expressed as,

$$\phi_s = \phi_0 - C \sin\left[\phi_s + \arctan(\alpha)\right] \tag{1.15}$$

Setting $dN(t)/dt = 0$, Eq.(1.3) becomes,

$$E_s^{\,2} = \frac{J - N_s/\tau_s}{G_N (N_s - N_0)} \tag{1.16}$$

Eq.(1.13), Eq.(1.14) and Eq.(1.16) are commonly known as the steady state solutions of the L-K equations.

The OFI signal can be derived by substitute Eq.(1.13) into Eq.(1.16), then we have,

$$E_s^{\,2} = \frac{\frac{\tau_p}{\tau_s} * (J\tau_s - N_0 - \frac{1}{G_N \tau_p} + \frac{2\kappa \cos(\omega_s \tau)}{\tau_{in} G_N})}{1 - \frac{2\kappa \tau_p \cos(\omega_s \tau)}{\tau_{in}}} \tag{1.17}$$

Limiting treatment to the practical case $\kappa < 0.01$ and using Tayler series, $E_s^{\,2}$ can be approximated as follow,

$$E_s^{\,2} = \frac{\tau_p}{\tau_s} * (J\tau_s - N_0 - \frac{1}{G_N \tau_p} + \frac{2\kappa \cos(\omega_s \tau)}{\tau_{in} G_N}) * (1 + \frac{2\kappa \tau_p \cos(\omega_s \tau)}{\tau_{in}}) \tag{1.18}$$

Indicating with E_{NF} the stationary electric field in the case of no feedback and $E_{NF}^2 = \tau_p [J - (N_0 + \frac{1}{G_N \tau_p}) \Big/ \tau_s]$, therefore,

$$E_s^{\,2} - E_{NF}^{\,2} = \frac{2J\tau_P^2}{\tau_{in}} \kappa \cos(\omega_s \tau) - \frac{2N_0 \tau_P^2}{\tau_s \tau_{in}} \kappa \cos(\omega_s \tau) + \frac{4\tau_p^2}{\tau_{in}^2 G_N \tau_s} \kappa^2 \cos^2(\omega_s \tau) \tag{1.19}$$

Neglecting second-order contributions, Eq.(1.19) becomes,

$$E_s^{\,2} - E_{NF}^{\,2} = (\frac{2J\tau_P^2}{\tau_{in}} - \frac{2N_0 \tau_P^2}{\tau_s \tau_{in}}) \kappa \cos(\omega_s \tau) \tag{1.20}$$

Let $\Delta P = \frac{2J\tau_P^2}{\tau_{in}} - \frac{2N_0\tau_P^2}{\tau_s\tau_{in}}$, it can be seen that ΔP is determined by the LD internal parameters and the injection current. It can be treated as a constant once the physical system is established. The OFI signal P can be expressed as,

$$P = \Delta P\kappa\cos(\phi_s) \tag{1.21}$$

The Eq.(1.15) and Eq.(1.21) constitute the OFI model which has been widely used to describe the OFI signal.

1.3.3. Sensing Signal Features

In the OFI model, C is called optical feedback level, it is an important quantity for characterizing feedback. It was proposed by Acket in [100] and used to distinguish between the low feedback regime ($C < 1$) and high feedback regime ($C > 1$). A more detailed feedback regimes studied by Tkach and Chraplyvy presented a T-C diagram shown in Fig. 1.4 which classified five feedback regimes [101].

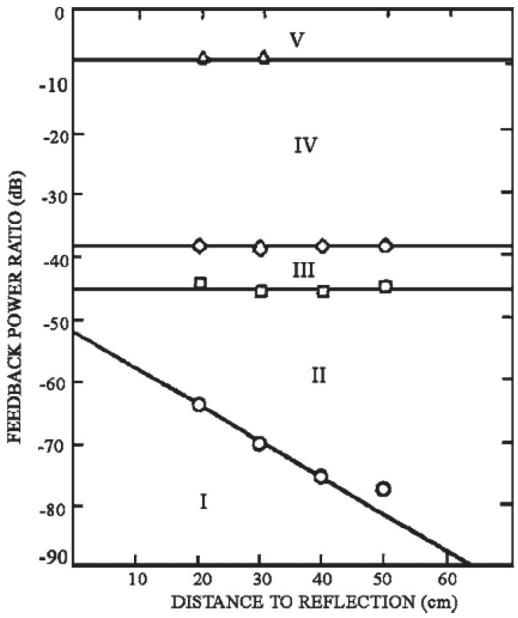

Fig. 1.4: T-C diagram with five feedback regimes [101]

As C increases from zero, the five qualitatively different regimes are [38, 102]:

Regimes I: It is characterized by weak optical feedback ($C < 1$) with a single emission frequency and a narrowing or broadening of the emission line depending on the phase of the feedback. In this regime, the phase equation Eq.(1.15) presents a unique mapping from ϕ_0 to ϕ_s. In some works, the approximation of $\phi_s \approx \phi_0$ have been taken in [44, 103, 104]. Fig. 1.5 shows the relationship between ϕ_0 and ϕ_s as well as P and ϕ_0 under weak feedback when $C = 0.5$ and $\alpha = 3$. Supposing a continuous sinusoidal displacement is applied on the target with $L(t) = L_0 + \Delta L \cdot \sin(2\pi ft)$, where L_0, ΔL and f are the initial external cavity length, the amplitude of the displacement and frequency respectively. They are chosen as $L_0 = 0.24m$, $\Delta L = 1.5\lambda_0$ and $f = 400KHz$. In this case, the variation of the initial optical phase can be expressed as: $\Delta\phi_0(t) = 4\pi\Delta L \sin(2\pi ft)/\lambda_0$. Fig. 1.6 shows the time-varying optical phase and its corresponding OFI signal.

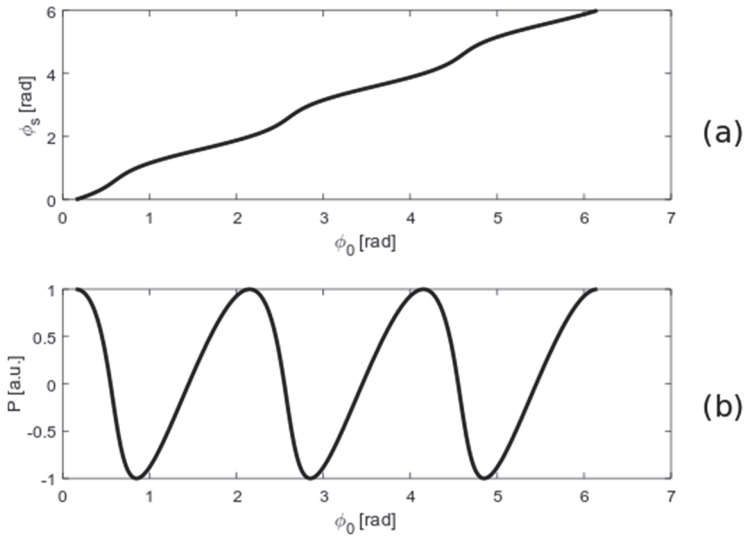

Fig. 1.5: Influence of external cavity on laser frequency and intensity at weak feedback with $C = 0.5$ and $\alpha = 3.0$. (a) Relationship between ϕ_0 and ϕ_s. (b) Relationship between P and ϕ_0.

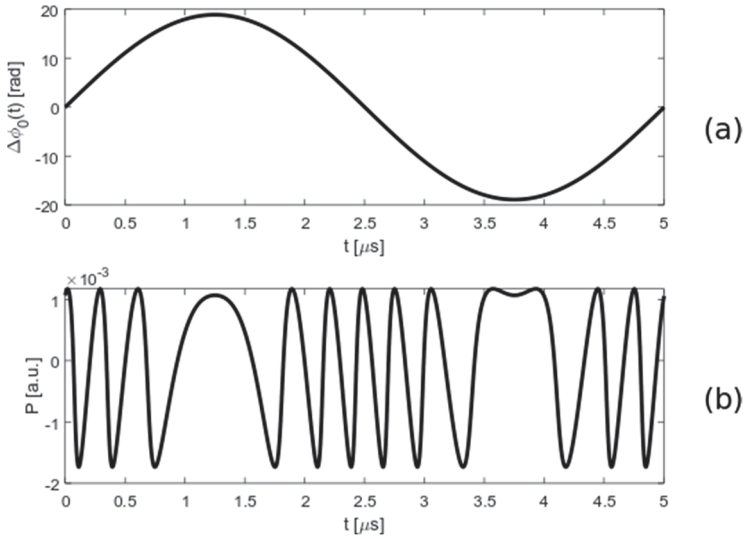

Fig. 1.6: OFI signal at weak feedback with $C = 0.5$ and $\alpha = 3.0$. (a) Time-varying optical phase induced by a moving target. (b) OFI signal.

Regimes II: It is characterized by moderate feedback ($1 < C < 4.6$), which results in multiple emission frequencies and apparent splitting of the emission line due to rapid mode hopping. Varieties of OFI-based applications have set the system in moderate feedback, and the behavior of the OFI in this regime have been investigated intensely [76, 105, 106]. Based on the behavior analysis in [76, 105], when ϕ_0 increases, that ϕ_s and P will track the route $\mathrm{A} \rightarrow \mathrm{B} \rightarrow \mathrm{C}$, when ϕ_0 decrease the route will be $\mathrm{C} \rightarrow \mathrm{D} \rightarrow \mathrm{A}$ as shown in Fig. 1.7. In the phase equation, when ϕ_0 locates between point A and C, ϕ_0 will yields three ϕ_s. Similar to Fig. 1.6 (a), when a continuous sinusoidal displacement is applied on the target, the OFI signal presents asymmetric hysteresis and produces a sawtooth-like fringes, shown in Fig. 1.8 (b).

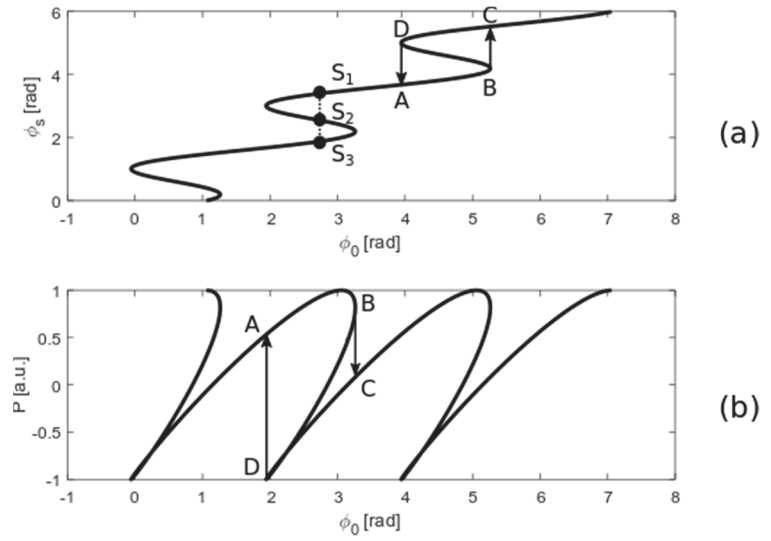

Fig. 1.7: Influence of external cavity on laser frequency and intensity at moderate feedback with $C = 3.5$ and $\alpha = 3.0$. (a) Relationship between ϕ_0 and ϕ_s . (b) Relationship between P and ϕ_0 .

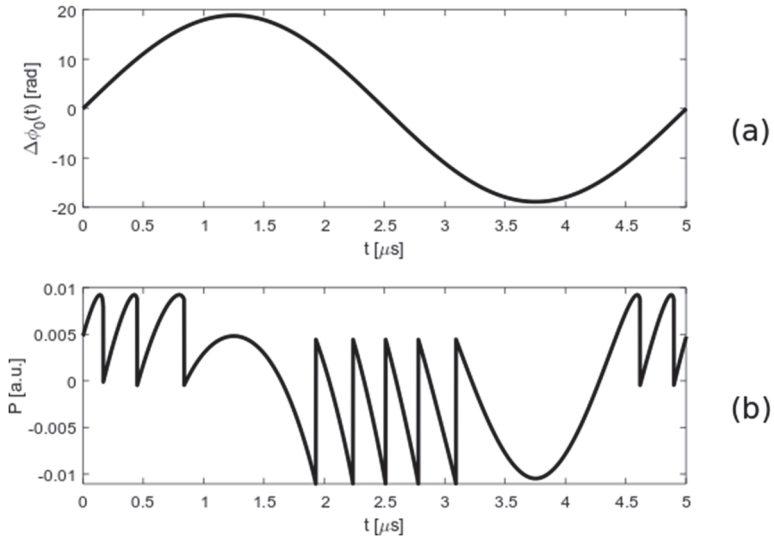

Fig. 1.8: OFI signal at moderate feedback with $C = 3.5$ and $\alpha = 3.0$. (a) Time-varying optical phase induced by a moving target. (b) OFI signal.

Regimes III: It is characterized by strong feedback ($C > 4.6$), which results in a return to single emission frequency. The work [107] studied the behavior of OFI system with a large C , and gave the details about the mode jumping rules. Indicated in Fig. 1.9, when ϕ_0 increases, that ϕ_s and P will track the route $\mathrm{A} \to \mathrm{B} \to \mathrm{C} \to \mathrm{D} \to \mathrm{E}$, when ϕ_0

decrease the route will be $\mathrm{E} \to \mathrm{F} \to \mathrm{G} \to \mathrm{H} \to \mathrm{A}$. In the phase equation, five or even more possible ϕ_s may be yielded from a single ϕ_0. When a continuous sinusoidal displacement is applied on the target, the corresponding OFI signal is presented in Fig. 1.10 (b). The signal is still in saw-tooth like waveform but it may experience fringe loss [59, 107]. Additionally, when C increases to certain values, the shape of the OFI signals may closely replicates that of the external movement.

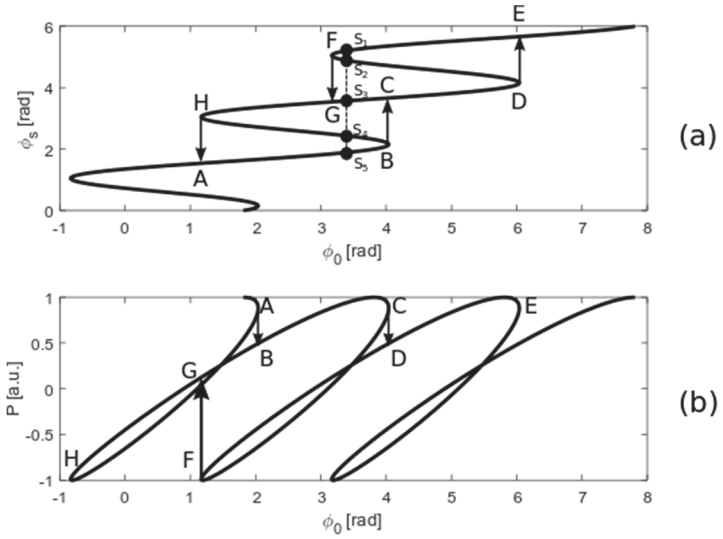

Fig. 1.9: Influence of external cavity on laser frequency and intensity at strong feedback with $C = 6.0$ and $\alpha = 3.0$. (a) Relationship between ϕ_0 and ϕ_s. (b) Relationship between P and ϕ_0.

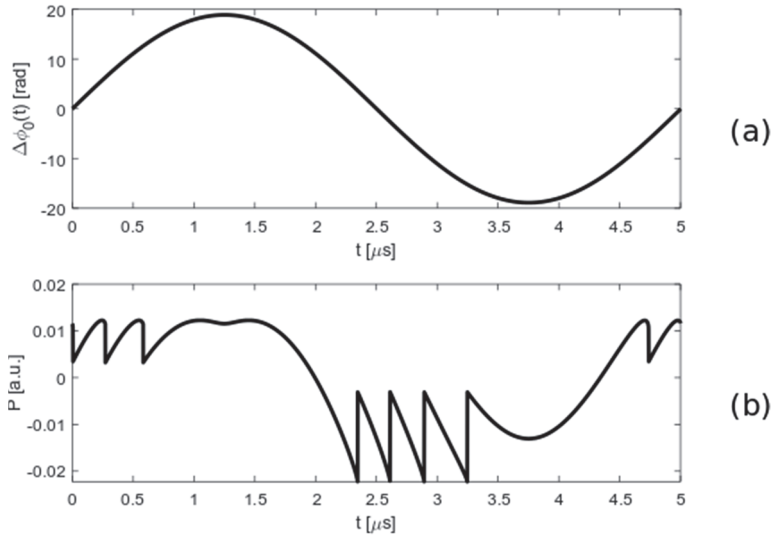

Fig. 1.10: OFI signal at strong feedback with $C = 6.0$ and $\alpha = 3.0$. (a) Time-varying optical phase induced by a moving target. (b) OFI signal.

Regime IV: It is characterized by chaotic dynamics with islands of stability [102] and broadening of the emission line, a state often referred to as "coherence collapse".

Regime V: It is characterized by a return to stability, when the system effectively operates as an optically pumped long external cavity laser. This regime occurs when the feedback level is much greater than the laser relaxation oscillation frequency. The laser under optical feedback is independent of the phase of the feedback.

1.4. Thesis Outline

This thesis consists of five chapters and is organized as below.

Chapter 2 presented a dual-cavity OFI system to addresses the issue of sensitivity degradation associated with an OFI sensing system due to the weak optical feedback of the target. Following the principle of the single-cavity OFI model, a theoretical model for

the dual-cavity OFI is derived from the steady state solutions of the dual-cavity L-K equations. A mathematic expression of the signal enhancement is obtained, elaborating how the feedback strength of the control target and the control cavity length influence the enhancement.

Chapter 3 starts with the investigation on the validity of both L-K equations and the OFI model when describe the OFI signal. We study the dynamic states in conjunction with the feedback regimes and presented a bifurcation diagram that consists both features. Base on such bifurcation diagram, we classified a new five regions. In each of the regions, the OFI signals generated from both LK equations are simulated and compared with that from the OFI model. Such study on the validity of OFI model and LK equations provide a guidance on applying appropriate models when designing OFI based sensing system. In Section 3.3, we present a new sensing scheme making use of laser dynamics associated with a dual-cavity OFI system to improve the sensing sensitivity. The second cavity is used to control the laser dynamics and ensure the LD operates at P1 state. The laser intensity in the P1 exhibits an oscillation with its amplitude modulated by an OFI signal (generated with a single cavity and LD operating at steady state). It is observed that the modulation depth is remarkably larger than the magnitude of the OFI signal. By adjusting the feedback strength, the system can be set at a most optimal working point for sensing and measurement. In Section 3.4, a new approach to achieve a sub-nanometre scale displacement sensing is also proposed, which is based on a fringe sub-division algorithm that utilizes the high frequency component of the laser intensity signal and a signal processing technique in the time-domain.

Chapter 4 presents a linewidth enhancement (α) factor measurement using the relaxation oscillation (RO) frequency. The RO frequency of a laser can be modified by external optical feedback. Based on this fact, we investigated the relation between the RO frequency and α factor and presented three measurement methods.

Chapter 5 summarized the contributions of this thesis and its relevant publications.

Chapter 2. Proposed Dual-Cavity Configuration

The dual-cavity configuration in optical feedback interferometry was first proposed in [108] by Fischer et al. It was called T-shaped cavity model that consists the LD and two external high reflecting gold mirrors. The model was used to study the transition phenomena from regular to high-dimensional chaotic behavior and it was regarded as an ideal candidate when studying the dynamics in nonlinear systems with many degrees of freedom. In 1997, Liu et al. used dual-cavity configuration to study the dynamical behaviors. Their publication [109] emphasis the variation of the laser output dynamics versus the ratios between the two external cavity lengths and reflectivity. Based on the bifurcation diagram, they conclude the stable region is quite robust for wide parameter ranges, which suggests the dual-cavity configuration can be applied to stabilize of the feedback-induced chaos. This function was later confirmed by Rogister et. al [110], furthermore, he gave an theoretical analysis on how the second feedback cavity can suppress the low frequency fluctuations. In 2003 Wang et al [111], experimentally demonstrated the suppression of low frequency fluctuations using the dual-cavity configuration. With the assist of signal processing techniques, they realized an absolute distance and microscopic displacement measurement. In recent years, researchers have utilized the dual-cavity configuration in many applications. In [112], it was used to compress the linewidth of the single longitudinal mode distributed feedback laser. Compare to the single cavity feedback, this approach can reduce the linewidth from Mhz

level to serval kHz. The work in [113, 114], proposed Doppler velocity measurement method based on the OFI with two parallel optical external cavity, then use Fast Fourier Transform applied on the obtained OFI signal to obtain two sets of Doppler shifts. Hence, the corresponding motion velocity of the target object can be measured via the sum of the two Doppler shifts. In [115-117], 2D vibration measurement and moving detection of multiple targets are achieved using the dual-cavity OFI and the work in [118] proposes to use the second cavity to realize nanoscale displacement sensing.

It is noted that the magnitude of the OFI signal mainly depends on the optical feedback level. However, in some practical applications, the target surface to be measured has very low reflectivity and thus it is unable to generate adequate feedback light reflected back into the LD, leading to weak and blurred OFI signal. In this situation, the sensing sensitivity of the system is severely degraded and the OFI system may even lose its sensing ability. A general way to address this problem is to affix a mirror or a piece of material with high reflectivity on the target, so that a high enough feedback level can be generated to get a clear OFI signal. However, in some applications, it is inconvenient or even impossible to affix high reflectivity materials on the target, e.g., the measurand target is a living organism, a fluid field, or acoustic emission. Therefore, it is highly desirable to develop a method which enables the OFI system to achieve high sensitive sensing. There have been a few publications focus on improving the dual-cavity configurations sensitivity. In [111], it notices the increasing of the target feedback strength will lead to the increasing of the laser intensity waveform's amplitude, and the waveform is similar to the signal-cavity configuration. However, the feedback strength in the paper was referring to the measurand target, and it did not give further analysis whether the

waveform in dual-cavity can be used for sensing purpose. In [119, 120], a large number of simulations were performed to valid the feedback strength of the second target and the length of the second cavity have impact on the laser intensity waveform. Their simulations show there are about 2-4 time signal amplitude improvement. However, it has lack of mathematical explanation how these factors are affecting the signal amplitude.

Based on the conventional single-cavity OFI shown in Fig. 1.1, the dual-cavity OFI is implemented by adding another target (Target-2) and forms a second cavity. We name it as the control cavity. We defined the target which associated with quantities to be measured as Target-1 or the measurand target, the cavity between the LD to Target-1 is called the measurand cavity. The dual-cavity OFI has the structural similarity to the Michelson interferometer, but different in terms of functions. The function of adding Target-2 is to increase the sensitivity of the overall system and control the LD dynamic (discussed in Chapter 3). Since it is based on OFI system, therefore it inherited all the advantages that single-cavity OFI has, such as no external PD is needed, the LD is acted as both source and receiver. The interferometric signal is achieved at everywhere on the beam. The system is applicable for rough diffusive surfaces and half-laser wavelength or sub-wavelength resolution are achievable.

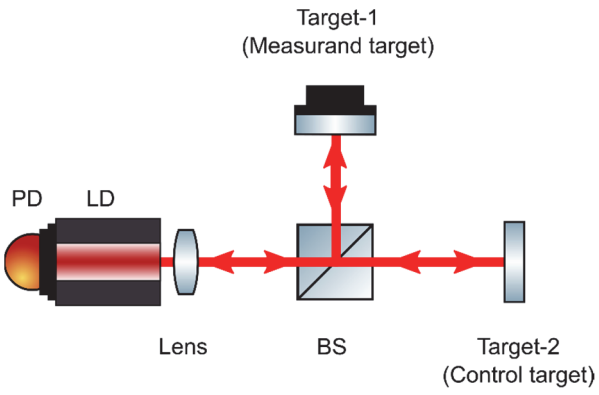

Fig. 2.1: Dual-cavity OFI configuration.

The dynamic behavior of an LD in a single-cavity OFI is describe by the L-K equations. For the dual-cavity OFI, the original L-K equations can be modified in below [109]. Note that the symbols with subscript '1' are relevant to Target-1 and '2' are relevant to Target-2.

$$\frac{dE(t)}{dt} = \frac{1}{2}\left\{G\left[N(t),E(t)\right] - \frac{1}{\tau_p}\right\}E(t) + \frac{\kappa_1}{\tau_{in}} \cdot E(t-\tau_1) \cdot \cos\left[\omega_0\tau_1 + \phi(t) - \phi(t-\tau_1)\right] + \frac{\kappa_2}{\tau_{in}} \cdot E(t-\tau_2) \cdot \cos\left[\omega_0\tau_2 + \phi(t) - \phi(t-\tau_2)\right] \tag{2.1}$$

$$\frac{d\phi(t)}{dt} = \frac{1}{2}\alpha\left\{G\left[N(t),E(t)\right] - \frac{1}{\tau_p}\right\} - \frac{\kappa_1}{\tau_{in}} \cdot \frac{E(t-\tau_1)}{E(t)} \cdot \sin\left[\omega_0\tau_1 + \phi(t) - \phi(t-\tau_1)\right] - \frac{\kappa_2}{\tau_{in}} \cdot \frac{E(t-\tau_2)}{E(t)} \cdot \sin\left[\omega_0\tau_2 + \phi(t) - \phi(t-\tau_2)\right] \tag{2.2}$$

$$\frac{dN(t)}{dt} = J - \frac{N(t)}{\tau_s} - G\left[N(t),E(t)\right]E^2(t) \tag{2.3}$$

2.1. Dual-Cavity OFI Model

In the conventional single-cavity OFI system, the steady state solutions of the L-K equations is called as the OFI model. For dual-cavity OFI, the steady state solutions can be derived from the dual-cavity L-K equations Eq.(2.1)-Eq.(2.3), by setting $dE(t)/dt = 0$, $d\phi(t)/dt = \omega_s - \omega_0$ and $dN(t)/dt = 0$. First, let's set $dE(t)/dt = 0$, then Eq. (2.1) becomes,

$$\frac{1}{2}[G_N(N_s - N_0) - \frac{1}{\tau_p}] + \frac{\kappa_1}{\tau_{in}} \cdot \cos(\omega_s\tau_1) + \frac{\kappa_2}{\tau_{in}} \cdot \cos(\omega_s\tau_2) = 0$$

$$G_N N_0 + \frac{1}{\tau_p} - \frac{2}{\tau_{in}}(\kappa_1 \cos(\omega_s\tau_1) + \kappa_2 \cos(\omega_s\tau_2)) = G_N N_s$$

Therefore,

$$N_s = N_0 + \frac{1}{G_N \tau_p} - \frac{2(\kappa_1 \cos(\omega_s \tau_1) + \kappa_2 \cos(\omega_s \tau_2))}{\tau_{in} G_N} \tag{2.4}$$

Second, let's set $d\phi(t)/dt = \omega_s - \omega_0$, then Eq. (2.2) becomes,

$$\frac{1}{2}\alpha[G_N(N_s - N_0) - \frac{1}{\tau_p}] - \frac{\kappa_1}{\tau_{in}} \cdot \sin(\omega_s \tau_1) - \frac{\kappa_2}{\tau_{in}} \cdot \sin(\omega_s \tau_2) = \omega_s - \omega_0$$

Since $N_s = N_0 + \frac{1}{G_N \tau_p} - \frac{2(\kappa_1 \cos(\omega_s \tau_1) + \kappa_2 \cos(\omega_s \tau_2))}{\tau_{in} G_N}$, substitute into above. We have,

$$\omega_s - \omega_0 = \frac{1}{2}\alpha[G_N(\frac{1}{G_N \tau_p} - \frac{2(\kappa_1 \cos(\omega_s \tau_1) + \kappa_2 \cos(\omega_s \tau_2))}{\tau_{in} G_N}) - \frac{1}{\tau_p}] - \frac{\kappa_1}{\tau_{in}} \cdot \sin(\omega_s \tau_1) - \frac{\kappa_2}{\tau_{in}} \cdot \sin(\omega_s \tau_2)$$

$$\omega_s - \omega_0 = -\frac{\alpha(\kappa_1 \cos(\omega_s \tau_1) + \kappa_2 \cos(\omega_s \tau_2))}{\tau_{in}} - \frac{\kappa_1}{\tau_{in}} \cdot \sin(\omega_s \tau_1) - \frac{\kappa_2}{\tau_{in}} \cdot \sin(\omega_s \tau_2)$$

$$\omega_0 = \omega_s + \frac{\kappa_1}{\tau_{in}}(\alpha \cos(\omega_s \tau_1) + \sin(\omega_s \tau_1)) + \frac{\kappa_2}{\tau_{in}}(\alpha \cos(\omega_s \tau_2) + \sin(\omega_s \tau_2))$$

Introducing τ_1 into the above equation then,

$$\omega_0 \tau_1 = \omega_s \tau_1 + \frac{\kappa_1}{\tau_{in}} \tau_1 \sqrt{1+\alpha^2} \sin(\omega_s \tau_1 + \arctan \alpha) + \frac{\kappa_2}{\tau_{in}} \tau_1 \sqrt{1+\alpha^2} \sin(\omega_s \tau_2 + \arctan \alpha)$$

Introducing $C_1 = \frac{\kappa_1}{\tau_{in}} \tau_1 \sqrt{1+\alpha^2}$ and $C_2 = \frac{\kappa_2}{\tau_{in}} \tau_1 \sqrt{1+\alpha^2}$ then $\omega_0 \tau_1$ becomes

$$\omega_s \tau_1 = \omega_0 \tau_1 - C_1 \sin(\omega_s \tau_1 + \arctan(\alpha)) + C_2 \sin(\omega_s \tau_2 + \arctan(\alpha)) \tag{2.5}$$

Third, let's set $dN(t)/dt = 0$, then Eq. (2.3) becomes,

$$J - \frac{N_s}{\tau_s} - G_N(N_s - N_0)E^2(t) = 0$$

$$J - \frac{N_s}{\tau_s} = G_N(N_s - N_0)E_s{}^2(t)$$

Rearrange the above equation,

$$E_s{}^2 = \frac{J - N_s/\tau_s}{G_N(N_s - N_0)} \tag{2.6}$$

In summary, Eq.(2.4), Eq.(2.5), Eq.(2.6) are the steady-state solutions for the dual-cavity OFI model, they are corresponded to the steady-state solution for the OFI model Eq.(1.13) , Eq.(1.14), Eq.(1.16).

Let's substitute Eq.(2.4) into Eq.(2.6), we have,

$$E_s^{\,2} = \frac{\frac{\tau_p}{\tau_s} * (J\tau_s - N_0 - \frac{1}{G_N\tau_p} + \frac{2\kappa_1 \cos(\omega_s\tau_1)}{\tau_{in}G_N} + \frac{2\kappa_2 \cos(\omega_s\tau_2)}{\tau_{in}G_N})}{1 - \frac{2\tau_p\kappa_1 \cos(\omega_s\tau_1)}{\tau_{in}} - \frac{2\tau_p\kappa_2 \cos(\omega_s\tau_2)}{\tau_{in}}} \tag{2.7}$$

Eq.(2.5) and Eq.(2.7) are the dual-cavity OFI model. If Target-2 related terms are removed, Eq.(2.5) and Eq.(2.7) are reduced to

$$E_{s\_\text{Target-1}}^2 = \frac{\frac{\tau_p}{\tau_s} * (J\tau_s - N_0 - \frac{1}{G_N\tau_p} + \frac{2\kappa_1 \cos(\omega_s\tau_1)}{\tau_{in}G_N})}{1 - \frac{2\kappa_1\tau_p \cos(\omega_s\tau_1)}{\tau_{in}}} \tag{2.8}$$

$$\omega_0\tau_1 = \omega_s\tau_1 + \frac{\kappa_1}{\tau_{in}}\tau_1\sqrt{1+\alpha^2}\sin(\omega_s\tau_1 + \arctan(\alpha)) \tag{2.9}$$

Eq.(2.8) and Eq.(2.9) are the OFI model which have been reported in many literatures.

2.2. Enhanced Sensing Performance

In dual-cavity OFI, Target-1 is moving and its surface assumed to have very low reflectivity and Target-2 is stationary and provides a high feedback. Hence, we have $\kappa_2 \gg \kappa_1$. Since Target-1 has a very low reflectivity ($\kappa_1 \ll 0.01$) and thus $\frac{2\kappa_1\tau_p \cos(\omega_s\tau_1)}{\tau_{in}} \ll 1$. For the convenience of comparison, we ignore $\frac{2\kappa_1\tau_p \cos(\omega_s\tau_1)}{\tau_{in}}$ in the denominators of Eq.(2.7) and Eq.(2.8), then Eq.(2.7) and Eq.(2.8) can be

approximated as the following two equations respectively,

$$E_s^{\,2} = \frac{DC + \frac{\tau_p}{\tau_s} * (\frac{2\kappa_2 \cos(\omega_s \tau_2)}{\tau_{in} G_N} + \frac{2\kappa_1 \cos(\omega_s \tau_1)}{\tau_{in} G_N})}{1 - \frac{2\tau_p \kappa_2 \cos(\omega_s \tau_2)}{\tau_{in}}} \tag{2.10}$$

$$E_{s\_\text{Target-1}}^2 = DC + \frac{\tau_p}{\tau_s} * \frac{2\kappa_1 \cos(\omega_s \tau_1)}{\tau_{in} G_N} \tag{2.11}$$

Where $DC = \frac{\tau_p}{\tau_s} * (J\tau_s - N_0 - \frac{1}{G_N \tau_p})$. The DC value is determined by the LD internal parameters and the injection current. It can be treated as a constant once the physical system is established.

The displacement information (L_1) relevant to Target-1 movement is carried in the term $\cos(\omega_s \tau_1)$ in Eq.(2.10) and Eq.(2.11) through $\tau_1 = 2L_1 / c$. To describe the sensing of the displacements, we introduce P_s as the OFI signal and $P_{s\_\text{Target-1}}$ as the dual-cavity OFI signal to represent the variation part in Eq.(2.10) and Eq.(2.11). Then we have,

$$P_s = E_s^2 - DC' = \frac{\frac{\tau_p}{\tau_s} * \frac{2\kappa_1 \cos(\omega_s \tau_1)}{\tau_{in} G_N}}{1 - \frac{2\tau_p \kappa_2 \cos(\omega_s \tau_2)}{\tau_{in}}} \tag{2.12}$$

$$P_{s\_\text{Target-1}} = E_{s\_\text{Target-1}}^2 - DC = \frac{\tau_p}{\tau_s} * \frac{2\kappa_1 \cos(\omega_s \tau_1)}{\tau_{in} G_N} \tag{2.13}$$

where $DC' = \frac{DC + \frac{\tau_p}{\tau_s} * (\frac{2\kappa_2 \cos(\omega_s \tau_2)}{\tau_{in} G_N})}{1 - \frac{2\tau_p \kappa_2 \cos(\omega_s \tau_2)}{\tau_{in}}}$. τ_p , τ_s and τ_{in} are LD related internal

parameters, which are fixed for a certain LD. κ_2 and $\cos(\omega_s\tau_2)$ are relate to Target-2 which is stationary and located at a certain location. Therefore, DC' can be treated as a constant. From Eq.(2.12) and Eq.(2.13), we have,

$$\frac{P_s}{P_{s-\text{Target-1}}} = \frac{1}{1-\frac{2\tau_p\kappa_2\cos(\omega_s\tau_2)}{\tau_{in}}} \tag{2.14}$$

Increasing κ_2 and setting a proper location of Target-2 to ensure that $\cos(\omega_s\tau_2)\approx 1$, we will be able to achieve $\frac{P_s}{P_{s-\text{Target-1}}} > 1$. It means that we can obtain a lager signal magnitude by using dual-cavity OFI model compared to the OFI model for the same displacement information. To increase κ_2, we can employ a target with high reflectivity surface such as mirror. To achieve $\cos(\omega_s\tau_2)\approx 1$, we can finely adjust its location by observing the laser intensity. The location is determined when the laser intensity reaches its highest value.

2.3. Simulation Verification

We implement both dual-cavity OFI model Eq.(2.7) and the OFI model Eq.(2.8) to show how the sensing sensitivity is improved. In the simulation, the LD internal parameters values are given in Table 1-1. The LD wavelength is $\lambda_0 = 780nm$, and the injection current is $J = 1.1J_{th}$, where J_{th} is the injection current threshold.

Firstly, we need to determine the location of Target-2 (denoted by L_2). Set $L_2 = L_{0\_2} + \Delta L_{0\_2}$, where L_{0_2} is the initial cavity length, it can be coarsely set as 0.05m.

ΔL_{0_2} is used to finely adjust the location of Target-2, we set a small displacement ranging from 0 to $1.5\lambda_0$. Target-2 has feedback strength with $\kappa_2 = 0.0154$. The OFI signal in Fig. 2.2 is plotted by using an OFI model with only Target-2 in present. Fig. 2.2(a) shows a small varying ΔL_{0_2} applied on Target-2 and Fig. 2.2(b) is the corresonding OFI signal of ΔL_{0_2}. The optimal location of ΔL_{0_2} is determined when the OFI signal reachs its peak at $\cos(\omega_s \tau_2) = 1$.

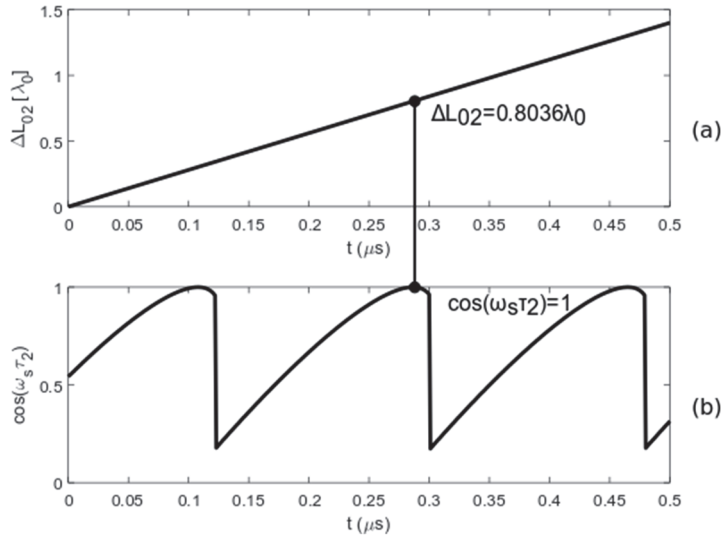

Fig. 2.2: Determining the location of Target-2 by $\cos(\omega_s \tau_2) = 1$ when $L_{0\_2} = 0.05\text{m}$ and $\kappa_2 = 0.0154$, (a) A varying ΔL_{0_2}. (b) OFI signal.

Secondly, we add Target-1 into the system. Target-1 has a weak feedback with $\kappa_1 = 0.0002$ and the initial external cavity length $L_{0\_1} = 0.7\text{m}$. It is in linear displacement ΔL_1. At this stage, Target-2 is in static, it is located at the optimal location which has determined previously. Fig. 2.3(a) shows the displacement of Target-1. The normalized OFI signals is denoted as P_s. Fig. 2.3(b) shows P_s from both dual-cavity and single-cavity OFI model. It can be seen that there is about 2 times enhancement. In Fig. 2.4, we

normalized both OFI signal in the range [-1, +1], the two signals look identical, it indicates the dual-cavity OFI has the same properties as the single-cavity OFI.

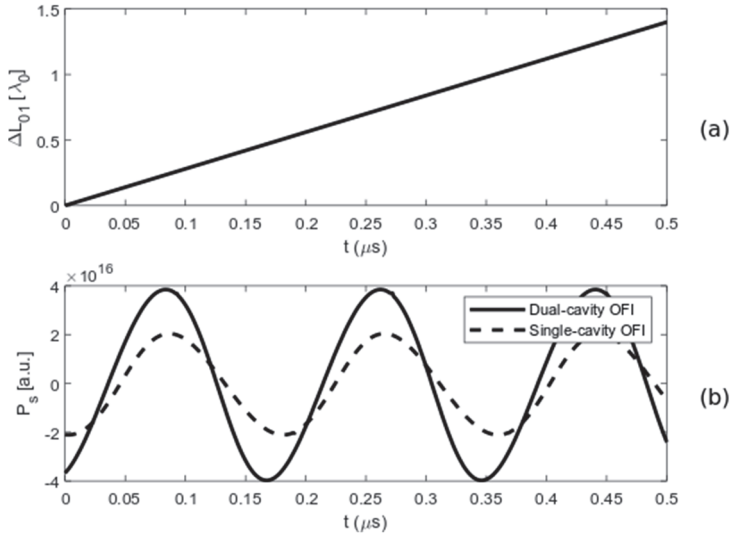

Fig. 2.3: Sensing signal comparison. (a) Displacement of Target-1. (b) Comparison of sensing signal from dual-cavity OFI and conventional single-cavity OFI with $\kappa_2 = 0.0154$.

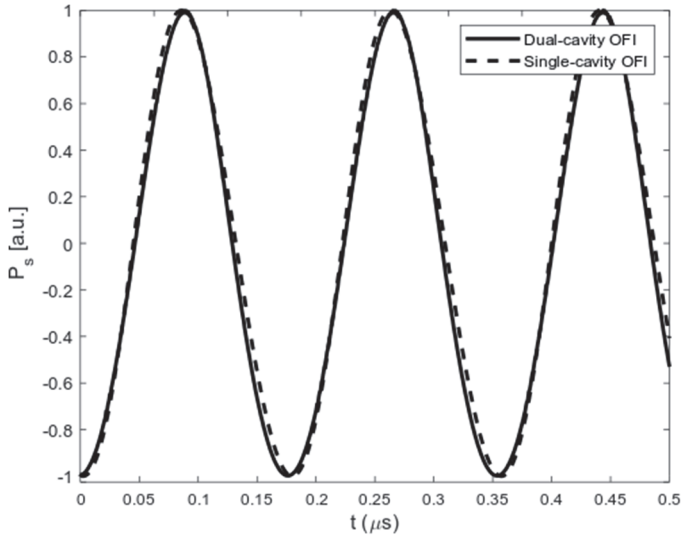

Fig. 2.4: Normalized signals in dual-cavity OFI and single-cavity OFI

It's deserve to mention that a moving Target-1 can cause a small variation in ω_s. This will have impact on $\cos(\omega_s \tau_2)$ as shown in Fig. 2.5. Regarding to the initial length of the

Target-2, According to Eq. (2.14), a larger κ_2 is prefered, hence the smaller initial length of Target-2 is recommendaned

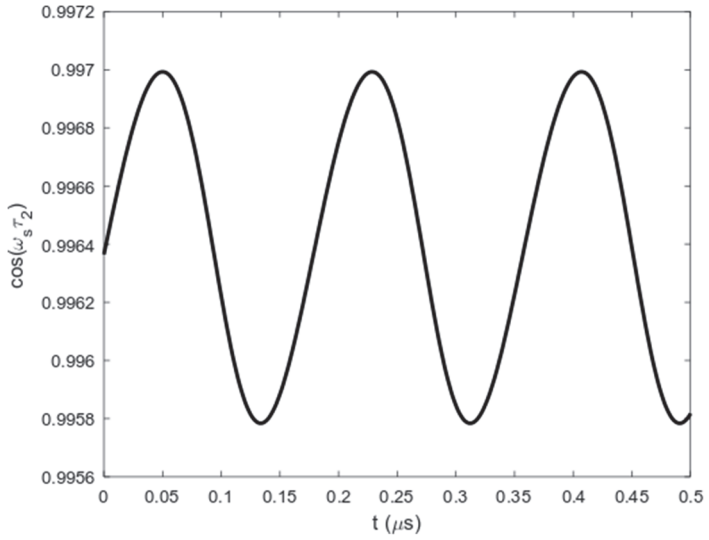

Fig. 2.5: Small variation in $\cos(\omega_s \tau_2)$ caused by Target-1 when $L_{0\_2} = 0.05m$

We now increase the feedback strength of Target-2 by setting $\kappa_2 = 0.0307$, while all other parameters remain unchange. The result is shown in Fig. 2.6(b). It can be seen that a larger magnitude for the dual-cavity OFI signal is obtained and the magnitude is enhanced about 4.5 times.

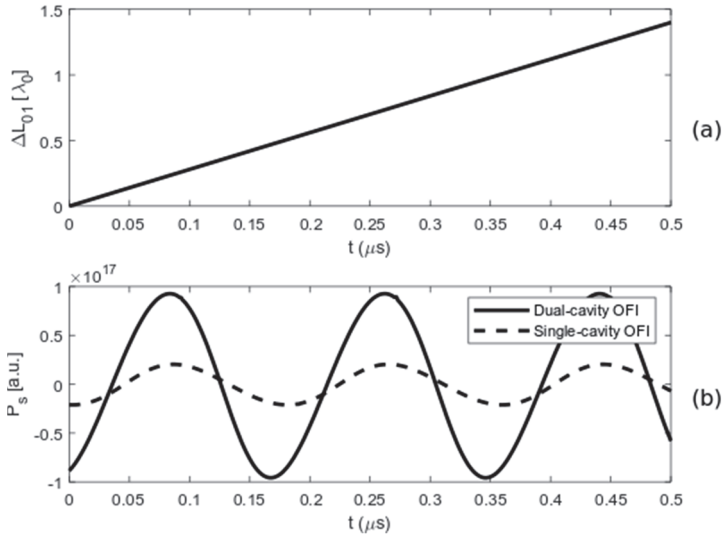

Fig. 2.6: Sensing signal comparison. (a) Displacement of Target-1. (b) Comparison of sensing signals from dual-cavity OFI and conventional single-cavity OFI with $L_{0\_2} = 0.05m$ and $\kappa_2 = 0.0307$.

2.4. Experimental Verification

To verify the proposed method, we further built an experimental system presented in Fig. 2.7. A single mode laser diode (Hatachi HL8325G, λ_0=830 nm, output power $P_0 = 40\ mW$) is employed in this physical system. The LD is driven and temperature-stabilized by a LD controller (Thorlabs, ITC4001) at the injection current of 90mA and the temperature of $23 \pm 0.002^\circ C$. The light emitted by the LD is focused by a lens then splited into two light beams by a beam splitter (BS) with spliting ratio of 50:50. One beam is directed to the Target-1 whose displacement is to be measured. The other beam is directed to the Target-2 for providing high feedback. The Target-1 is a piezoelectric transducer (PZT) (Thorlabs, PAS005). A piece of paper is glued on the PZT head to provide a weak feedback. The PZT (PAS005) has a displacement resolution of 20nm, driven by a PZT controller (Thorlabs, MDT694) by applying a sinusoidal driving signal. Another PZT (PI P-841.20) with higher displacement resolution is employed as Target-2

used for providing feedback. To provide a high feedback by Target-2, a mirror is glued on the head of this PZT. The PZT is driven by a controller (PI E-625). We use this PZT to finely adjust the location of Target-2 to meet the requirement of $\cos(\omega_s \tau_2) \approx 1$. A variable attenuator (VA) (Thorlabs, NDC-50C-2M-B) is inserted between the beam splitter and Target-2. The VA is continuously variable density filter with angular graduations mounted on an rotating axle which can be used to continuously adjust the feedback strength, in this experiment it is used to adjust the feedback strength of Target-2. The photodiode (PD) packaged at the rear of the LD is connected to a detection circuit to detect OFI signal. Finally, the OFI signal is captured, recorded and displayed by a digital oscilloscope.

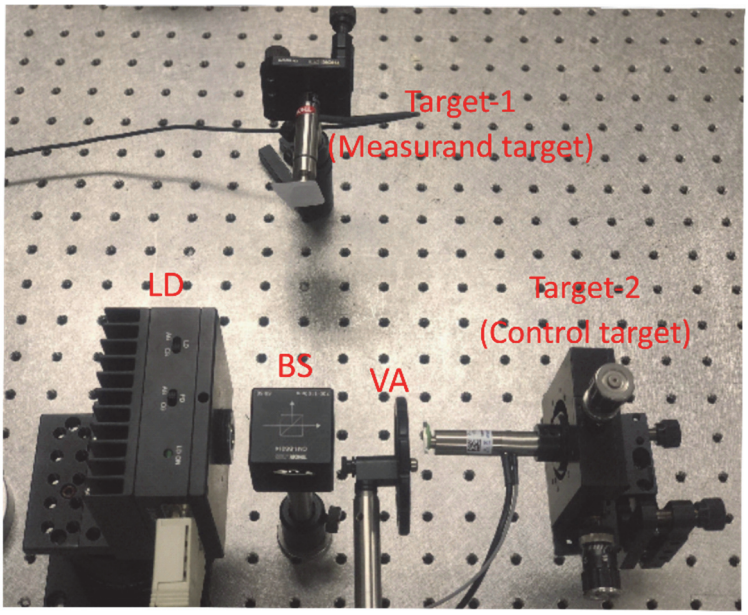

Fig. 2.7: Experimental system with dual-cavity configuration.

The experiment is carried out in the following the procedure:

1. Firstly, remove Target-2 from Fig. 2.7, with only Target-1, we observe an OFI signal using the experimental system established. Apply an displacement on Target-1 by the PZT (PAS005). The controlling voltage signal from a signal generator applied on the

PZT driver is an sinusodial signal with freqeuncy of 200Hz ,amplitude of 3V. According to the datasheet, 0.1V controlling voltage leads to 27nm displacement of the PZT. The initial external cavity length of Target-1 is 0.25m. As the surface of Target-1 has very low reflectivity, the OFI signal recorded by the oscilloscopt looks blurred, shown on Fig. 2.8(a).

2. Then block the light beam refected from Target-1. The system now only have optical feedback from Target-2. We adjust the location for Target-2 to meet $\cos(\omega_s \tau_2) = 1$. Rotate the VA which is located between the PZT (P-841.20) and the spiliter so that the system with Target-2 works at moderate regim. Target-2 is placed at 0.10m away from the LD. Moving Target-2 linearly by applying a controlling valtage signal changing from 0V to 1V. The corresponding OFI signal can be observed and recorded by the digital oscillocope. From the signal waveform, we can lock the location of Target-2 when the signal reach its peak where we have $\cos(\omega_s \tau_2)$ close to 1. Note this PZT has a displacment resolution of 9nm. We can use this PZT to accurately determine the location.
3. Allow the two targets on the system, the system will receive optical feedbacks from both Target-1 and Target-2. Target-1 is moving as described in step 1. Target-2 is stationary at the location determinded in step 2. Then, we can obtain and an dual-cavity OFI signal P_s.
4. Starting from step 3, we further finely adjust the location of Target-2 to observe the influence of its location on P_s. The PZT (PI P-841.20) has PC controlled function. We can use a computer to adjust its movement with 10nm each time. In this case, about 40 different locations can be set within $\lambda_0 / 2$. We can observe how the

magnitude of P_s is changed with the locations.

5. At last, we observe the influence of feedback strength provided by Target-2 on P_s by setting Target-2 at a certain location, e.g., the location obtained in step 2. Rotate the VA to get different feedback strength and record the corresponding OFI signal P_s.

Amount the observed signals, we selected three locations with visiable enhancement ratio. They are presented in Fig. 2.8 and Fig. 2.9. Fig. 2.8(a) is a blurred OFI signal corresponding to the displacement of Target-1, recorded in step 1. It can be read OFI signal is nearly burried in noise. The peak-peak value of the recorded signal is about 10mv. Note that the second feedback is not applied to the experimental system at this step. Fig. 2.8(b) is the dual-cavity OFI signal P_s with Target-2 added to the experimental system, recorded in step 3. It shows the magnitude of the recorded signal has been significant enhanced due to the feedback from Target-2. Fig. 2.8(c) and (d) are P_s with same feedback strength but different locations of Target-2, recorded in step 4. The peak-peak values of the OFI signals in (b), (c) and (d) are about 35mV, 25mV, and 15mV respectively. It can be seen the magnitude of P_s can be enhanced at these locations with different enhancement ratio. With the current setup, we are able to make the blurred OFI signal much clear and enhance its magnitude to 3.5 times, as shown in Fig. 2.8(b).

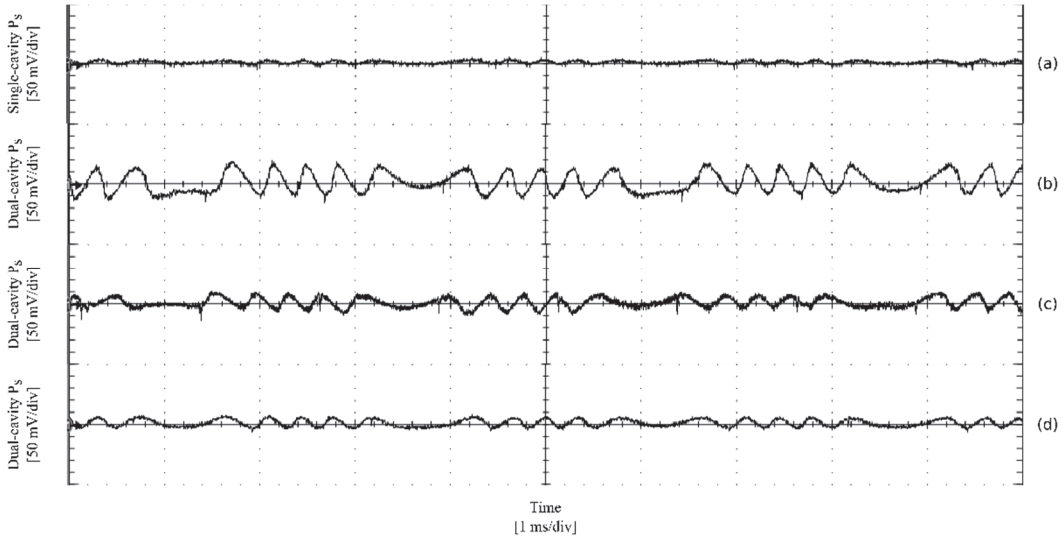

Fig. 2.8: Influence of Target-2 location. (a) OFI signal with Target-1 only. (b),(c),(d) Dual-cavity OFI signals with different locations but same feedback strength.

Another set of experiment results are presented in Fig. 2.9. based on the result in Fig. 2.8(b), we keep the location of Target-2 unchanged, and change the feedback strength of Target-2 and record the corresponding P_s, as described in step 5. The recorded signals are shown in Fig. 2.9(b), (c) and (d). The signal in Fig. 2.9(b) is with the same location and feedback strength from Target-2 as in Fig. 2.8(b). Fig. 2.9(a) is the same blurred OFI signal as in Fig. 2.8(a). Comparing to Fig. 2.9(b), Fig. 2.9(c) is the case that Target-2 has lower feedback strength and whereas in Fig. 2.9(d) it has higher strength compared to the feedback in (b). The peak-peak values in Fig. 2.9(b), (c) and (d) are about 35mV, 20mV and 50mV respectively, with enhancment factor as 3.5, 2.0 and 5.0. Obviously, a higher feedback strength of Target-2 can lead to a larger magnitude in P_s.

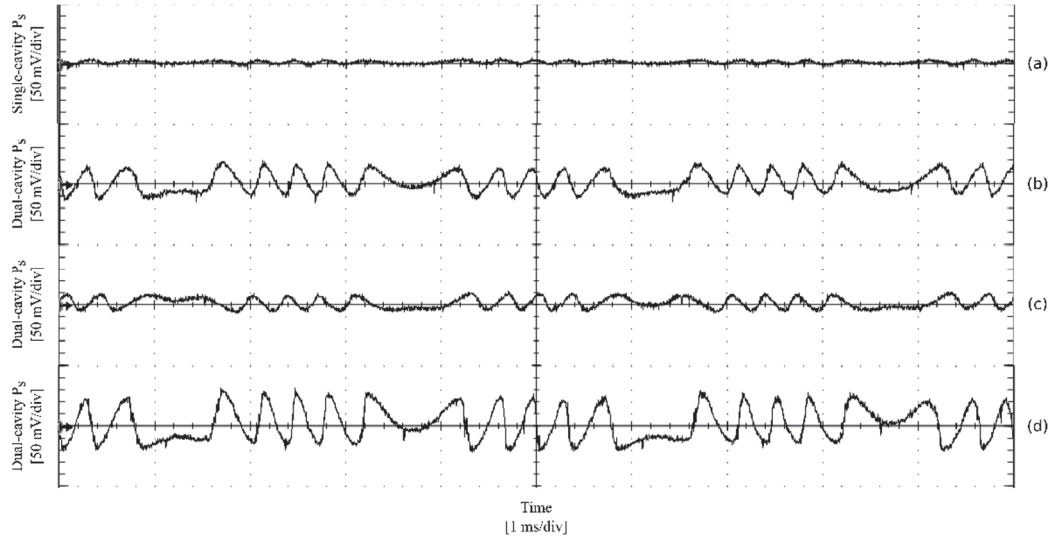

Fig. 2.9: Influence of dual-feedback strength; (a) OFI signal with Target-1 only. (b), (c), (d) Dual-cavity OFI signals with different feedback strength but same location of Target-2.

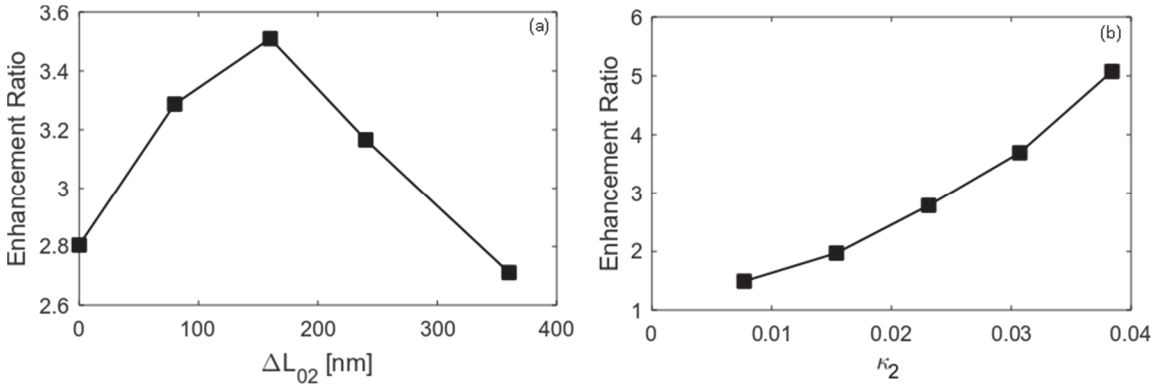

Fig. 2.10: Signal enhancement performance. a) Different control cavity lengths with $\kappa_2 = 0.0327$, (b) Different control target feedback strengths with $\Delta L_{0\_2} = 160\ nm$

Further analysis of Target-2's location and feedback strength on the enhacement ratio is shown in Fig. 2.10. Fig. 2.10 (a) shows that the location of Target-2 needs to be choosen by satisfying to ensure a larger ehancement ratio for a fixed feedback strength. Fig. 2.10(b) shows that the enhancment ratio goes up with the increase of the feedback strength for a fixed location of Target-2. the above experiments varified the proposed daul-cavity OFI system has capability to improve the OFI signal quality in terms of large signal

magnitude.

2.5. Summary

In this chapter, we utilized the dual-cavity OFI configuration to improve the performance of the conventional single-cavity OFI. Follow the principle of the single-cavity OFI model, we derived the dual-cavity OFI model from the steady state solutions of the dual-cavity L-K equations. A mathematic expression was obtained to describe the enhancement of the sensing signal, which also elaborates the way to enhance the signal by controlling the feedback strength and the length of the second cavity. Our simulation shows the dual-cavity and single-cavity OFI signals are identical when normalized them in the same range. This means the dual-cavity OFI signal has the same properties as the single-cavity OFI signal can be used for sensing applications. The results also show the signal enhancement will increase with feedback strength of the control target. However such relationship does not exist for the control cavity length. A fine adjustment for the control cavity length is needed to ensure the dual-cavity system has the maximum enhancement. An experiment was conducted to valid the proposed method. The results show with the adjustment of the feedback strength of the control target and control cavity length, the dual-cavity OFI can give 2-5 times sensitivity improvement compare to the single-cavity OFI. It is in a good agreement with the simulation results. The proposed dual-cavity OFI system addressed the issue of an OFI system with degraded sensing sensitive due to the weak optical feedback of the measurand target. The second cavity effectively improved the sensing sensitive without any physical changes on the measurand target. It provides important guidance for designing a practical OFI based sensor. The journal publication based on this work can be found in [121].

Chapter 3. Sensing at Period-One State -- A New Sensing Scheme

3.1. Dynamic States

The numerical study of L-K equations unveils a number of complex dynamical states, including Steady (S) state, Period-One (P1) oscillation state, Quasi-periodic (QP) state and Chaos (C). Various potential applications have been investigated and reported in different dynamic states. In steady state, a LD with optical feedback being utilized to detect the Doppler shift, vibration, velocity measurement, and displacement [49, 57, 122, 123]. In P1 state, a large sideband-rejection-ratio is obtained, with this unique advantage, P1 oscillation can be used to generate microwave photonic signal for sensing and fiber-optic radio communication [124-128]. In quasi-period state, LD with the influence from feedback will generate subwavelength, by monitoring frequency shift can achieve multi-dimensional 2D measurement [129]. In chaos, due to the broad bandwidth and pseudo-randomness of chaotic oscillation, it can be implemented in chaotic radar and chaotic secure communication [130-132], et al.

The dynamic states can be identified by observing the laser intensity waveform which is obtained through solving the L-K equations. An example of the waveform in their corresponding state is shown in Fig. 3.1.

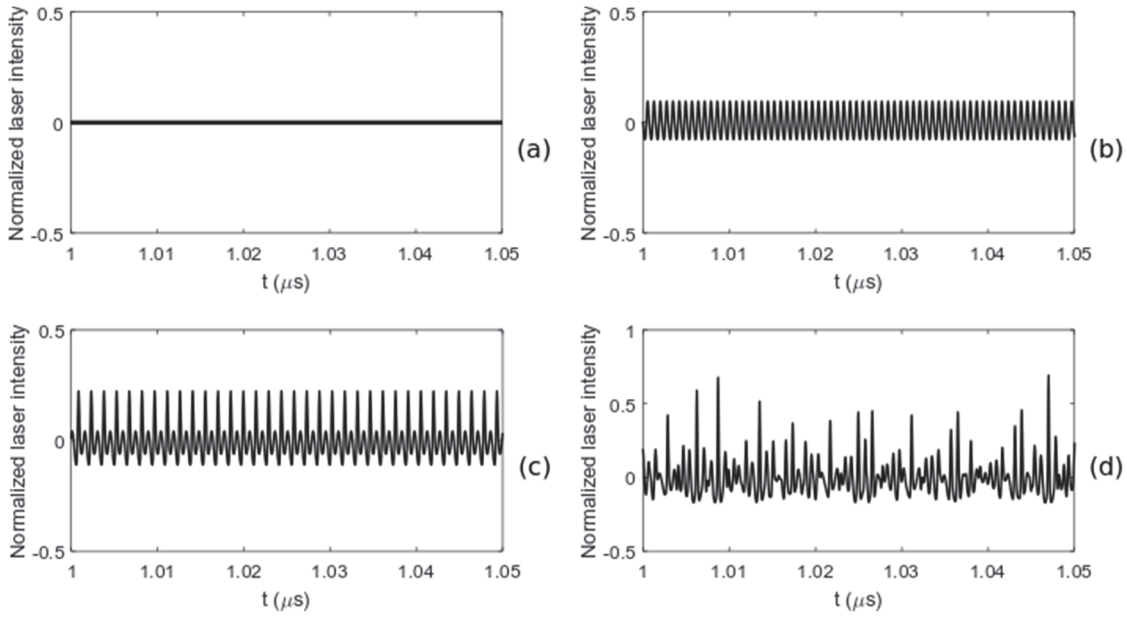

Fig. 3.1: Laser intensity waveforms in different dynamic states. (a) Steady state. (b) Period-One oscillation state. (c) Quasi-Periodic oscillation state. (d) Chaos.

The transition from steady state to chaos through various states when one of the system parameter values change is called bifurcation. A bifurcation diagram can be created by sampling the local maxima (or minima) of the laser intensity waveforms. A set of the local maxima is plotted along the vertical axis (laser intensity) at a fixed LD parameter value, e.g. external cavity length, feedback strength, injection current etc. Then, when the parameter value is slightly increased (or decreased), a new waveform is obtained at a new fixed parameter value and the local maxima of the waveform are sampled and plotted again [133]. This procedure is repeated to create a bifurcation diagram. In Fig. 3.2, two examples of the bifurcation diagrams are given. Fig. 3.2(a) show the bifurcation of a single-cavity OFI with $\alpha = 3$, $J = 1.1J_{th}$, and $L = 0.2m$, the optical feedback strength κ is used as the variable parameter. The LD experiences Steady, P1, QP and Chaos states. In Fig. 3.2(b), the fixed parameters are $\alpha = 2$, $J = 1.3J_{th}$, and $\kappa = 0.125$. The external cavity length L is used as the variable, the LD experiences Steady, Chaos, P1 Steady then

Chaos. In the next section, we will focus on OFI sensing characters at steady and P1 state.

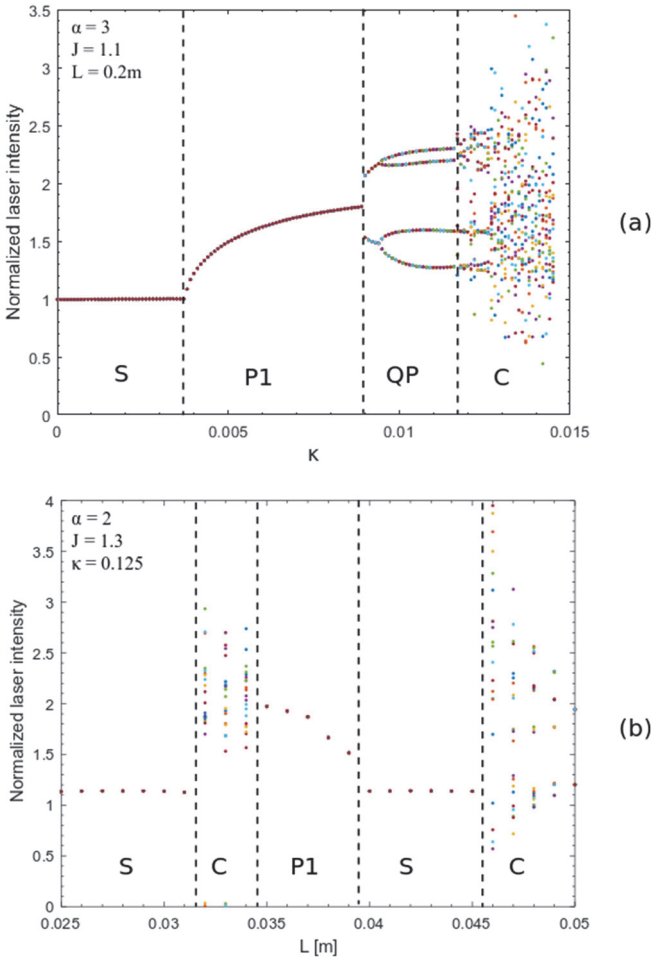

Fig. 3.2: Two examples of single-cavity OFI bifurcation diagram. (a) Bifurcation diagram with κ as variable. (b) Bifurcation diagram with L as variable.

3.2. Validity of Existing OFI Model

The OFI model and their applications are based on an assumption that the system operates in stable state, that is both the electric field $E(t)$ and carrier density $N(t)$ in a LD with a stationary external cavity can reach a constant after a transient period. With the changes of the system parameters, e.g. feedback strength, LD injection current, the system will leave the steady state, entering other states and exhibits complicated dynamics. The work

in [134] observed a high frequency component exists in the OFI signal under the moderate feedback regime. Although the authors did not explicit say the LD is no longer in the steady state, it has implied the OFI model is not able to correctly describe the signal anymore. It is possible that the LD has entered other state under the moderate feedback regime. In this case, a modulated laser intensity obtained by the OFI model will be different from the one using the L-K equations. In the following, we study the validity of the OFI system models through the analysis on the laser intensity waveform that generated from both L-K equations and OFI model. As mentioned in Section 3.1, a bifurcation diagram is used to investigate LD dynamic states for the change of a certain parameter. However, it has lack of information of the OFI feedback regimes which is classified by feedback level C. We present a bifurcation diagram that contains both dynamic states and C factor, this allows us to clearly identify how the states and regimes are corresponded. It can be used as a guide on when to use the L-K equations and OFI model to describe the laser intensity waveform.

The bifurcation diagram in Fig. 3.3 was induced by optical feedback strength in an LD. The vertical axis is LD intensity values of the local peaks of the waveform, it is defined as $E^2(t)/E_0^2$, where E_0^2 is the intensity of the LD without optical feedback. The top horizontal axis is the parameter of the optical feedback level C and the bottom horizontal axis is the optical feedback strength κ. The LD related parameters are set as follow, $\lambda_0 = 780nm$, $\alpha = 3$, $J = 1.3J_{th}$, where J_{th} is the injection current density threshold. The target is in static mode with initial external cavity length $L_0 = 0.24m$. According to the feedback regimes and dynamic states, the bifurcation diagram can be divided into five operation regions. Region I: LD is in steady state and with weak feedback. Region II: LD

is in steady state and with moderate feedback. Region III: LD is in P1 state and with moderate feedback. Region IV: LD is in P1 state and with strong feedback. Region V: LD is in qusi-periodic or chaos state and with strong feedback. Next, we will investigate the OFI signal waveforms by using the OFI model and L-K equations.

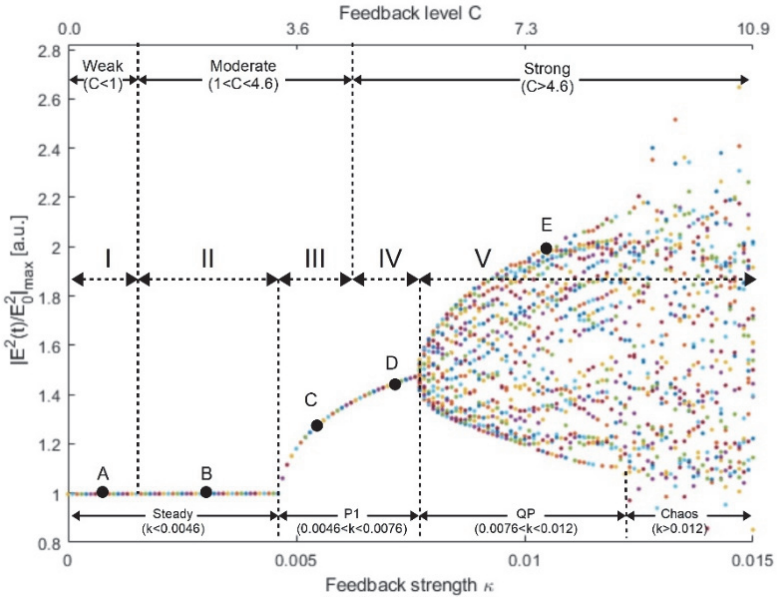

Fig. 3.3: Bifurcation diagram of an OFI system, with $\alpha = 3$, $J = 1.3J_{th}$ and $L_0 = 0.24m$.

3.2.1. Comparison of Sensing Waveform Generated from OFI Model and L-K Equations

For the recognized five operation regions shown on Fig. 3.3, we choose a working point in each region denoted by A,B,C,D and E respectively. At each point, we performed three groups simulations to obtain the laser intensity waveform $I(t)$ (A relative laser intensity $I(t) = (E^2(t) - \overline{E^2(t)}) / E_0^2$ is used, where $\overline{E^2(t)}$ is the mean of $E^2(t)$ and E_0^2). The first group use the OFI model described by Eq.(1.15) $\phi_s = \phi_0 - C\sin[\phi_s + \arctan(\alpha)]$ and Eq.(1.21) $P = \Delta P \kappa \cos(\phi_s)$ to obtain $I(t)$, the second group use L-K equations Eq.(1.1)

-Eq.(1.3) to obtain $I(t)$, the third group also use L-K equations, but with a 500MHz low-pass filter applied on the results. In all these simulations, the system and LD parameters setting are same as those used to generate the bifurcation diagram. The target has a reciprocating movement with a sinusoid displacement waveform shown in Fig. 3.4 (a).

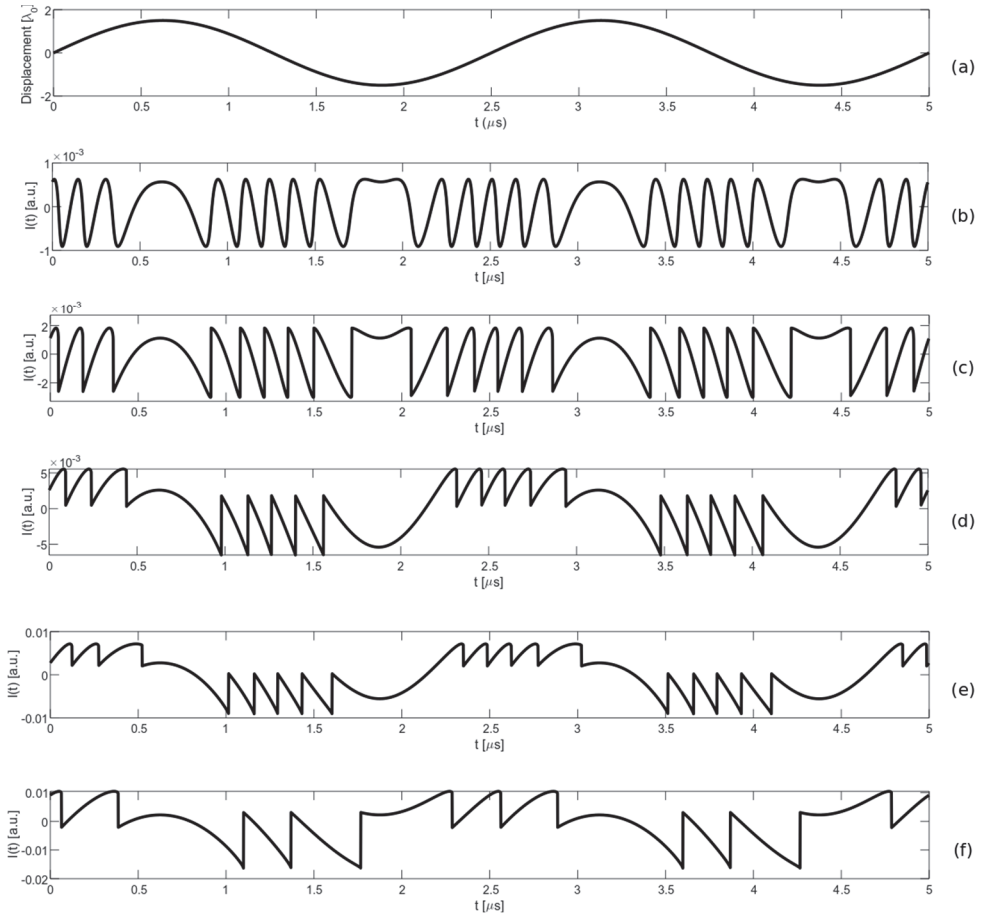

Fig. 3.4: Laser intensity waveforms $I(t)$ obtained from the OFI model. (a): Displacement of the target. (b): $I(t)$ at point A in Region I (c): $I(t)$ at point B in Region II. (d): $I(t)$ at point C in Region III. (e): $I(t)$ at point D in Region IV. (f): $I(t)$ at point E in Region V.

The laser intensity waveforms $I(t)$ obtained from OFI model are shown in Fig. 3.4 (b)-(f), they are the corresponding $I(t)$ at point A: $C = 0.50$ (κ=0.0007), B: $C = 1.60$ (κ=0.0022), C: $C = 4.00$ (κ=0.0055), D: $C = 5.38$ (κ=0.0074), and E:

$C = 8.95$ (κ=0.0123) respectively. From Fig. 3.4(b)-(e), as the feedback factor C increases, the shape of the fringes changed from sinusoidal to sawtooth like waveform and the signal amplitude also increased. In Fig. 3.4(f), $I(t)$ was obtained in region V, there are only three fringes compare to five fringes in Region I to IV. So there is a signaficant fringe loss [105-107].

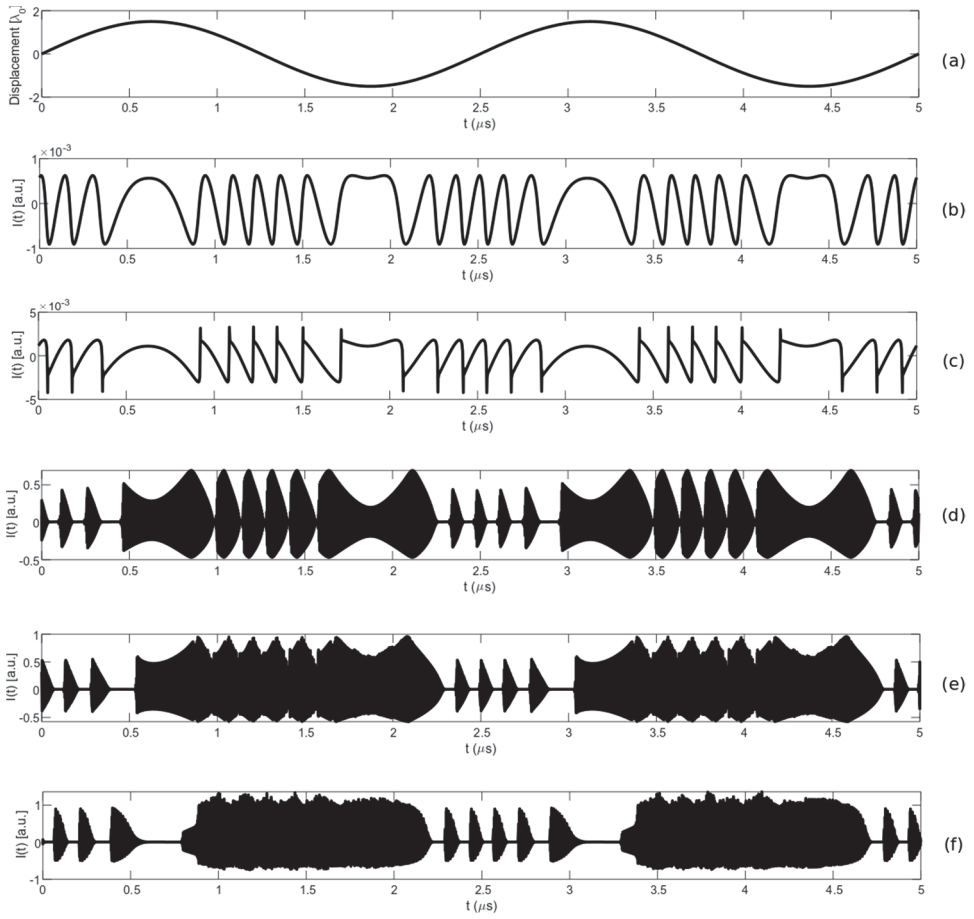

Fig. 3.5: Laser intensity waveforms $I(t)$ obtained from the L-K equations. (a): Displacement of the target. (b): $I(t)$ at point A in Region I (c): $I(t)$ at point B in Region II. (d): $I(t)$ at point C in Region III. (e): $I(t)$ at point D in Region IV. (f): $I(t)$ at point E in Region V.

The laser intensity waveforms $I(t)$ obtained through solving the L-K equations are shown in Fig. 3.5. Comparing Fig. 3.5 (b) and (c) with Fig. 3.4 (b) and (c), their

corresponding $I(t)$ has the same peak value and phase. It is as expected that their waveforms are identical, due to both region I and region II are operate in steady state. Fig. 3.5 (d)-(e) show very different waveform compared them with Fig. 3.4 (d)-(e). It was reported in [135] that the LD operates above steady state, the laser intensity waveform exhibit a form of high frequency oscillation with its amplitude modulated by a slow-varying signal. The slow-varying envelop is similar to the $I(t)$ in the steady state. The amplitude of $I(t)$ is increasing with the feedback strength. Although, Fig. 3.5 (d), (e) do not have clear fringes, with appropriate signal processing technique, it may still be able to provide displacement information about the target. Fig. 3.5 (f) shows the $I(t)$ in region V, the envelop becomes unclear, the whole signal is blurry. It can also be noticed in Fig. 3.5 (d)-(f) that there are areas between the fringes where high frequency oscillation does not exist and its amplitude is significantly smaller than other parts, this indicates that at certain movements the system is switching between states.

In a pratical system, the detection of the laser intensity was done by the in-built PD which is commenly attached at the back of a comerical LD. However, the bandwidth of the in-built PD is usually less than 1GHz. Due to the limit in the rising time of the PD, it is not able to detect the high frequency components of laser intensity waveform when LD enters other states. Therefore, the waveform observed in region III to V through internal PD would be a distorted. So in the third group simulations, we applied a filter with cut-off frequency at 500MHz on the waveforms obtained in Fig. 3.5. This low-pass filter imitates the in-built PD that suppress the high frequencies components in the waveforms. The filter applied results are shown in Fig. 3.6. It can be seen the high frequencies in Fig. 3.6

(d)-(f) are filtered out. Although, $I(t)$ still has sprinkle, they have the same fringe numbers and appromixted same amplitude with the $I(t)$ in Fig. 3.4 (d)-(e).

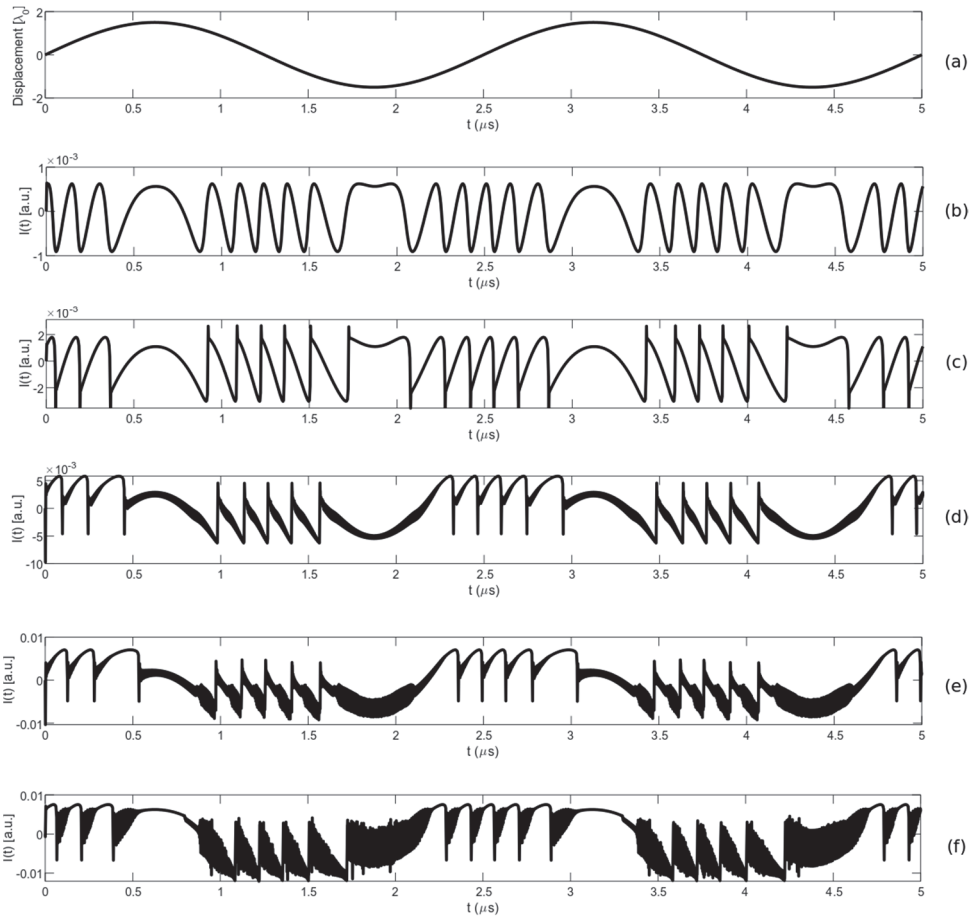

Fig. 3.6: Laser intensity waveforms $I(t)$ with 500MHz filter applied. (a): Displacement of the target. (b): $I(t)$ at point A in Region I (c): $I(t)$ at point B in Region II. (d): $I(t)$ at point C in Region III. (e): $I(t)$ at point D in Region IV. (f): $I(t)$ at point E in Region V.

From the comparison of the three groups' simulations, we concluded that the existing OFI model can only correctly describe an OFI sensing signal waveform in Region I and Region II. When LD operates in Region III and above, the L-K equations should be used to describe the OFI signal waveform.

3.2.2. Experiment Observation

An experimental system is built and depicted in Fig. 3.7 to observe laser intensity signal. The LD (HL8325G, Hitachi, Tokyo, Japan) is a single mode quantum well laser with an emitting wavelength of 830 nm and a maximum output power (P) of 40 mW. The LD is driven and temperature-stabilized by an LD controller (Thorlabs, ITC4001) with the injection current of 75mA and the temperature of $23 \pm 0.002\,^{\circ}\mathrm{C}$. The light emitted by the LD is focused by a lens and then splited into two light beams by a beam splitter (BS) with splitting ratio of 50:50. One beam is directed to the Target which is a piezoelectric transducer (PZT) (PI P-841.20) with a mirror surface for providing optical feedback to the LD. A variable attenuator (VA) is inserted inbetween the BS and the Target to adjust the feedback amount to ensure that the LD can operate at different dynamic states/feedback regimes. Since the intensicity waveform $I(t)$ can exhibits high frequency, so the other beam from the BS is directed to the external fast PD with a bandwidth of 9.5 GHz (Thorlabs, PDA8GS). The detected $I(t)$ from both external fast PD and internal PD are collected and recorded by a high-speed digital oscilloscope (Tektronix DAS 70804). With the current setup, we are able to observe the $I(t)$ in region I,II, and III. The relevant experimental steps are described as below:

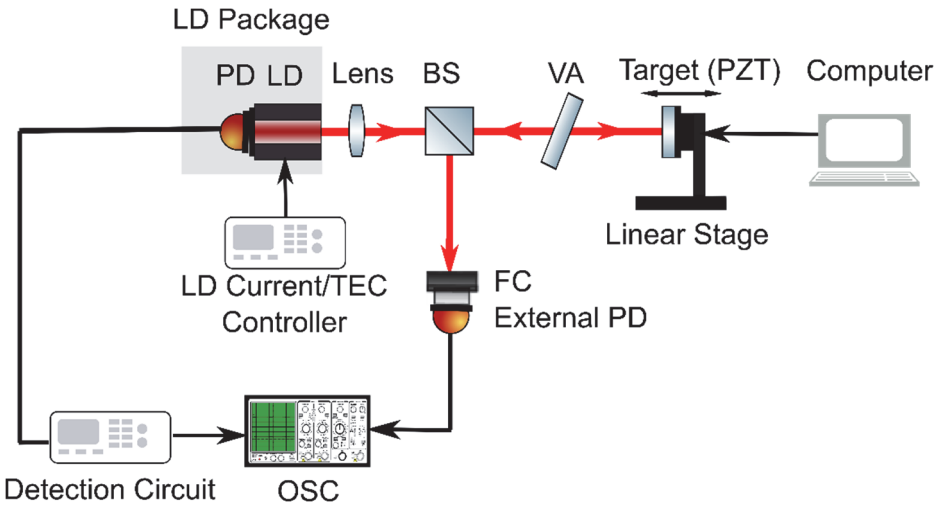

Fig. 3.7: Experimental comparison.

We apply a displacement on the target, the controlling voltage signal from a signal generator applied on the PZT driver is a sinusodial signal with freqeuncy of 200Hz, amplitude of 0.4V. The initial external cavity length of the target is 0.25m. Adjust the VA to vary the feedback strength from low to high, and record three $I(t)$ waveforms at different feedback levels.

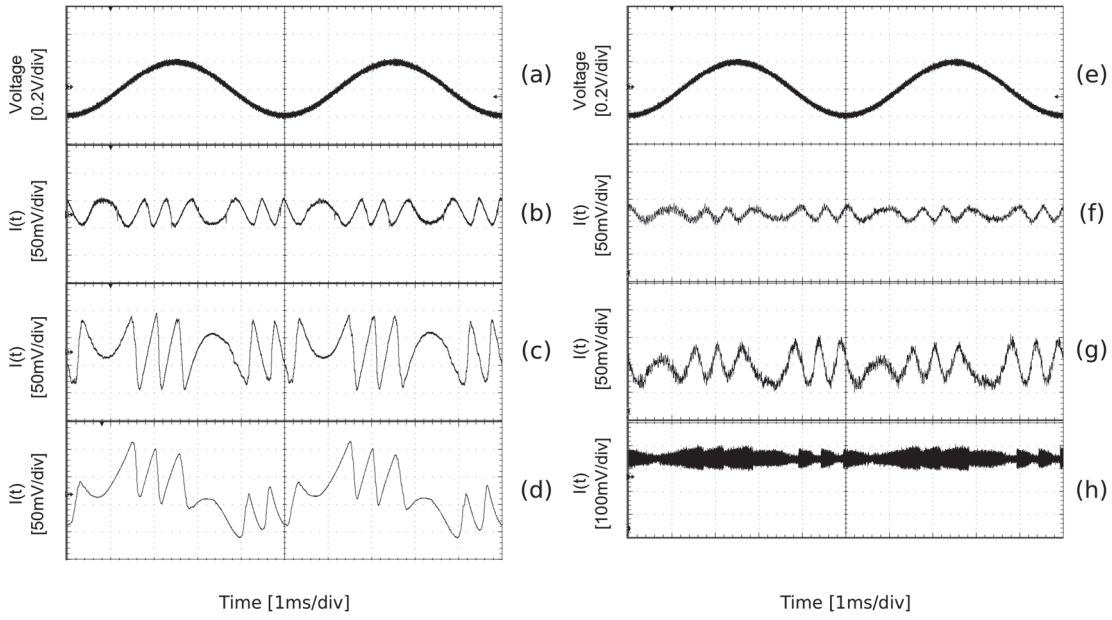

Fig. 3.8: Experimental results. (a), (e): Controlling signal applied to the PZT. (b)-(d): $I(t)$ from the internal PD. (f)-(h): $I(t)$ from the external PD.

Fig. 3.8 shows the experimental results from two PDs with different bandwidths. Fig. 3.8 (b), (c), (d) show $I(t)$ obtained from the internal PD which is packaged at the rear of the LD, while Fig. 3.8 (f), (g), (h) show $I(t)$ obtained from the external PD with a bandwidth of 9.5 GHz. Each row in the figure are captured under the same laser operation conditions, i.e. same injection current, initial external cavity length and optical feedback level, but different photodetectors. Fig. 3.8 (a) and (e) are the driving signals applied on the PZT. For the PZT in the experiments, each 0.1 V contributes to 330 nm displacement. The peak to valley value of the voltage in (a) and (e) is about 0.4V, i.e. 1320 nm displacement. From top to bottom, the optical feedback strength increases. For Fig. 3.8 (b) and (f), $I(t)$ is obtained in region I. For Fig. 3.8 (c) and (g), $I(t)$ is obtained in region II. It can be found in region I and II, the $I(t)$ from both PDs are similar. $I(t)$ in region I are showing sinusoidal waveforms and in region II are saw-tooth like waveforms. The amplitude increases with the feedback strength. We can conclude that both OFI model and L-K equations can be used to describe its behaviour. With the increase of feedback strength, the system enters region III. Fig. 3.8 (d) is the $I(t)$ obtained from the internal PD. It shows saw-tooth like waveform, but the amplitude of each fringe are no longer in the same level. Fig. 3.8 (h) is the $I(t)$ obtained from the external PD. The high frequency component can be observed with its amplitude modulated by a slow-varying signal. The results in region III show the observed laser intensity from the internal PD may not be the original signal due to the limitation of its bandwidth, using the OFI model to describe the signal is not valid, instead the L-K equations should be used to characterise the behaviour of the signal in this region. Although the OFI signal waveforms are complicated in Region III to V, they contain rich information related to a moving target. In the next section, we

will explain the sensing capability in these regions.

3.3. A New Sensing Scheme

With the increase of the optical feedback level, an LD will leave the steady state and enter other operation states such as P1, QP, chaos, and rich dynamics can then be observed. Our work in [135] showcased the sensing capability of an OFI system with a moving target and high level optical feedback operating above the steady boundary. In this case, the laser intensity signal contains very high frequency components and its amplitude is modulated and exhibited a clear envelop, which contains the displacement information of the external target. The work in [135] opened a way to achieve more sensitive sensing using laser dynamics. However, the problem with the work is that the laser intensity exhibits very complicated waveform due to the moving target with high feedback. It is not easy to ensure that the system has a stable performance during the measurement because the LD may switch among different states. To solve this problem, a dual-cavity OFI system operates in P1 state is proposed. As shown in Fig. 3.9, the second target (Target-2/Control target) is added to the conventional single-cavity OFI. The cavity between the LD to the Control target is named as the control cavity since it will be used to control the dynamic of the system. The target which associated with quantities to be measured named as Target-1 or the measurand target. The cavity between the LD to measurand target is called the measurand cavity. Through a proper parameters settings and adjustment of the control cavity, the dual-cavity OFI system will operate in P1 state.

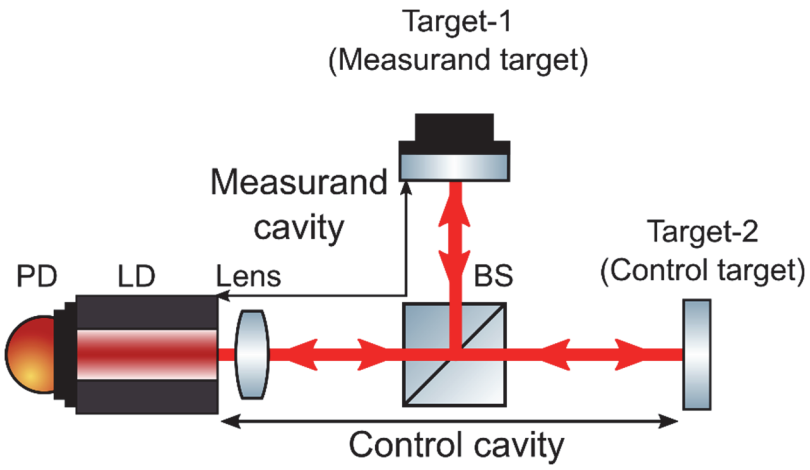

Fig. 3.9: Dual-cavity OFI system operates in P1 state.

Based on the dual-cavity OFI system described in Chapter 2, we developed a bifurcation diagram through solving the dual-cavity L-K equations Eq. (2.1)-Eq.(2.3). The vertical axis is the laser intensity values of the local peaks of the waveform, it is defined as $(E^2(t)/E_0^2)$, where E_0^2 is the intensity of the LD without optical feedback. The horizontal axis is the optical feedback strength of Target-2 κ_2. Meanwhile, through the relationship $C=\frac{\kappa}{\tau_{in}}\tau\sqrt{1+\alpha^2}$, we added the optical feedback level C_2 on the bifurcation diagram. The parameter settings for the dual-cavity OFI system are as follows. We set $J=1.3J_{th}$, $\alpha=3$ and the LD wavelength is $\lambda_0=780nm$. Target-1 related parameters are initial cavity length $L_{01}=0.10m$ and feedback level $C_1=0.1$. Target-2 related parameters are initial cavity length $L_{02}=0.24m$.The values for the internal LD parameters are listed in Table 1-1. The bifurcation diagram for the dual-cavity OFI is shown in Fig. 3.10. It can be seen, the dual-cavity OFI system with varying κ_2 experienced Steady, P1 QP states and Chaos. In steady state, C_2 ranges from 0 to 3.6, this corresponded to weak feedback regime and partial moderate feedback regime. Most of existing OFI model including the work in

Chapter 2 are working in this state. The P1 state which C_2 covers from 3.6 to 5.5, includes partial moderate and strong feedback regime. Our proposed sensing scheme will be working in this P1 state, it was labelled as the "New sensing scheme region" on the bifurcation diagram. The QP and Chaos corresponded the strong feedback regime, C_2 is above 5.5.

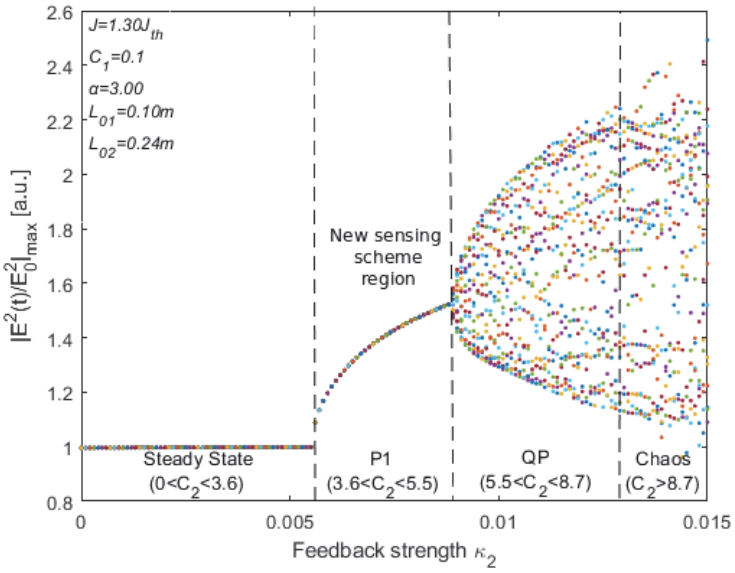

Fig. 3.10: Bifurcation diagram for dual-cavity OFI.

3.3.1. Theoretical Investigation

We define P_s as the varying laser intensity with only Target-1 in use and the LD operates at steady state. P_{P1} represents when both Target-1 and Target-2 are in use and LD operates at P1 state. For the OFI with only Target-1, Target-1 is set in reciprocating movement with a triangular displacement waveform as shown in Fig. 3.11(a). Through solving the L-K equations Eq.(1.1)-Eq.(1.3), we can get a P_s corresponding to Target-1's movement.

Fig. 3.11(b). shows the corresponding P_s with $C_1 = 0.1$, and the peak-valley (denoted as P-V) value is 6.92×10^{-4} (a.u.).

Then, we consider the dual-cavity OFI, where both Target-1 and Target-2 are involved and the LD operates at P1 state. Target-1 related parameters remain unchanged, while Target-2 is set in stationary with $L_{02} = 0.24m$ and $C_2 = 4.0$. The same displacement signal shown in Fig. 3.11(a) is applied on Target-1. The P_{P1} corresponding to the displacement is presented in Fig. 3.12, where we find that P_{P1} exhibits a high frequency oscillation at 2.28 GHz with its amplitude modulated by a slow-varying signal.

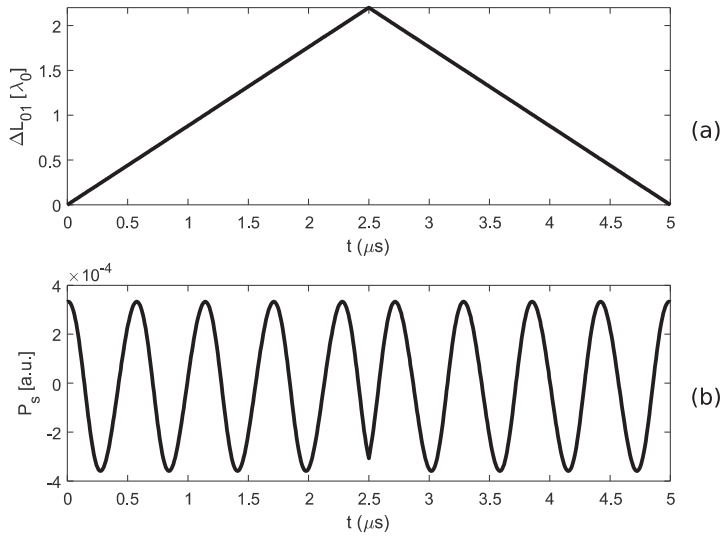

Fig. 3.11: Varying laser intensity P_s with Target-1 only. (a) Triangular displacement applied on Target-1. (b) P_s with $L_{01} = 0.10m$ and $C_1 = 0.1$.

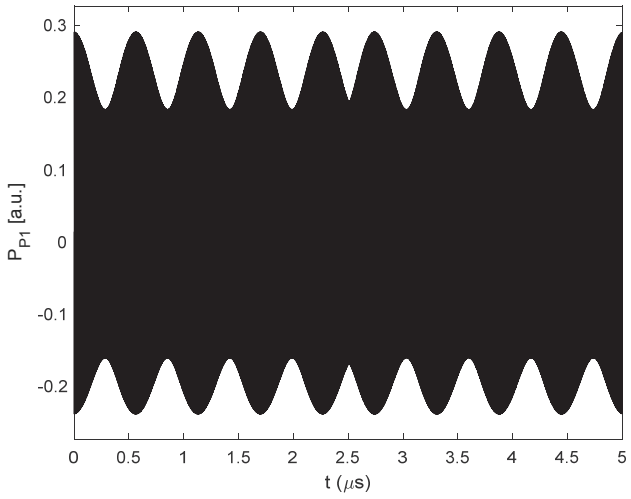

Fig. 3.12: Varying laser intensity P_{P1} with both targets when $L_{01} = 0.10m$, $L_{02} = 0.24m$, $C_1 = 0.1$, and $C_2 = 4.0$.

We normalized both the P_s and the envelop of P_{P1}, which are shown in Fig. 3.13(a). It is found that the waveforms are identical, i.e., the dual-cavity OFI can generate an amplitude-modulated (AM) sensing signal with P_{P1} as the carrier modulated by a P_s signal. This indicates that P_{P1} has the same sensing resolution (half laser wavelength) as the single-cavity OFI. We also found that a significantly larger sensing signal can be obtained using the dual-cavity OFI at P1 state. Fig. 3.13(b) shows the comparison of the two signals. The P-V value of the envelop of P_{P1} is 0.107 (a.u.), contrasted to 6.92×10^{-4} (a.u.) for P_s. The former is 155 times of the latter. It can be seen that the dual-cavity OFI in the new sensing scheme region leads to significant increase in the sensitivity sensing contrast to the single cavity OFI and it is able to provide an effective solution for the detection of very small or weak physical metrological quantities.

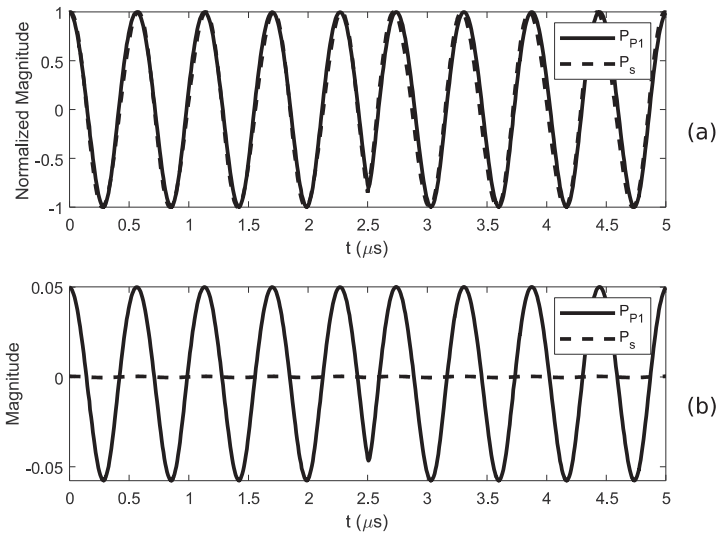

Fig. 3.13: Comparison of the laser intensity generated from dual-cavity OFI and single-cavity OFI. (a) Normalized P_s and envelop of P_{P1}. (b) Comparison of P_{P1} envelop and P_s

The larger the modulation depth (envelop), the more sensitive a P_{P1} for measurement. To measure the sensitivity, we define R as the enhancement ratio of P_{P1} envelop to P_s. We further tested the sensitivity within P1 state for different C_2 values, which are marked as A-E in Fig. 3.14.

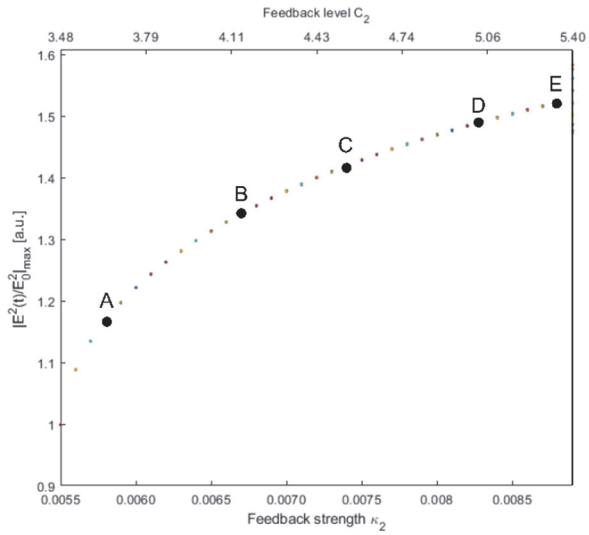

Fig. 3.14: Testing different C_2 in the new sensing scheme region.

Point A corresponds to when $C_2 = 3.73$, the P_{P1} is shown in Fig. 3.15. The P-V value of the envelop of P_{P1} is 0.186 (a.u.), this lead to an enhancement ratio 268. Point B corresponds to when $C_2 = 4.14$, the P_{P1} is shown in Fig. 3.16. The P-V of the envelop of P_{P1} is 0.089 (a.u.), this lead to an enhancement ratio 129. Point C corresponds to when $C_2 = 4.55$, the P_{P1} is shown in Fig. 3.17. The P-V of the envelop of P_{P1} is 0.064 (a.u.), this lead to an enhancement ratio 93. Point D corresponds to when $C_2 = 4.96$, the P_{P1} is shown in Fig. 3.18. The P-V of the envelop of P_{P1} is 0.053 (a.u.), this lead to an enhancement ratio 76. Point E corresponds to when $C_2 = 5.38$, the P_{P1} is shown in Fig. 3.19. The P-V of the envelop of P_{P1} is 0.044 (a.u.), this lead to an enhancement ratio 64. The results for the enhancement ratio are summarized in Table 3-1. It can be seen that, within P1, a smaller C_2 leads to a larger R.

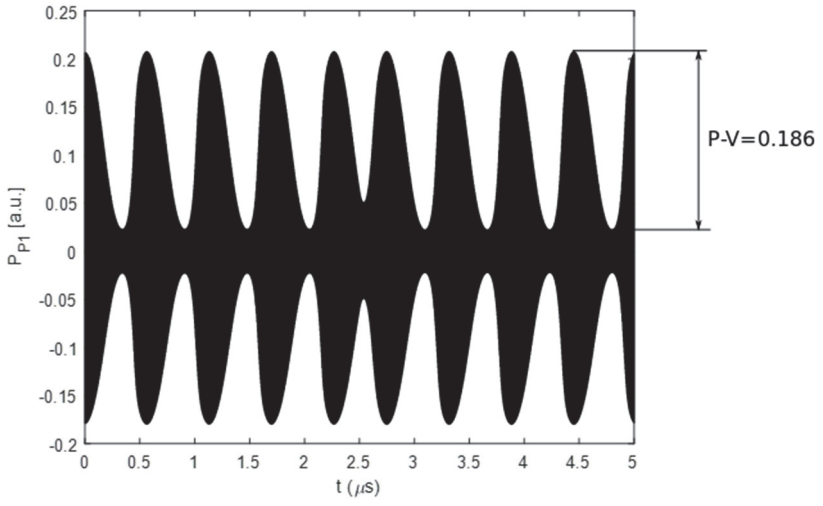

Fig. 3.15: P_{P1} at Point A with $C_2 = 3.73$.

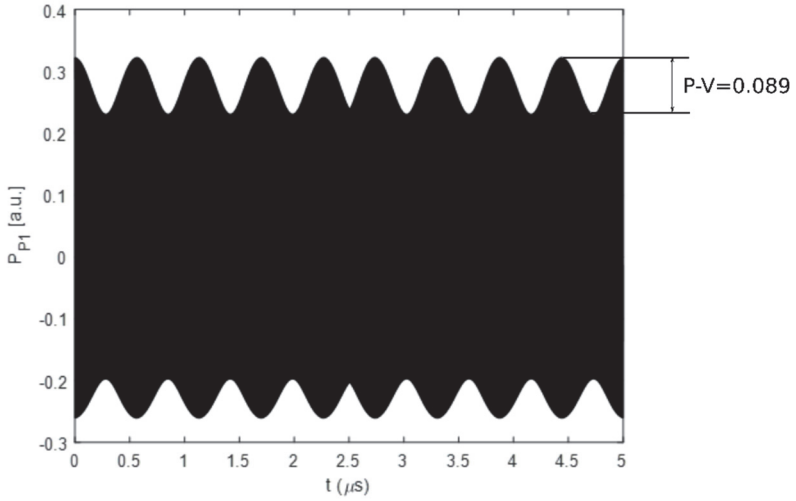

Fig. 3.16: P_{P1} at Point B with $C_2 = 4.14$.

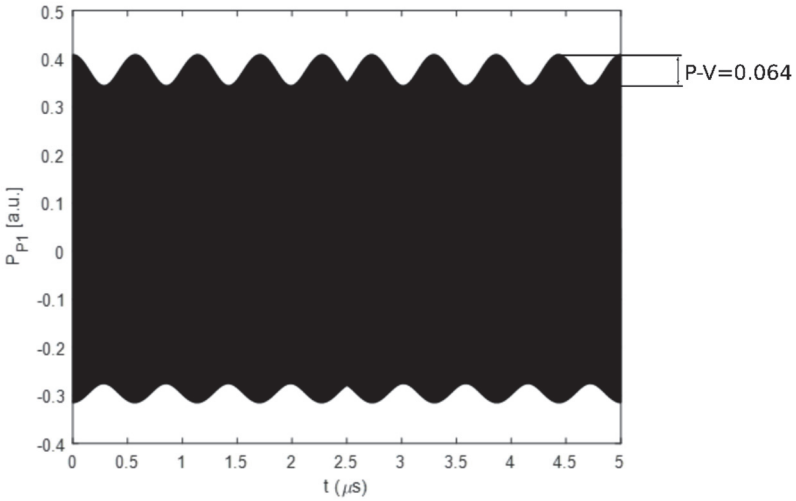

Fig. 3.17: P_{P1} at Point C with $C_2 = 4.55$.

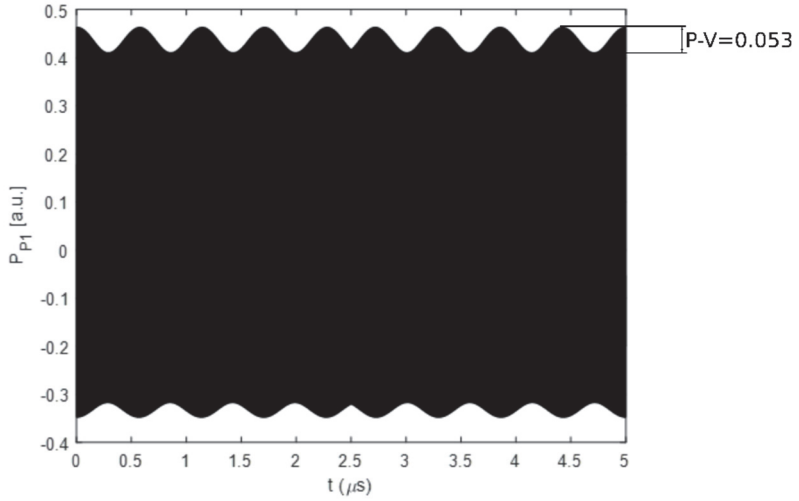

Fig. 3.18: P_{P1} at Point D with $C_2 = 4.96$.

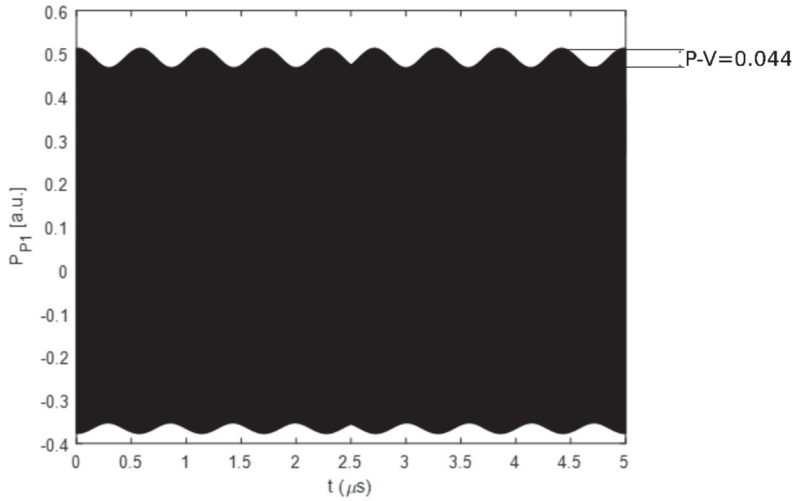

Fig. 3.19: P_{P1} at Point E with $C_2 = 5.38$.

Table 3-1: Sensitivity within P1 for different C_2 values

	A	**B**	**C**	**D**	**E**
C_2	3.73	4.14	4.55	4.96	5.38
P-V	0.186	0.089	0.064	0.053	0.044
R	268	129	93	76	64

Furthermore, we explored the influence of other controllable the system parameters such

as linewidth enhancement factor α, injection current density J and control cavity length L_{02}. We have the following fixed parameters $L_{01} = 0.10m$, $C_1 = 0.1$ and $C_2 = 5.38$. Table 3-2 tested different α values. In this simulation, we have $L_{02} = 0.24m$ and $J = 1.3J_{th}$. From the results, we can see smaller α can give a better enhancement. The values indicated as N/A means the system is no longer in the P1 state, therefore enhancement is not applicable. In Table 3-3, we shows the enhancement results under different J. In this simulation, we have $L_{02} = 0.24m$ and $\alpha = 3$. Lastly, we performed a set of simulation on different L_{02}. In this simulation, we set $J = 1.3J_{th}$ and $\alpha = 3$. From the results shown in Table 3-4, we found that the long cavity leads to a better enhancement.

Table 3-2: Sensitivity within P1 for different α values

α	2.0	2.5	3.0	3.5	4.0
P-V	N/A	0.0839	0.0446	0.0412	N/A
R	N/A	121	65	60	N/A

Table 3-3: Sensitivity within P1 for different J values

J/J_{th}	1.1	1.3	1.5	1.7	1.9
P-V	0.1499	0.0446	0.0691	N/A	N/A
R	217	65	100	N/A	N/A

Table 3-4: Sensitivity within P1 for different L_{02} values

L_{02}	0.14	0.18	0.22	0.26	0.30
P-V	0.0455	0.0545	0.064	0.0794	N/A
R	66	79	92	115	N/A

3.3.2. Experimental Investigation

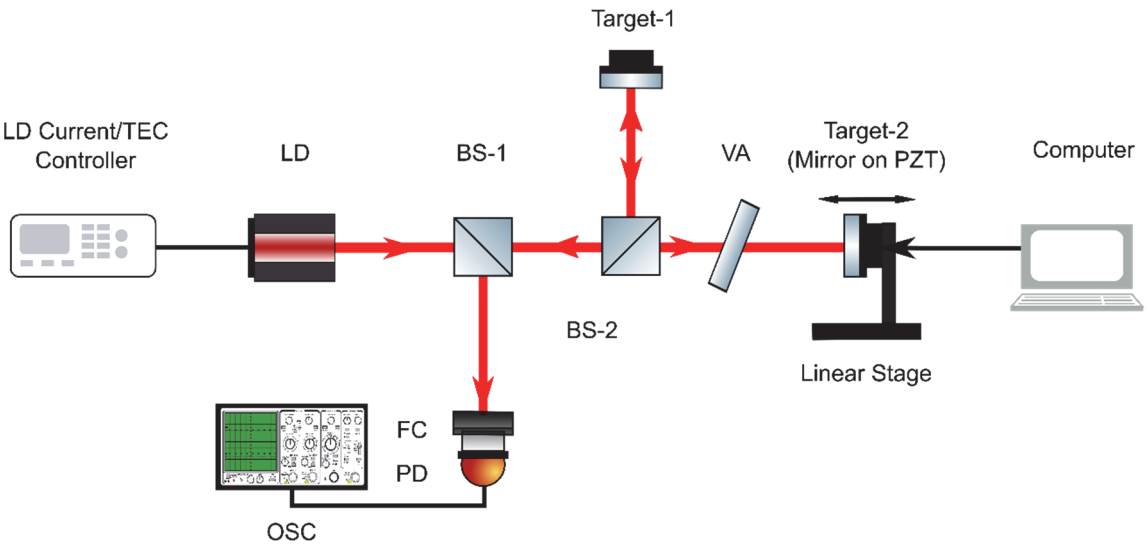

Fig. 3.20: Schematic layout of the experimental setup.

An experimental system shown in Fig. 3.20 is built to verify the proposed method. A single mode laser diode (Hatachi HL8325G, $\lambda = 830\ nm$, output power $P_0 = 40\ mW$) is employed in this physical system. The LD is driven and temperature-stabilized by an LD controller (Thorlabs, ITC4001) with the injection current of 75mA and the temperature of $23 \pm 0.002^{\circ}C$. The light emitted by the LD is focused by a lens and split into two light beams by a beam splitter (BS-1) with splitting ratio of 50:50. One beam is directed to the Target-2 with a mirror surface for providing high enough optical feedback to the LD. A variable attenuator (VA) is inserted inbetween the lens and Target-2 to adjust the feedback amount to ensure that the LD operates at P1 state. We also use it to adjust the modulation depth of P_{P1}. The other beam from BS-1 is directed to the Target-1 which is a piezoelectric transducer (PZT) (PI P-841.20) with a very weak reflective surface. Since the P_{P1} has a very high frequency, it needs a fast photodetector (PD) for its detection. Commonly, a commercial LD has an inbuilt PD which can be used for picking up P_s. However, the

bandwidth of the inbuilt PD is less than 1GHz, which cannot meet the requirement of our design. Therefore, in this experiment, we use an external PD with a bandwidth of 9.5 GHz (Thorlabs, PDA8GS). Therefore, a second beam spliter (BS-2) is needed to direct the part of light into this external PD. To make a direct experimental comparison, both P_s and P_{P1} signals are detected using the same PD, and they are then visualized by a fast oscilloscope (Tektronix DAS 70804).

One set of the recorded experimented waveforms are presented in Fig. 3.21. Fig. 3.21(a) is a voltage controlling signal applied on the PZT (Target-1) which drives Target-1 to move in a triangular waveform. The controlling voltage is provided by a signal generator with a frequency of 200Hz and amplitude of 0.85V. This makes Target-1 move with a displacement of 2500nm. Fig. 3.21(b) shows the corresponding P_s with only Target-1 in the experimental system. When recording P_s, the light to Target-2 must be blocked. It can be seen that the P_s is nearly buried in noise due to the surface with very weak reflectivity. The P-V value of P_s is about 1.0 mv. Fig. 3.21(c) shows the P_{P1} in dual-cavity OFI at P1 state. It can be seen that this signal is large and has a clear envelop. The P-V of the envelop is about 10 mV. Therefore, the enhancement ratio R is 10. Through adjust the VA, P_{P1} with lower feedback amount is obtained and shown in Fig. 3.21(d). The P-V of the envelop is about 50 mV, this gives the enhancement ratio $R = 50$.

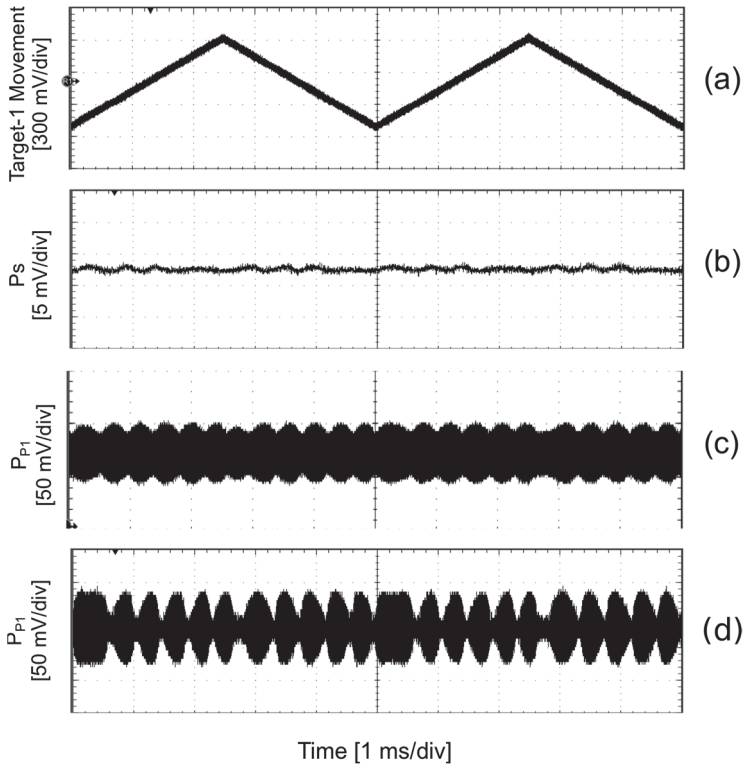

Fig. 3.21: Experimental results: (a) The triangular displacement waveform applied on Target-1. (b) Corresponding P_s. (c) Corresponding P_{P1}. (d) Corresponding P_{P1} with a lower feedback than (c).

3.4. A New Approach for Fringe Sub-Division

For a sensing signal generated by an OFI system, each fringe variation corresponds to a target displacement of $\lambda_0/2$, where λ_0 is the laser's wavelength. Therefore $\lambda_0/2$ is the basic resolution of all the OFI based applications. Over the years, researches have used different methods to improve the OFI system resolution. In 1998, Servagent *et al.* [136] used linear interpolation on the inter-fringe of a sawtooth-like OFI signal under moderate feedback regime to measure displacement. They found a linearity principle between a half-wavelength linear displacement and a sawtooth-like output optical power. By using linear interpolation on the output optical power, a resolution of $\lambda_0/12$ for displacement up to several micrometres can be achieved. In 2001, Wang et al proposed a method to

reconstruct displacement by sinusoidal phase modulation based OFI [137]. They modulated the phase of a OFI signal by changing the external cavity length. The generated OFI is processed by Fourier transform from which zero and first order of spectra components can be obtained and used for calculating the displacement of the target. Their experiment demonstrated the proposed method can achieve approximately $\lambda_0/50$ (31 nm) resolution. In the same year, their work in [103] uses signal processing by adding modulation of injection current into the OFI system to calculate the initial phase and retrieve displacement within a fringe, which achieves a resolution of $\lambda_0/90$ (16 nm) in experiment. In 2005, Guo et al. [138] proposed a sinusoidal phase modulating method to reconstruct harmonic displacement by adding an electro-optic modulator in between the laser and the external target. The modulator can provide a pure phase modulation in the optical length. By calculating the first and second order Fourier series of the modulated OFI signal, a wrapped phase of OFI signal can be obtained. Combining phase unwrapping, the displacement can be reconstructed based on the relationship between phase signal and the length of the external cavity. Although, this method gives resolution of $\lambda_0/80$, it requires the OFI system works in weak feedback regime. The most recent work in [139] utilizes experimental measurements to observe the relationship between optical frequency and LD terminal voltage versus external cavity length, they experimentally demonstrate a nanometric sensing system in P1 state, based on feedback interferometry in distributed interference lasers. With a high feedback strength to an LD can achieve a resolution up to $12nm$. The work in [140] proposed a spatial differential technique named as differential optical feedback interferometry. A reference laser is used improve the resolution up to $4nm$. The work in [141] improves the resolution by adding extra physical components, combines the high sensitivity of a frequency-shifted feedback

laser with the axial positioning capability of a confocal microscope, which realizes $2nm$ resolution in a non-ambiguous range of about ten microns. The use of dual-cavity OFI for displacement was reported in [111, 142, 143], they reached displacement resolution between 10 to 25 nm.

Our work in Section 3.3 confirmed the envelop of laser intensity in P1 state is same as the single-cavity OFI signal. With the dual-cavity OFI configuration, it significantly boosted the sensing sensitivity compare to the single-cavity OFI system. However, the resolution is still the same which is half-laser wavelength. In this section, we developed an algorithm that utilize the characteristic of the dual-cavity OFI signal in P1 state to realize a sub-nanometre scales displacement measurement.

3.4.1. Measurement Algorithm

An example of the dual-cavity OFI signal in P1 state (denoted as P_{P1}) is shown in Fig. 3.22. The envelop of the P_{P1} is the integer fringe numbered as M_i. The fractional fringes are the sub-fringes in the integer fringe, they are numbered as M_f. The algorithm of using P_{P1} for displacement measurement is presented in Fig. 3.23.

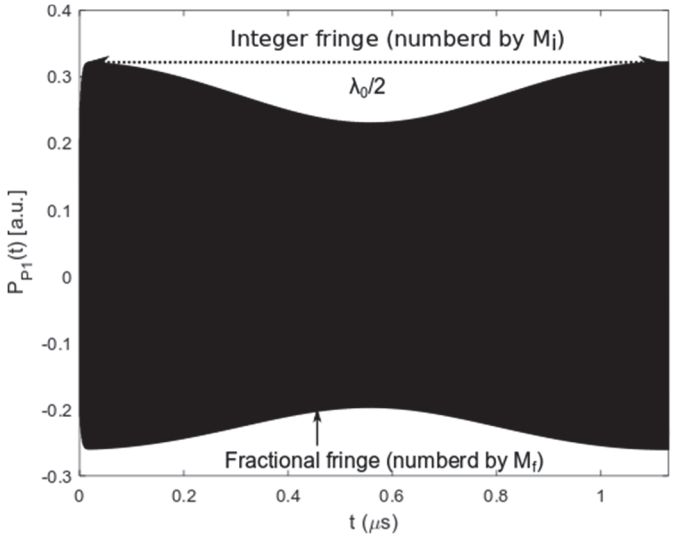

Fig. 3.22: An example of dual-cavity OFI signal in P1 state.

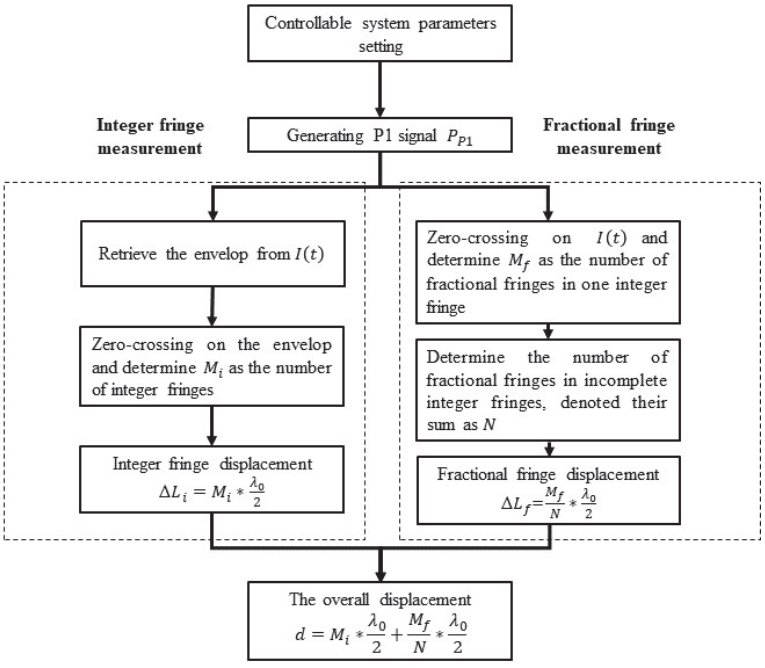

Fig. 3.23: Measurement procedures

The details of each step is described as below,

Step 1: Adjust the LD controllable parameters, such as injection current J, feedback strength κ, external cavity length L, and linewidth enhancement factor α, to ensure the dual-cavity OFI operates in P1 state.

Step 2: With an appropriate parameters settings, the laser intensity signal P_{P1} is generated and captured for analysis.

Step 3: The displacement measurement starts in this step. Two measurement process are performed simultaneous to realize both integer and fraction fringe measurement.

- Integer fringe measurement: performing the envelop extraction on P_{P1}, then determine the number of integer fringe, denoted as M_i. The displacement of the measurand target in the integer fringe measurement can be express as,

$$\Delta L_i = M_i * \frac{\lambda_0}{2} \tag{3.1}$$

- Fractional fringe measurement, determine the number of fractional fringe within one integer fringe, denoted as M_f. Then, determine the number of fractional fringe located before the first full integer fringe and after the last full integer fringe. Their sum is denoted as N. The displacement of the measurand target in the fractional fringe measurement can be express as,

$$\Delta L_f = \frac{N}{M_f} * \frac{\lambda_0}{2} \tag{3.2}$$

Step 4: With the displacement of both ΔL_i and ΔL_f are obtained. The total displacement of the measurand target can be expressed as,

$$\begin{aligned} d &= \Delta L_i + \Delta L_f \\ &= M_i * \frac{\lambda_0}{2} + \frac{M_f}{N} * \frac{\lambda_0}{2} \end{aligned} \tag{3.3}$$

3.4.2. Simulation

Following the algorithm described above, a set of simulation was performed to verify the

proposed algorithm.

1. We carefully selected the following parameters to ensure the dual-cavity OFI system operates in the P1 state. We set the $J = 1.3J_{th}$, where J_{th} the injection current density threshold. The measurand cavity length is $L_{01} = 0.10m$, the measurand target has a feedback strength $\kappa_1 = 0.0003$. It is set in a linearly movement shown as Fig. 3.24(a) with a displacement of $2.2\lambda_0$. The control cavity length is $L_{02} = 0.24m$. The second target has a feedback strength $\kappa_2 = 0.0065$. It is set in static. The LD has wavelength $\lambda_0 = 780nm$.

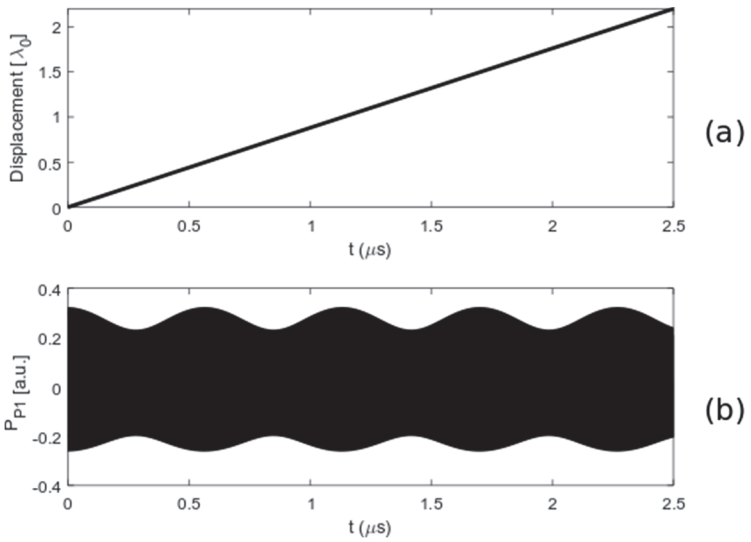

Fig. 3.24: Varying laser intensity in P1 state. (a) Displacement of the measurand target. (b) P_{P1} waveform.

2. Through solving the L-K equations, the laser intensity is represented as P_{P1}. shown in Fig. 3.24.
3. **Integer fringe measurement:** To count the number of the integer fringes, we extract the envelop from the P_{P1} shown in Fig. 3.25(a). Then apply the zero-crossing detection on the envelop, it will result a square waveform as shown in

Fig. 3.25(b). After that perform differentiation on the raising edge of the square waveform. The differentiated result is shown in Fig. 3.25(c), it gives us an impulse signal, from which we can determine $M_i = 3$ that is equivalent to $\Delta L_i = 1170$ nm .

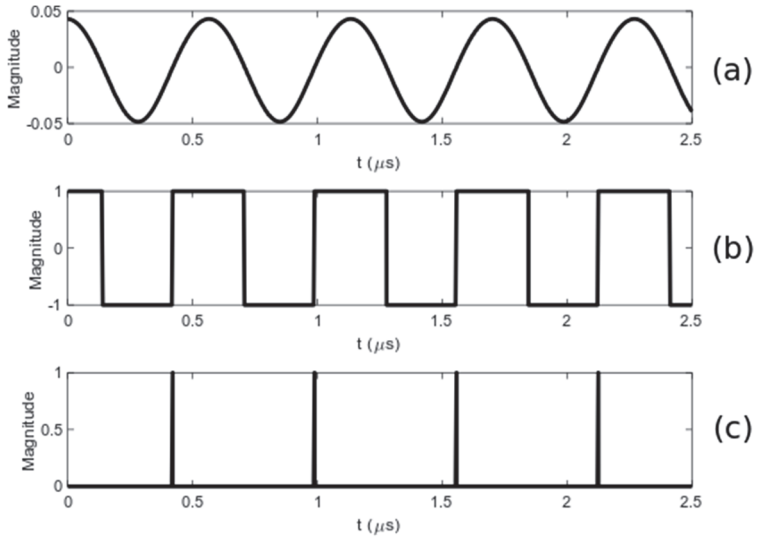

Fig. 3.25: Signal process applied P_{P1}. (a) The envelop of P_{P1}. (c) zero-crossing applied on the envelop. (c) Differentiation result on the envelop.

Fractional fringe measurement: We directly perform the zero-crossing on P_{P1} and find the number of fractional fringes in one integer fringe is $M_f = 113641$, which revealed the displacement resolution is about 0.003 nm. Then we counted, there are 83704 fractional fringes located before the first full integer fringe, another 75371 fractional fringes after the last full integer fringes, which gives $N = 159075$ and $\Delta L_f = 546$ nm . Fig. 3.26.(b) shows both integer and fractional fringes on the zero-crossing applied P1 signal.

4. The total displacement is 1716 nm, which is same as the displacement we set for measurand target, $2.2\lambda_0$.

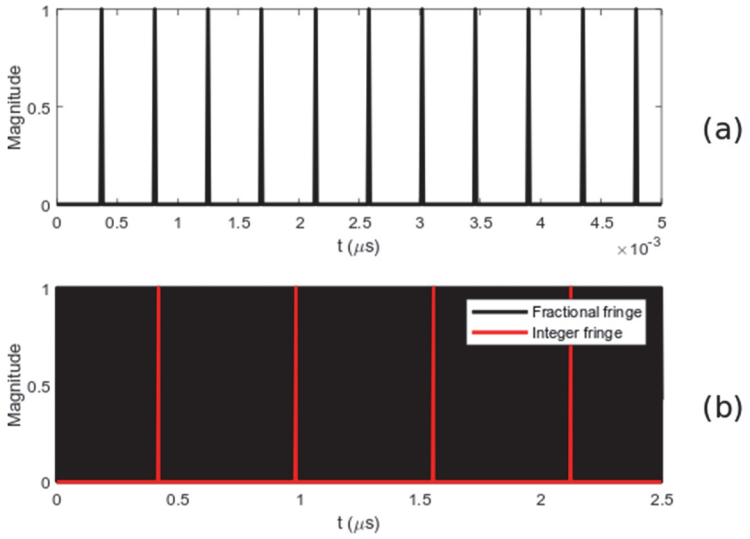

Fig. 3.26: The sub-division fringes. (a) Fractional fringes in P_{P1} at the first 0.005 us. (b) Integer fringes and fractional fringes.

3.4.3. Experiment

The proposed measurement algorithm was further verified by an experimental system shown in Fig. 3.27. A single mode LD (Hatachi HL8325G) is employed, the LD is driven and temperature-stabilized by an LD controller (Thorlabs, ITC4001). The light emitted by the LD is focused by a lens and split into two light beams by a beam splitter (BS-1) with splitting ratio of 50:50. One beam is directed to the Target-2 (Control Target) with a mirror surface for providing high enough optical feedback to the LD. A variable attenuator (VA) is inserted in between the lens and Target-2 to adjust the feedback amount to ensure that the LD operates at P1 state. The other beam from BS-1 is directed to the Target-1 (measurand target) which is a piezoelectric transducer (PZT) (PI P-841.20) with a weak reflective surface. Since the system exhibits a high frequency, it needs a fast photodetector (PD) for detection. The LD's the in-built PD is less than 1GHz, which cannot meet the requirement of our design. We use an external PD with a bandwidth of 9.5 GHz (Thorlabs, PDA8GS). Therefore, a second beam spliter (BS-2) is needed to direct

a part of light into this external PD. The detected LD intensity signals are visualized by a fast oscilloscope (Tektronix DAS 70804). The experiment is carried our according to the steps described in Fig. 3.23

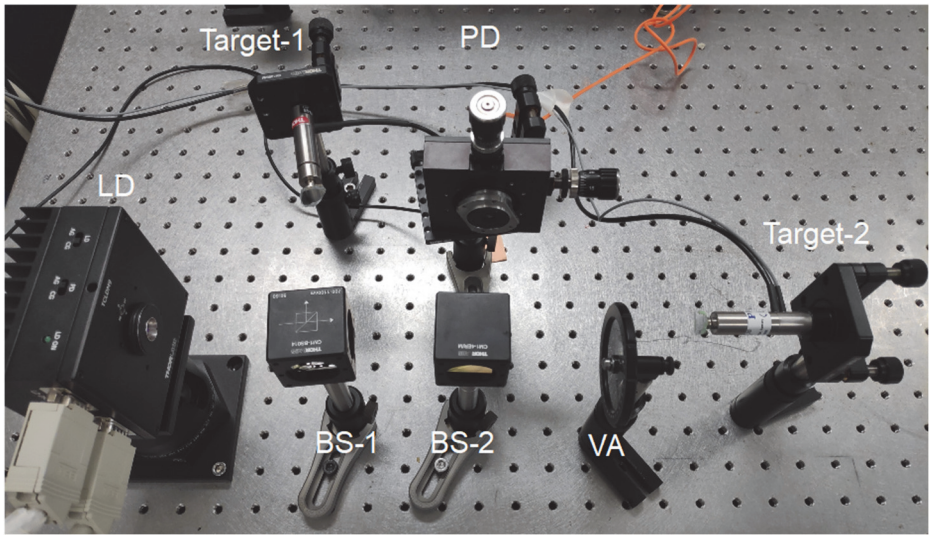

Fig. 3.27: Experiment setup

We set the measurand cavity length as $L_{01} = 0.13m$ and the control cavity about $L_{02} = 0.25m$ approximately. The LD has a wavelength of 830 nm, injection current 75mA , the α value of the LD is about 3.4, it was measured using the method in [76]. The measurand target is attached on a PZT, which is controlled by a PZT controller. A triangular voltage signal shown in Fig. 3.28(a) with amplitude 0.55V was applied on the PZT. Through adjust the VA to control the feedback amount in the control cavity, P_{P1} is generated and shown in Fig. 3.28(b).

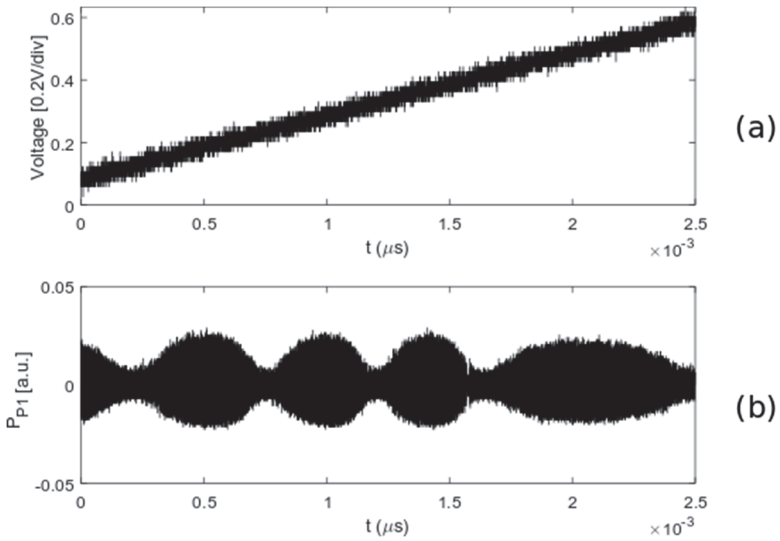

Fig. 3.28: Experimental results of varying laser intensity in P1 state. (a) Displacement of Target-1. (b) P_{P1} waveform.

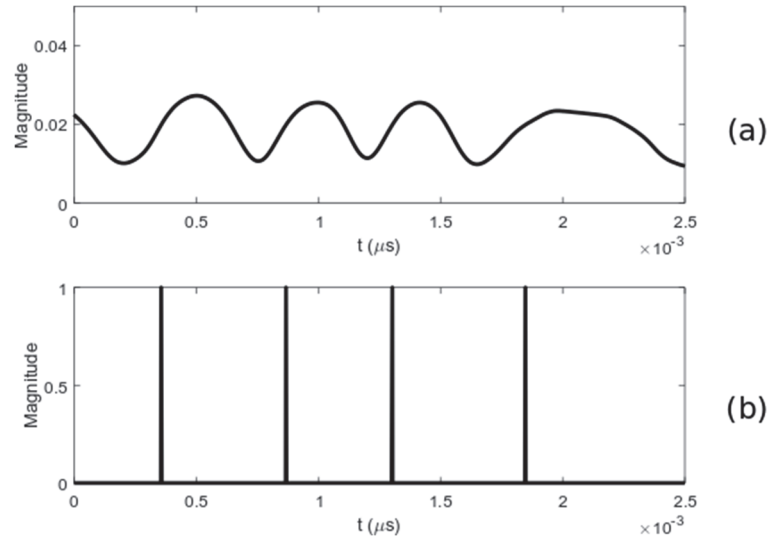

Fig. 3.29: Experimental results of signal process applied P_{P1}. (a) The envelop of P_{P1}. (b) Differentiation result on the envelop.

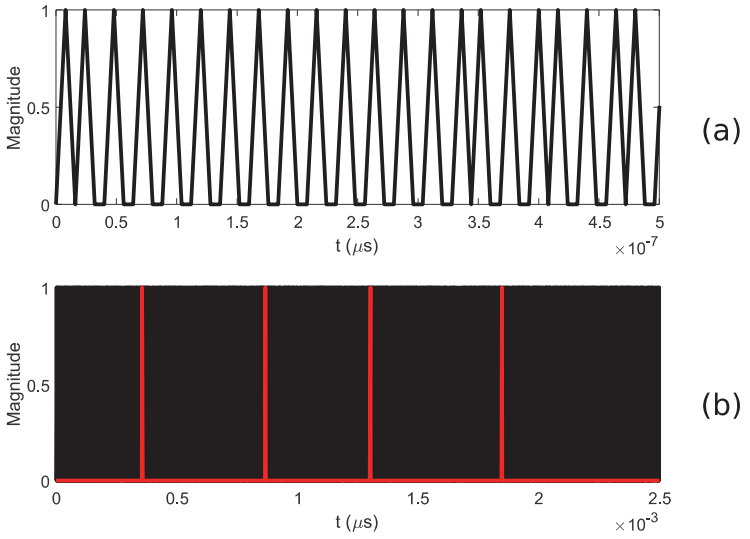

Fig. 3.30: Experimental results of sub-division fringes. (a) Fractional fringes in P_{P1} in the first 5×10^{-7} μs. (b) Integer fringes and fractional fringes.

The envelop of P_{P1} is extracted and shown in Fig. 3.29(a). After applied the zero-crossing detection, we can obtained $M_i = 3$, this can be seen in Fig. 3.29(b). Therefore, $\Delta L_i = 1245$ nm. Meanwhile, the zero-crossing is applied on the P_{P1} to obtain the fractional fringes. Fig. 3.30(a) shows the first $5*10^{-7}$ μs of the fractional fringes. Fig. 3.30(b) shows the both the integer and fractional fringes. There are 68055 fractional fringes in one integer fringe, indicating $M_f = 68055$, therefore the resolution is 0.006 nm. The total fractional fringes located before first full integer fringe and after the last full integer fringe is $N = 57484$, therefore, $\Delta L_f = 350.538$ nm.

3.5. Summary

In this chapter, we first reviewed the dynamic states of LD. When one of the system parameter values change, the LD can transition from steady state, P1, QP state and chaos. Then we presents theoretical analysis on OFI systems by investigating into the validity of

both L-K equations and the OFI model. Traditionally, existing OFI model was derived based on an assumption that the system operates in stable state. With the changes of the system parameters, e.g. feedback strength, LD injection current, the system will leave the steady state, entering other states and exhibits complicated dynamics. In this case, the OFI model will not be able to correctly describe the signal. In the validity study, we presented a bifurcation diagram that showing both dynamic states and optical feedback regimes Base on such bifurcation diagram, we further classified the operation of a LD into five regions.

- Region I: LD is in steady state and with weak feedback.
- Region II: LD is in steady state and with moderate feedback.
- Region III: LD is in P1 state and with moderate feedback.
- Region IV: LD is in P1 state and with strong feedback.
- Region V: LD is in qusi-periodic or chaos state and with strong feedback.

The above classification allows us to clearly identify how the states and regimes are corresponded. We performed three group of simulations in each of the five regions. The first two groups compared the waveforms generated using OFI model and L-K equations. The results show both models are only valid in Region I and Region II. When the optical feedback is high, the two models give very different waveforms. The third group simulation shows when a low-pass filter was applied on the waveforms that is obtained using L-K equations. The third simulation reflected a practical condition, where the observed waveforms under the high optical feedback may have been filtered due to the limited bandwidth of the internal PD. An experiment was conducted by observing the waveforms through the inbuilt PD and external PD. The results show a good aggrement with the thrid simulation. The study of the validity of OFI model and L-K equations

provide a guidance on applying appropriate models when designing OFI based sensing system.

In Section 3.3, we present a new sensing scheme that use of laser dynamics in dual-cavity OFI system to improve the sensing sensitivity. The second cavity is used to control the laser dynamics and ensure the LD operates at P1. The laser intensity in the P1 state exhibits an oscillation with its amplitude modulated by an OFI signal (generated with a single cavity and LD operating at steady state). It is observed that the modulation depth is remarkably larger than the magnitude of the OFI signal. By adjusting the feedback strength, the system can be set at a most optimal working point for sensing and measurement and it does not have the requirement of an accurate adjustment of control cavity length. The results show the sensitivity can be improved up to 268 time in theory and 50 time improvement in the experiment. The work in this section has contributed a journal publication [144]. In Section 3.4, a new approach for fringe sub-division using the characteristic of the dual-cavity OFI signal in P1 state was proposed. It utilized the high frequency in the laser intensity signal and through signal processing technique in the time-domain to achieve a sub-nanometre scale displacement sensing. Our simulation results show the displacement resolution can reach up to 0.003 nm for a LD with 780nm wavelength. The experimental results show the system can reach 0.006 nm for an LD with 830nm wavelength. It is expected the resolution could be further increased if a higher frequency laser intensity signal is generated in the dual-cavity OFI system. The work in both Section 3.3 and Section 3.4 utilize the properties of the dual-cavity OFI signal in P1 state to realize a significant sensing performance improvement. They provide an effective solution for the detection of very small or weak physical quantities.

Chapter 4. A New Method for Measuring Linewidth Enhancement Factor

The LDs are the most abundant lasers, due to their small size, large gain per unit length, wide gain spectrum and emission wavelength flexibility. It plays a key role in the emerging field of optoelectronics, such as optical sensor, optical communication and optical disc system, etc. However, the conventional semiconductor lasers cannot achieve fundamental spectral purity similar to gas and solid-state lasers due to intrinsic linewidth broadening stemming from significant coupling between the real and imaginary parts of the susceptibility [145]. In 1982, Henry described this coupling by a ratio of their derivatives with respect to the carrier density, this ratio is commonly referred as the linewidth enhancement factor (also called α factor). It is defined as $\alpha = (\partial n_R / \partial N) / (\partial n_I / \partial N)$, where N, n_R and n_I are, respectively, the carrier density, the real and imagery part of the refractive index [146]. The α factor is regarded as a fundamental descriptive parameter of the LD, not only for its crucial role in spectral characteristics, but also for its dynamical response to the optical injection and feedback. As demonstrated in Chapter 2 and Chapter 3, α factor could impact the sensing sensitivity and system operating state in the dual-cavity OFI system. Therefore, an accurate value of the α factor is vital for behaviour analysis of an LD and designing its application systems. In this chapter, a new method for measuring α is presented by using laser relaxation oscillation.

Various techniques have been explored for measuring the α factor. These techniques can be mainly classified [147, 148] as follow:

1. Direct linewidth measurement. In this technique, it was further divided into another three categories, (1). Linewidth above and below threshold. The α factor was derivate from the ratio between the laser linewidth value below threshold and the value above threshold. $\alpha = 5.0 \pm 0.4$ was reported in [149] for using this method. (2). Linewidth above threshold. The α factor can be directly computed from the linewidth above threshold formula, under the assumption that all other laser parameters are known. Based on this method α ranging between 3.5 and 5 are reported in [150-152]. (3). Linewidth below threshold was first proposed in [153], it employs the changes in linewidth versus centre frequency shift measured at below threshold. $\alpha = 5.0 \pm 0.4$ was reported for using this method.

2. Current modulation. It is based on modulation of the bias current utilise the fact that, due to $\alpha \neq 0$, amplitude modulation (AM) is accompanied by frequency modulation (FM). E.g. Chattopadhyay et al. [154] proposed a method of measuring α factor through narrowband optical FM generation in direct modulation of a Fabry–Perot laser diode, where the modulating signal is fed through a thermoelectric current and temperature controller. The α factor is estimated by detecting the sinusoidal modulated light wave in a photodiode and measuring the amplitude of the detected sinusoidal signal. It is found the α factor decreases linearly with the increase in bias current of the laser diode above threshold.

3. Optical injection locking. In [155], it introduced a method which utilises the behaviour of a distributed feedback laser diode at very weak levels of optical injection, where the locking range is symmetrical with respect to the master-slave frequency detuning. The α factor is deduced from the measurement of the maximum and minimum voltage excursions in the symmetrical locking range. In [156], a slightly different scheme was proposed. The α factor is calculated through the measurement of the maximum and minimum power excursion. However both schemes were criticised for unreliability due to the interference of the uncoupled light from the master laser or high current level caused noised. Other injection locking based method such as [74] measures α factor using Hopf bifurcation. α values around 4.4 ± 0.9 and 3.2 ± 0.3 were reported. In [157] frequency-modulated optical injection was use to prove the method can measure small α value and gives $\alpha = 0.28 \pm 0.04$.

4. Optical feedback interferometry (OFI) technique. The OFI technique is based on the optical feedback effect that occurs when a small fraction of light emitted by the SL reflected by the moving target re-enters the SL cavity, leading to both modulated amplitude and frequency of the LD power. The modulated LD optical power is known as the optical feedback signal which carries the information associated with the LDs' parameters [80, 81].

Among all these techniques, OFI technique is an emerging and promising method reflecting a minimum part-count scheme, which provides an ease of implementation and simplicity in system configuration. Various methods have been presented for the

measurement of α factor. In 2004, Yu et al. [76] proposed a method to measure α factor by using the hysteresis of OFI signal when the external target has a reciprocating movement. However, this method needs the OFI system being in moderate feedback regime and OFI signals have zero-crossing points, i.e. the optical feedback level in the range of 1<C<3. The required condition on the feedback level may not be met in some practical applications. Although an attenuator can be used to adjust the optical feedback to the measurement range with 1<C<3, this may lead to a larger measurement error as α factor is influenced by optical feedback level [79]. Then several other OFI-based methods were developed [49, 77-79, 158] for covering different C level, e.g. the methods in [77, 158] are for 0<C<1 and methods in [78, 79] for 1<C<4.6. The method in [80], investigated the relationship between the light phase and power from the L-K equations, it was found that the α can be simply measured from the power value overlapped by two LDs' output power under two different optical feedback levels. The simulations show, α value ranging from 0.1 to 8.0 can be obtained, with errors between 3.8% to 7.8%. These methods for retrieving α are based on commonly accepted OFI waveform model followed by data processing applied on the waveform, e.g. phase unwrapping in [49, 79], and data-to-model fitting algorithms in [77, 78, 158]. However, the reported hysteresis and it resulted sawtooth-like OFI waveform is on the case with $\alpha > 1$ [79, 99, 159]. For $\alpha < 1$, the hysteresis in an OFI waveform does not follow the switching law reported in [99, 159]. Thus, the existing algorithms developed for α will be not applicable.

4.1. Measurement Theory

Recently, high sensing sensitivity by using the relaxation oscillation (RO) frequency has been demonstrated [96, 135, 160, 161]. This gives us an inspiration to measure α factor

by laser dynamics. The RO frequency (denoted as f_{RO}) of the LD can be obtained by linear stability analysis for the system described by L-K equations. With the conditions of $\kappa\tau / \tau_{in} \ll 1$, an expression for f_{RO} can be derived from L-K equations given as below [133],

$$f_{RO} = \frac{1}{2\pi}\sqrt{\frac{J-1}{\tau_s \tau_p}\left(1+G_N N_0 \tau_p\right)}\sqrt{\frac{\left[1-2\frac{\kappa}{\tau_{in}}\tau_p\cos\left(\omega_s\tau\right)\right]\left[1+\frac{\kappa}{\tau_{in}}\tau\cos\left(\omega_s\tau\right)-\alpha\frac{\kappa}{\tau_{in}}\tau\sin\left(\omega_s\tau\right)\right]}{1+(\frac{\kappa}{\tau_{in}})^2\tau^2+2\frac{\kappa}{\tau_{in}}\tau\cos\left(\omega_s\tau\right)}} \quad (4.1)$$

Where $\frac{1}{2\pi}\sqrt{\frac{J-1}{\tau_s \tau_p}\left(1+G_N N_0 \tau_p\right)}$ is the RO frequency of a solitary LD (denoted by $f_{RO-zero}$). ω_s is the laser angular frequency in the steady state. It can be seen the RO frequency is determined by both LD associated parameters G_N, N_0, τ_s, τ_p, α and its operation related parameters J, κ, τ. In following, we derive the measurement formula of α. First, we re-arrange the Eq.(4.1) as following,

$$\left(\frac{f_{RO}}{f_{RO-zero}}\right)^2 = \frac{[1-2\frac{\kappa}{\tau_{in}}\tau_p\cos(\omega_s\tau)][1+\frac{\kappa}{\tau_{in}}\tau\cos(\omega_s\tau)-\alpha\frac{\kappa}{\tau_{in}}\tau\sin(\omega_s\tau)]}{1+(\frac{\kappa}{\tau_{in}})^2\tau^2+2\frac{\kappa}{\tau_{in}}\tau\cos(\omega_s\tau)} \quad (4.2)$$

Limiting our treatment to practical case $\kappa < 0.01$, Eq.(4.2) can be approximated as following,

$$\left(\frac{f_{RO}}{f_{RO-zero}}\right)^2 = \frac{1+\frac{\kappa}{\tau_{in}}\tau\sqrt{1+\alpha^2}\cos(\omega_s\tau+\arctan\alpha)}{[1+(\frac{\kappa}{\tau_{in}})^2\tau^2+2\frac{\kappa}{\tau_{in}}\tau\cos(\omega_s\tau)][1+2\frac{\kappa}{\tau_{in}}\tau_p\cos(\omega_s\tau)]} \quad (4.3)$$

Neglecting second-order contribution, Eq.(4.3) becomes,

$$\left(\frac{f_{RO}}{f_{RO-zero}}\right)^2 = \frac{1+\frac{\kappa}{\tau_{in}}\tau\sqrt{1+\alpha^2}\cos(\omega_s\tau+\arctan\alpha)}{1+2\frac{\kappa}{\tau_{in}}[\tau_p\cos(\omega_s\tau)+\tau\cos(\omega_s\tau)]} \tag{4.4}$$

Because $\tau_p << \tau$, Eq.(4.4) can be simplified and re-arrange as,

$$\left(\frac{f_{RO}}{f_{RO-zero}}\right)^2 = \frac{1+\frac{\kappa}{\tau_{in}}\tau\sqrt{1+\alpha^2}\cos(\omega_s\tau+\arctan\alpha)}{1+2\frac{\kappa}{\tau_{in}}\tau\cos(\omega_s\tau)} \tag{4.5}$$

For the case $\kappa < 0.01$, Eq.(4.5) can be approximated as following:

$$\left(\frac{f_{RO}}{f_{RO-zero}}\right)^2 = [1+\frac{\kappa}{\tau_{in}}\tau\sqrt{1+\alpha^2}\cos(\omega_s\tau+\arctan\alpha)][1-2\frac{\kappa}{\tau_{in}}\tau\cos(\omega_s\tau)] \tag{4.6}$$

Neglecting second-order contribution, Eq.(4.6) becomes,

$$\left(\frac{f_{RO}}{f_{RO-zero}}\right)^2 = 1+\frac{\kappa}{\tau_{in}}\tau[\sqrt{1+\alpha^2}\cos(\omega_s\tau+\arctan\alpha)-2\cos(\omega_s\tau)] \tag{4.7}$$

Re-arranging Eq.(4.7), we get,

$$\left(\frac{f_{RO}}{f_{RO-zero}}\right)^2 = 1-\frac{\kappa}{\tau_{in}}\tau(\cos\omega_s\tau+\alpha\sin\omega_s\tau) \tag{4.8}$$

By setting up $\cos(\omega_s\tau)=0,\pm1$ and $\sin(\omega_s\tau)=0,\pm1$ in Eq.(4.8), the following four cases can be obtained,

Case 1: with $\cos(\omega_s\tau)=0$, $\sin(\omega_s\tau)=1$, from Eq.(4.8), we have,

$$\left(\frac{f_{RO1}}{f_{RO-zero}}\right)^2 = 1-\alpha\frac{\kappa\tau}{\tau_{in}} \tag{4.9}$$

Case 2: with $\cos(\omega_s\tau)=0, \sin(\omega_s\tau)=-1$, from Eq.(4.8), we have

$$\left(\frac{f_{RO2}}{f_{RO-zero}}\right)^2 = 1+\alpha\frac{\kappa\tau}{\tau_{in}} \tag{4.10}$$

Case 3: with $\cos(\omega_s\tau)=1,\ \sin(\omega_s\tau)=0$, we have

$$\left(\frac{f_{RO3}}{f_{RO-zero}}\right)^2 = 1-\frac{\kappa\tau}{\tau_{in}} \tag{4.11}$$

Case 4: with $\cos(\omega_s\tau)=-1,\ \sin(\omega_s\tau)=0$, we have

$$\left(\frac{f_{RO4}}{f_{RO-zero}}\right)^2 = 1+\frac{\kappa\tau}{\tau_{in}} \tag{4.12}$$

In the following we presented three methods to calculate α value.

4.1.1. Method 1

Firstly, let's set $\Delta f_{ROi} = f_{ROi} - f_{RO-zero}$ then Eq. (4.9)-(4.12) can be re-written as,

$$\Delta f_{RO1} = f_{RO\text{-}zero}\left(\sqrt{1\text{-}\alpha\frac{\kappa\tau}{\tau_{in}}}\text{-}1\right) \tag{4.13}$$

$$\Delta f_{RO2} = f_{RO\text{-}zero}\left(\sqrt{1+\alpha\frac{\kappa\tau}{\tau_{in}}}\text{-}1\right) \tag{4.14}$$

$$\Delta f_{RO3} = f_{RO\text{-}zero}\left(\sqrt{1\text{-}\frac{\kappa\tau}{\tau_{in}}}\text{-}1\right) \tag{4.15}$$

$$\Delta f_{RO4} = f_{RO\text{-}zero}\left(\sqrt{1+\frac{\kappa\tau}{\tau_{in}}}\text{-}1\right) \tag{4.16}$$

From Eq.(4.13)-(4.16), we can get,

$$\Delta f_{RO1} - \Delta f_{RO2} = f_{RO\text{-}zero}\left(\sqrt{1-\alpha\frac{\kappa\tau}{\tau_{in}}} - \sqrt{1+\alpha\frac{\kappa\tau}{\tau_{in}}}\right) \tag{4.17}$$

$$\Delta f_{RO1} - \Delta f_{RO3} = f_{RO\text{-}zero}\left(\sqrt{1-\alpha\frac{\kappa\tau}{\tau_{in}}} - \sqrt{1-\frac{\kappa\tau}{\tau_{in}}}\right) \tag{4.18}$$

$$\Delta f_{RO3} - \Delta f_{RO4} = f_{RO\text{-}zero}\left(\sqrt{1-\frac{\kappa\tau}{\tau_{in}}} - \sqrt{1+\frac{\kappa\tau}{\tau_{in}}}\right) \tag{4.19}$$

From Eq.(4.17)-(4.19), we can obtain,

$$(\Delta f_{RO1} - \Delta f_{RO2})\left(\sqrt{1-\frac{\kappa\tau}{\tau_{in}}} - \sqrt{1+\frac{\kappa\tau}{\tau_{in}}}\right) = (\Delta f_{RO3} - \Delta f_{RO4})\left(\sqrt{1-\alpha\frac{\kappa\tau}{\tau_{in}}} - \sqrt{1+\alpha\frac{\kappa\tau}{\tau_{in}}}\right) \tag{4.20}$$

$$(\Delta f_{RO1} - \Delta f_{RO3})\left(\sqrt{1-\frac{\kappa\tau}{\tau_{in}}} - \sqrt{1+\frac{\kappa\tau}{\tau_{in}}}\right) = (\Delta f_{RO3} - \Delta f_{RO4})\left(\sqrt{1-\alpha\frac{\kappa\tau}{\tau_{in}}} - \sqrt{1-\frac{\kappa\tau}{\tau_{in}}}\right) \tag{4.21}$$

By solving Eq.(4.20) and Eq.(4.21) simultaneously, α can be obtained. In this method, it is required to know the value of $f_{RO\text{-}zero}, f_{RO1}, f_{RO2}, f_{RO3}, f_{RO4}$.

4.1.2. Method 2

For simplicity, we set $M_i = \left(\frac{f_{ROi}}{f_{RO-zero}}\right)^2$, so Eq.(4.9) to Eq.(4.12) can be re-written as following,

$$M_1 = 1 - \alpha\frac{\kappa\tau}{\tau_{in}} \tag{4.22}$$

$$M_2 = 1 + \alpha\frac{\kappa\tau}{\tau_{in}} \tag{4.23}$$

$$M_3 = 1 - \frac{\kappa\tau}{\tau_{in}} \tag{4.24}$$

$$M_4 = 1 + \frac{\kappa\tau}{\tau_{in}} \tag{4.25}$$

Using Eq.(4.24) and Eq.(4.25), $\frac{\kappa\tau}{\tau_{in}}$ can be expressed as,

$$\frac{\kappa\tau}{\tau_{in}} = \frac{M_4 - M_3}{M_3 + M_4} \tag{4.26}$$

Using Eq.(4.22) to divide Eq.(4.24), we get

$$\frac{M_1}{M_3} = \frac{1-\alpha x}{1-x} \tag{4.27}$$

And α can be expressed as,

$$\alpha = \frac{M_4 + M_3 - 2M_1}{M_4 - M_3} \tag{4.28}$$

In this method, it is required to know $f_{RO\text{-}zero}$, f_{RO1}, f_{RO3}, f_{RO4}.

4.1.3. Method 3

For this method we only using Case 1 Eq.(4.9) and Case 3 Eq.(4.11). They can be re-arranged as following,

$$1 - \left(\frac{f_{RO1}}{f_{RO-zero}} \right)^2 = \alpha \frac{\kappa\tau}{\tau_{in}} \tag{4.29}$$

$$1 - \left(\frac{f_{RO3}}{f_{RO-zero}} \right)^2 = \frac{\kappa\tau}{\tau_{in}} \tag{4.30}$$

Keeping the LD under same optical feedback κ, Eq.(4.29) and Eq.(4.30) describe a linear relationship between the relative RO frequency difference and the external cavity length L respectively for the two cases. Denoting the gradients of the two lines as S_1 and S_2, α

can be calculated by their ratio shown as below,

$$\alpha=\frac{S_1}{S_2} \tag{4.31}$$

In this method, it only requires to know $f_{RO\text{-}zero}$, f_{RO1}, f_{RO3}.

4.2. Simulation Test

In this section we verify the three proposed methods by simulations. We need to obtain $f_{RO\text{-}zero}$ and the RO frequencies respectively at the four cases. All the RO related frequencies can be gained from the transient oscillation waveform of laser intensity through solving L-K equations. The simulations are divided into two parts, the first simulation is used for method 1 and method 2. This is because the RO frequency can be obtained in one location for these two methods. The second simulation is used for method 3 only, it requires RO frequency obtain at different locations. A comparison table will be presented in this section to compare the performance of each method. In both simulations, the settings for system parameters are initial external cavity length $L_0=0.16m$, the injection current ratio is $J=1.5J_{th}$, feedback strength κ=0.00003, $\alpha=3$ and LD wavelength is $\lambda_0=780nm$.

The procedures of the simulation test for method 1 and 2 are summarized as below:

1. Set the target in a linearly movement shown in Fig. 4.1(a) with a displacement of $0.8\lambda_0$. Correspondingly, we can use the OFI model Eq.(1.15) and Eq.(1.21) to plot an OFI signal shown in Fig. 4.1(b), and Fig. 4.1(c) on which we can locate the accurate locations for Case 1 to Case 4.

2. Set the external cavity to the location of the four cases, the external cavity length can be expressed as $L = L_0 + L_{Case\_n}$, where L_{Case_n} is the target's location in each case. Then generates the corresponding laser intensity $I(t)$ by numerically solving the L-K equations. Fig. 4.2 shows the laser transient waveform for Case 1. From which, the corresponding RO frequencies can be obtained.

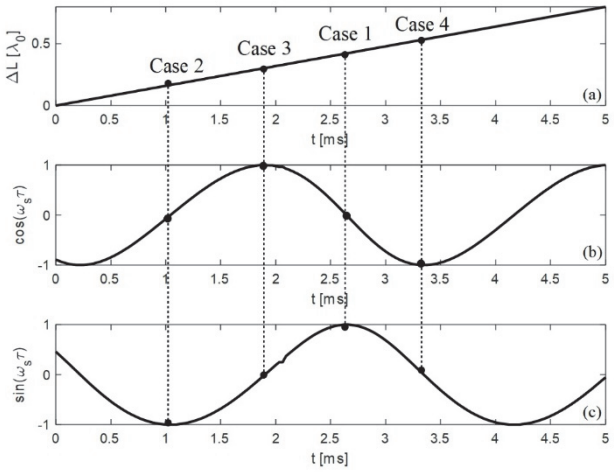

Fig. 4.1: OFI signal $L_0 = 0.16m$, κ=0.00003 , $J = 1.5J_{th}$ and $\alpha = 3$. (a): Target displacement. (b): $\cos(\omega_s \tau)$ waveform. (c): $\sin(\omega_s \tau)$ waveform.

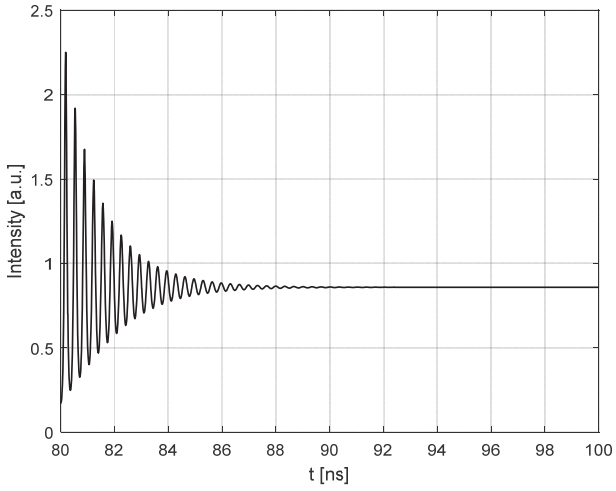

Fig. 4.2: Transient waveform of the laser intensity at Case 1 with $L_0 = 0.16m$.

The procedures of the simulation test for method 3 is summarized as below:

1. Starting from $L_0 = 0.16m$, increase the cavity length and set it with 6 different locations.
2. Similar to Step 2 in the simulation for method 1 and 2. At each location, apply a linearly movement on the target shown in Fig. 4.1(a), with a displacement of $0.8\lambda_0$. Correspondingly, use the OFI model to plot an OFI signal on which we can locate the accurate locations for Case 1 and Case 2.
3. Set the external cavity to the location of Case 1 and Case 2, the corresponding laser intensity $I(t)$ can be generated through numerically solving the L-K equations.
4. Repeat Step 2 and 3 for the 6 different locations, we get six RO frequencies for each case, denoted by f_{RO1_i} and f_{RO2_i}, i=1,2,..6. The relationship between the relative RO frequency ($(f_{ROi} - f_{RO-zero}) / f_{RO-zero}$) and the cavity length L for the two cases are shown in Fig. 4.3. Note that the gradient can be determined by only 2 points. In order to reduce the measured error, we prefer to use more than 2 points, e.g. 6 points to do line fitting to get the gradients at each case. From the gradients of these two fitting lines, α can be calculated by using Eq.(4.31).

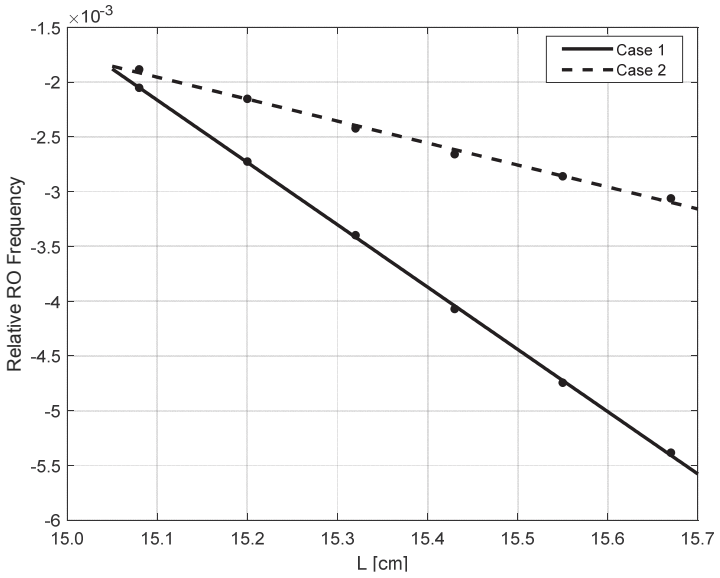

Fig. 4.3: Relationship between the relative RO frequency and the external cavity length L.

Under the same system settings, we change the pre-set value of α from 0.5 to 5 and measure them using the three methods. The relative error is used to measure the performance of each method, that is calculated by $|\alpha-\hat{\alpha}|/\alpha$, where α is the pre-set true value and $\hat{\alpha}$ is calculated using the proposed methods. Table 4-1 to Table 4-6 show the simulation results. In each table, it lists the RO frequencies under each case, the measured α value and the error in percentage. The results show that method 1 tends to perform well when the α value is small, the average error in method 1 for measuring α value between 0.5 to 2 is about 3.50%. Method 2 and 3 tend to perform well for LD with larger α value. The average error in method 2 for measuring α value between 3 to 5 is about 1.68% and the average error in method 3 is about 0.86%. The overall error for method 1 is 3.22%, method 2 is 4.25% and method 3 is 3.85%. This results can be compared to the method presented in [80], the error for α value range 0.5~6 is between 5.1% to 7.1%. Therefore, our methods show a satisfactory and reliable results.

Table 4-1: Simulation results for testing the three methods when $\alpha = 0.5$.

$f_{RO\text{-}zero} = 2.9664, f_{RO1} = 2.9640, f_{RO2} = 2.9688, f_{RO3} = 2.9619, f_{RO4} = 2.9712$		
	Measured α	Error
Method 1	0.5176	3.52%
Method 2	0.5489	9.78%
Method 3	0.5203	3.80%

Table 4-2: Simulation results for testing the three methods when $\alpha = 1.0$.

$f_{RO\text{-}zero} = 2.9664, f_{RO1} = 2.6160, f_{RO2} = 2.9712, f_{RO3} = 2.9619, f_{RO4} = 2.9712$		
	Measured α	Error
Method 1	1.0324	3.24%
Method 2	1.0644	6.44%
Method 3	1.0109	0.60%

Table 4-3: Simulation results for testing the three methods when $\alpha = 2.0$.

$f_{RO\text{-}zero} = 2.9664, f_{RO1} = 2.9570, f_{RO2} = 2.9761, f_{RO3} = 2.9620, f_{RO4} = 2.9712$		
	Measured α	Error
Method 1	2.0759	3.79%
Method 2	2.0844	4.22%
Method 3	2.0400	1.90%

Table 4-4: Simulation results for testing the three methods when $\alpha = 3.0$.

$f_{RO\text{-}zero} = 2.9664, f_{RO1} = 2.9528, f_{RO2} = 2.9811, f_{RO3} = 2.9619, f_{RO4} = 2.9710$		
	Measured α	Error
Method 1	3.1012	3.37%
Method 2	2.9939	0.20%
Method 3	2.9400	1.90%

Table 4-5: Simulation results for testing the three methods when $\alpha = 4.0$.

$f_{RO\text{-}zero} = 2.9664, f_{RO1} = 2.9487, f_{RO2} = 2.9861, f_{RO3} = 2.9620, f_{RO4} = 2.9710$		
	Measured α	Error
Method 1	4.1352	3.38%
Method 2	3.9444	1.39%
Method 3	3.8100	4.80%

Table 4-6: Simulation results for testing the three methods when $\alpha = 5.0$.

$f_{RO\text{-}zero} = 2.9664, f_{RO1} = 2.945, f_{RO2} = 2.991, f_{RO3} = 2.962, f_{RO4} = 2.971$		
	Measured α	Error
Method 1	5.0996	1.99%
Method 2	4.8274	3.45%
Method 3	4.7500	5.00%

4.3. Experimental Verification

To verify the proposed method, we further built an experimental system as depicted in Fig. 4.4. The LD in the experiment is a single mode laser diode (Sanyo, DL4140-001S) with a wavelength of 780nm and maximum output power of 25 mW, the LD is driven and temperature-stabilized by a LD controller (Thorlabs, ITC4001) at an injection current of 35mA and the temperature of $23 \pm 0.002^{\circ}\mathrm{C}$. The light emitted by the LD is focused by a lens and then touch the piezoelectric transducer (PZT) (Thorlabs, PAS005). An attenuator is used to adjust the optical feedback strength. The PZT with a displacement resolution of 20nm, driven by a PZT controller (Thorlabs, MDT694), is used to continuously adjust the external optical phase to satisfy the requirements of Case 1 to Case 4. The PZT is assembled on a linear translation stage to change the external cavity at different locations. The photodiode (PD) packaged at the rear of the LD is connected to a detection circuit to record an OFI signal when varying the PZT. A beam splitter (BS) with a splitting ratio of 50:50 is used to direct a part of light into the fast external photodetector (Thorlabs, PDA8GS) through a fiber port coupler. This fast PD with a bandwidth of 9.5GHz is suitable to capture the transient laser intensity. The OFI signal and transient laser intensity are finally captured and displayed in a fast oscilloscope (Tektronix DSA 70804) with a maximum sampling rate of 25GHz and analog bandwidth of 8GHz.

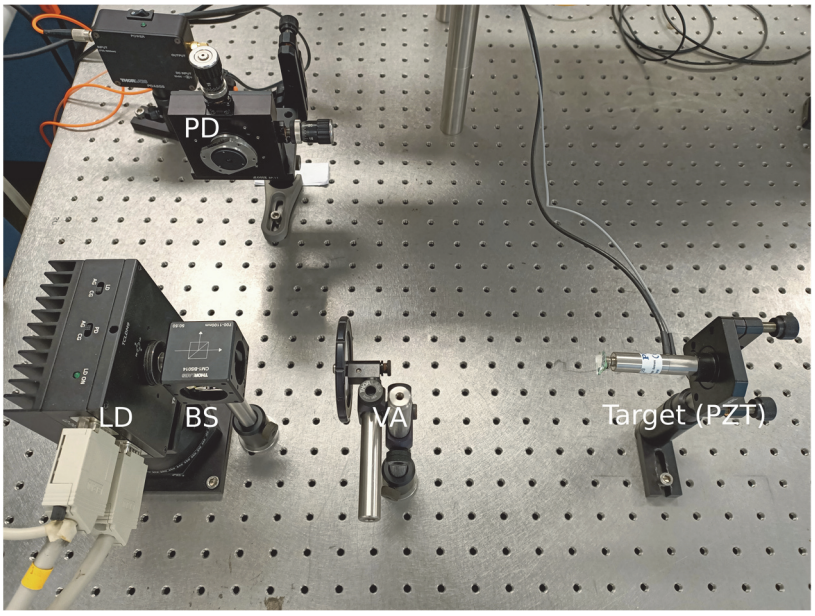

Fig. 4.4: Experimental setup.

Following the simulation test procedure described in Section 4.2, we choose 6 different locations for the PZT target, with the external cavity length varying from 0.15m to 0.155m. For each location, we adjust the external cavity length by linearly moving the PZT with ΔL in a few wavelengths through the control voltage applied on the PZT (denoted by V_{PZT}). Note that in our experiment, each 0.1V of the V_{PZT} corresponds to 27nm travel length of the PZT. Fig. 4.5(a) shows the control signal applied on the PZT and Fig. 4.5(b) is the corresponding OFI signal. After signal processing on the raw experimental signals, we are able to determine the locations for Case 1 to Case 4. We then set the LD working under quasi-continuous wave (QCW) mode. Through using the method in [161], the transient laser intensity can be captured by using the external fast photodetector and oscilloscope. Fig. 4.6 shows one of the experimental signals for the transient laser intensity. We apply digital signal processing on the raw experimental signal and make the signal clearer. Then, the period of the transient laser intensity can be measured to get the required RO frequency.

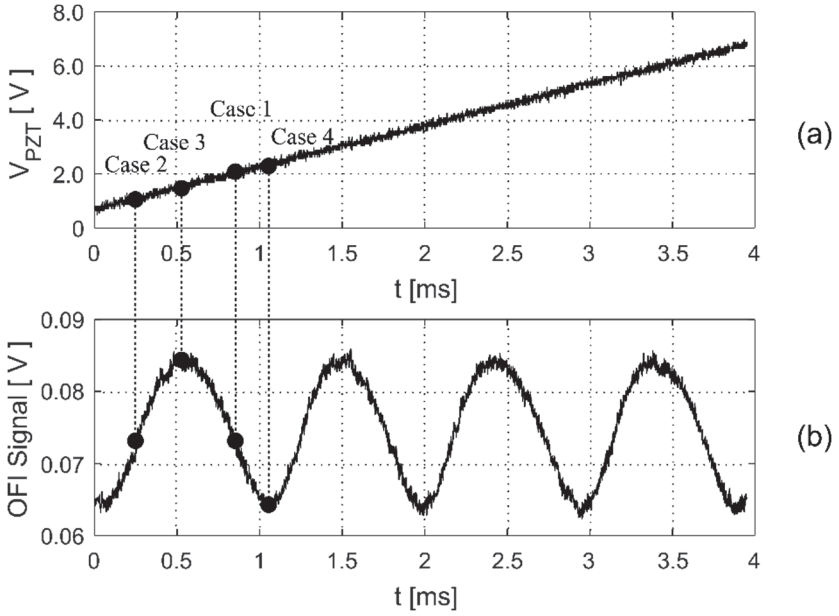

Fig. 4.5: Experimental results. (a) Control signal applied on PZT. (b) Corresponding OFI signal.

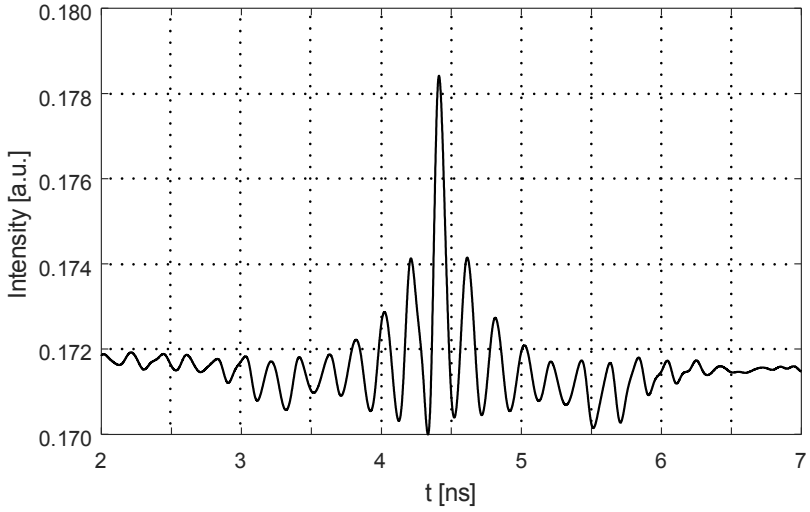

Fig. 4.6: Transient laser intensity under QCW mode.

The experimental data and calculated result of α are presented in Table 4-7 and Table 4-8. For method 1 and method 2, the RO frequencies of the four cases are recorded at the beginning of the experiment when $L = 0.15m$. Using Eq.(4.20), Eq.(4.21) and Eq.(4.28), the α for method 1 is $\alpha = 3.14$, for method 2 is $\alpha = 2.76$. For method 3, the required two RO frequencies at 6 different locations are recorded in Table 4-8.

Table 4-7: Experimental results for method 1 and method 2.

$f_{RO\text{-}zero} = 4.751, f_{RO1} = 4.631, f_{RO2} = 4.878, f_{RO3} = 4.697, f_{RO4} = 4.771$	
Method 1	$\alpha = 3.14$
Method 2	$\alpha = 2.76$

Table 4-8: Experimental results for method 3.

L (cm)	15.0	15.1	15.2	15.3	15.4	15.5
f_{RO1} (GHz)	4.631	4.645	4.659	4.669	4.687	4.701
f_{RO2} (GHz)	4.697	4.702	4.708	4.709	4.717	4.725
$f_{RO\text{-}zero}$ (GHz)	4.751					
$S_1 = 0.139, S_2 = 0.053,\ \alpha = 2.62.$						

Based on these values the relationship between f_{RO} and L for the two cases are shown in Fig. 4.7 with line fitting. Note, we use the relative RO frequencies difference as expressed in Eq.(4.29) and Eq.(4.30), where $f_{RO\text{-}zero} = 4.751\ GHz$. The gradients S_1 and S_2 of the two lines are respectively 0.139 for case 1 and 0.053 for case 2. According to Eq.(4.31), we obtain that α factor for the LD used in our experiment is 2.62. We also measure α factor under different laser operation condition, i.e. injection current $J = 30\text{mA}$, $T = 25 \pm 0.01^{\circ}C$, in this case we get $\alpha = 2.75$. Since there is no a commercial measurement device for α, thus we do not have a true value of α to justify our measured value. However, we can verify our results using the method in [76]. For the same LD, we applied the method presented in [76] with $J = 35\text{mA}$, $T = 23 \pm 0.01^{\circ}C$ and $L_0 = 0.15\text{m}$ under moderate feedback regime, it gives $\alpha = 2.89$ which is close to the result obtained by our proposed method.

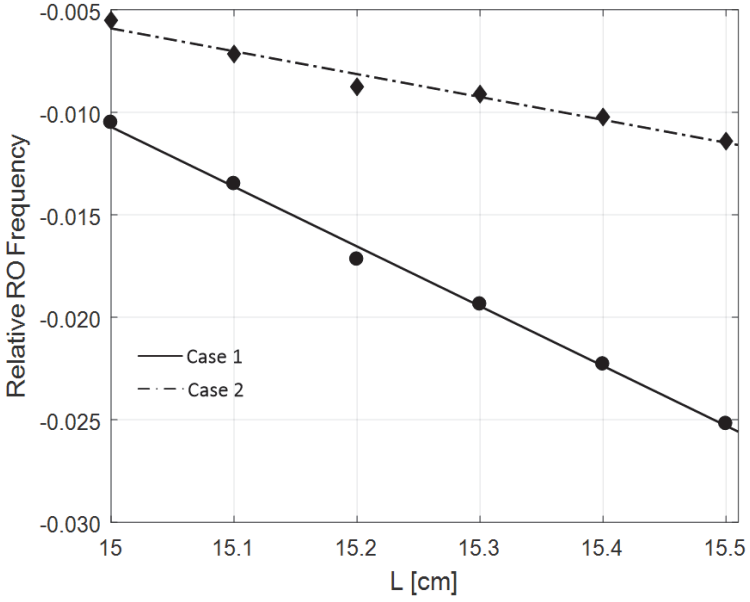

Fig. 4.7: Fitting curves of the experimental results.

4.4. Summary

The RO frequency of a laser can be modified by external optical feedback. Based on this fact, we investigated the relation between the RO frequency and α factor and presented three new methods for the measurement. We derived three measurement formulas showing that α can be determined by only using the RO frequencies, without needing to know any internal or external parameters associated with the laser. The proposed methods are verified by simulations. The results show the overall error for method 1 is 3.22%, method 2 is 4.25% and method 3 is 3.85%. This results show an improvement compare to the method presented in [80]. An experiment was built to measure the α in particle condition. Since there is no a commercial measurement device for α, we compare our value aginst the method in [76] for the same type of LD. This work has the advantages that it does not need the external target to have a symmetric reciprocate movement and it does not rely on analysis the OFI waveform. In addition, the RO can be observed in many

types of lasers, therefore, the proposed methods are not limited to semiconductor lasers. The work in this chapter has contribution a journal publication [162].

Chapter 5. Conclusion

The lasers diodes (LD) experiencing external optical feedback are known to demonstrate complex dynamics, which unveil new and unexpected behavior. While the dynamics may give rise to negative effect on the LD performance, it also enables many applications. For example, a class of laser interferometry called optical feedback interferometry (OFI) can be implemented utilizing such external optical feedback effect in an LD. As a promising non-contact sensing technology, OFI has attracted extensive research in recent decades due to its merits of minimum part-count scheme, low cost in implementation and ease in optical alignment. Various OFI-based sensing applications have been reported, including measurement of displacement, velocity, vibration, laser related parameters, thickness, mechanical resonance, etc. Recently, OFI based sensing has been extended for imaging, material parameter measurement, near-field microscopy, chaotic radar, acoustic detection, biomedical applications etc.

The thesis presented a set of novel work with the aim to improve the performance and/or to broaden the application areas of OFI, by investigating the rich dynamics of LD under various level of optical back and selections of system parameters associated with the OFIs. The contributions of this thesis are summarized as below:

1. The dual-cavity OFI system was proposed and investigated to improve the performance of OFI. In contrast to the conventional single-cavity OFI system, a second cavity is added to control the operation of the LD, while the target to be measured (i.e., the first cavity) remains unchanged. In a similar way for working out the single-cavity OFI model, a dual-cavity OFI model was derived from the

steady state solutions of the dual-cavity LK equations. A mathematic expression was obtained to describe the enhancement of the sensing signal, which also elaborates the way to enhance the signal by controlling the feedback strength and the length of the second cavity. Computer simulations were also conducted and the results shows that the OFI signals from the dual-cavity OFI are identical in their waveform to the signals from the single-cavity OFI systems when they are normalized into the same range. The results also show that the signal can be enhanced with the increase in the feedback strength of the second target. However such relationship does not exist for the second cavity length. Also, it was found that the second cavity length needs to be adjusted with care for the system to achieve maximal OFI signal enhancement. The experiment results show that, with the adjustment of the feedback strength of the second target and its cavity length, the dual-cavity OFI can achieve 2-5 times sensitivity improvement compare to the single-cavity OFI. Therefore, the proposed dual-cavity OFI system addressed the issue that a single cavity OFI system degrades its sensitivity due to the weak optical feedback associated with the target. In other words, the dual cavity OFI provides a novel structure for OFI based sensors, which are advantageous by strong sensing signals. This not only leads to significant improvement in the sensing performance, but also broaden the applications of OFI systems.

Publication: [J2], [C3]

2. The OFI model and their applications are based on an assumption that the system operates in stable state. With the changes of the system parameters, the system will leave the steady state, entering other states and exhibits complicated

dynamics. In this case, the OFI model will not be able to correctly describe the signal anymore. We investigated the validity of both LK equations and the OFI model. In the study, we presented a bifurcation diagram that consists both dynamic states and optical feedback regimes. Base on such bifurcation diagram, we further classified the operation of a LD into five regions:

a. In Region I, the LD is in steady state and with weak feedback.
b. Region II refers to the case that the LD is in steady state and with moderate feedback.
c. In Region III: LD is in P1 state and with moderate feedback.
d. Region IV: LD is in P1 state and with strong feedback.
e. Region V: LD is in qusi-periodic or chaos state and with strong feedback.

The above classification allows us to clearly identify how the states and regimes are corresponded. We performed three group of simulations in each of the five regions. The first two groups compared the waveforms generated using OFI model and LK equations. The results show both models are only valid in Region I and Region II. When the optical feedback is high, the two models give very different waveforms. The third group simulation shows when a low-pass filter was applied on the waveforms that is obtained using LK equations, they will be same as the one generated by OFI model. The third simulation reflected a practical condition, where the observed waveforms under the high optical feedback may have been filtered due to the limited bandwidth of the internal PD. An experiment was conducted by observing the waveforms through the inbuilt PD and external PD. The results show a good agreement with the third simulation. The study of the validity of OFI model and LK equations provide a guidance on applying

appropriate models when designing OFI based sensing system.

Publication: [C10]

3. Based on the work above, we present a new sensing scheme that makes use of laser dynamics in dual-cavity OFI system. The second cavity is used to control the laser dynamics and ensure the LD operates at P1. The laser intensity in the P1 state exhibits an oscillation with its amplitude modulated by an OFI signal (generated with a single cavity and LD operating at steady state). It is observed that the modulation depth is remarkably larger than the magnitude of the OFI signal. By adjusting the feedback strength, the system can be set at a most optimal working point for sensing and measurement and it does need the requirement of an accurate adjustment of control cavity length. The results show the sensitivity can be improved up to 268 time in theory (based on simulations) and 50 time improvement in the experimental observation.

   Publication: [J1], [J5], [J4], [C2], [C4], [C8], [C9]

4. A new approach for fringe sub-division using the characteristic of the dual-cavity OFI signal in P1 state was proposed. It utilized the high frequency in the laser intensity signal and through signal processing technique in the time-domain to achieve a sub-nanometre scale displacement sensing. The simulation results show the displacement resolution can reach up to 0.003 nm for an LD with 780nm wavelength. The experimental results show the system can reach 0.006 nm for an LD with 830nm wavelength. It is expected the resolution could be further increased if a higher frequency laser intensity signal is generated in the dual-cavity

OFI system.

Publication: [C1]

5. Finally, we studied the α factor measurement by making use of the RO frequency of a laser. Based on investigations on the relationship between the RO frequency and α factor, we presented three new methods for the measurement. We derived three measurement formulas showing that α can be determined by only using the RO frequencies, without needing to know any internal or external parameters associated with the laser. The proposed methods are verified by simulations and the results are consistent over the three methods, that is, overall error is 3.22% for method 1, 4.25% for method 2 and 3.85% for method 3. This work has the advantages that it does not need the external target to have a symmetric reciprocate movement and it does not rely on analysis the OFI waveform. In addition, the RO can be observed in many types of lasers, therefore, the proposed methods are not limited to semiconductor lasers. Publication: [J3][C4][C7]

References

[1] C. Hilsum and P. G. R. King, "Some demonstrations of the properties of optical masers," *Contemporary Physics,* vol. 4, no. 6, pp. 435-444, 1963/08/01 1963.

[2] R. F. Broom, "Self modulation at gigahertz frequencies of a diode laser coupled to an external cavity," *Electronics Letters,* vol. 5, no. 23, pp. 571-572, 1969.

[3] R. Broom, E. Mohn, C. Risch, and R. Salathe, "Microwave self-modulation of a diode laser coupled to an external cavity," *IEEE Journal of Quantum Electronics,* vol. 6, no. 6, pp. 328-334, 1970.

[4] R. Lang, "Injection locking properties of a semiconductor laser," *IEEE Journal of Quantum Electronics,* vol. 18, no. 6, pp. 976-983, 1982.

[5] C. Henry and R. Kazarinov, "Instability of semiconductor lasers due to optical feedback from distant reflectors," *IEEE Journal of Quantum Electronics,* vol. 22, no. 2, pp. 294-301, 1986.

[6] W. Way, "Large signal nonlinear distortion prediction for a single-mode laser diode under microwave intensity modulation," *Journal of Lightwave Technology,* vol. 5, no. 3, pp. 305-315, 1987.

[7] G. Yabre and J. L. Bihan, "Reduction of nonlinear distortion in directly modulated semiconductor lasers by coherent light injection," *IEEE Journal of Quantum Electronics,* vol. 33, no. 7, pp. 1132-1140, 1997.

[8] C. Browning *et al.*, "Performance improvement of 10Gb/s direct modulation OFDM by optical injection using monolithically integrated discrete mode lasers," *Optics Express,* vol. 19, no. 26, pp. B289-B294, 2011/12/12 2011.

[9] M. C. Soriano, J. García-Ojalvo, C. R. Mirasso, and I. Fischer, "Complex photonics: Dynamics and applications of delay-coupled semiconductors lasers," *Reviews of Modern Physics,* vol. 85, no. 1, pp. 421-470, 03/20/ 2013.

[10] A. Bogatov, P. Eliseev, L. Ivanov, A. Logginov, M. Manko, and K. Senatorov, "Study of the single-mode injection laser," *IEEE Journal of Quantum Electronics,* vol. 9, no. 2, pp. 392-394, 1973.

[11] C. Voumard, R. Salathé, and H. Weber, "Resonance amplifier model describing diode lasers coupled to short external resonators," *Applied physics,* vol. 12, no. 4, pp. 369-378, 1977/04/01 1977.

[12] C. Risch and C. Voumard, "Self‐pulsation in the output intensity and spectrum of GaAs‐AlGaAs cw diode lasers coupled to a frequency‐selective external optical cavity," *Journal of Applied Physics,* vol. 48, no. 5, pp. 2083-2085, 1977.

[13] D. M. Kane and K. A. Shore, *Unlocking Dynamical Diversity: Optical Feedback Effects on Semiconductor Lasers*. Wiley, 2005.

[14] Y. Mitsuhashi, J. Shimada, and S. Mitsutsuka, "Voltage change across the self-coupled semiconductor laser," *IEEE Journal of Quantum Electronics,* vol. 17, no. 7, pp. 1216-1225, 1981.

[15] S. Donati, "Laser interferometry by induced modulation of cavity field," *Journal of Applied Physics,* vol. 49, no. 2, pp. 495-497, 1978.

[16] P. J. de Groot and G. M. Gallatin, "Backscatter-modulation velocimetry with an external-cavity laser diode," *Optics Letters,* vol. 14, no. 3, pp. 165-167, 1989/02/01 1989.

[17] A. Seko, Y. Mitsuhashi, T. Morikawa, J. Shimada, and K. Sakurai, "Self‐quenching in semiconductor lasers and its applications in optical memory readout," *Applied Physics Letters,* vol. 27, no. 3, pp. 140-141, 1975.

[18] V. M. Gordienko *et al.*, "Autodyne effect in the presence of laser-induced hydrodynamic flows and its use in identification of the type of biotissue in the course of its destruction," *Quantum Electronics,* vol. 26, no. 10, pp. 846-847, 1996/10/31 1996.

[19] K. Petermann, "External optical feedback phenomena in semiconductor lasers," *IEEE Journal of Selected Topics in Quantum Electronics,* vol. 1, no. 2, pp. 480-489, 1995.

[20] G. Giuliani, M. Norgia, S. Donati, and T. Bosch, "Laser diode self-mixing technique for sensing applications," *Journal of Optics A: Pure and Applied Optics,* vol. 4, no. 6, p. S283, 2002.

[21] K. Panajotov, M. Sciamanna, M. A. Arteaga, and H. Thienpont, "Optical Feedback in Vertical-

Cavity Surface-Emitting Lasers," *IEEE Journal of Selected Topics in Quantum Electronics,* vol. 19, no. 4, pp. 1700312-1700312, 2013.
[22] O. Spitz, J. Wu, M. Carras, C.-W. Wong, and F. Grillot, "Chaotic optical power dropouts driven by low frequency bias forcing in a mid-infrared quantum cascade laser," *Scientific Reports,* vol. 9, no. 1, p. 4451, 2019/03/14 2019.
[23] B.-B. Zhao, X.-G. Wang, J. Zhang, and C. Wang, "Relative intensity noise of a mid-infrared quantum cascade laser: insensitivity to optical feedback," *Optics Express,* vol. 27, no. 19, pp. 26639-26647, 2019/09/16 2019.
[24] J. von Staden, T. Gensty, W. Elsäßer, G. Giuliani, and C. Mann, "Measurements of the α factor of a distributed-feedback quantum cascade laser by an optical feedback self-mixing technique," *Optics Letters,* vol. 31, no. 17, pp. 2574-2576, 2006/09/01 2006.
[25] R. P. Green *et al.*, "Linewidth enhancement factor of terahertz quantum cascade lasers," *Applied Physics Letters,* vol. 92, no. 7, p. 071106, 2008.
[26] K. Bertling *et al.*, "Demonstration of the self-mixing effect in interband cascade lasers," *Applied Physics Letters,* vol. 103, no. 23, p. 231107, 2013.
[27] K. M. Manfred, G. A. D. Ritchie, N. Lang, J. Röpcke, and J. H. v. Helden, "Optical feedback cavity-enhanced absorption spectroscopy with a 3.24 μm interband cascade laser," *Applied Physics Letters,* vol. 106, no. 22, p. 221106, 2015.
[28] D. Han, M. Wang, and J. Zhou, "Self-Mixing Speckle in an Erbium-Doped Fiber Ring Laser and Its Application to Velocity Sensing," *IEEE Photonics Technology Letters,* vol. 19, no. 18, pp. 1398-1400, 2007.
[29] S. Blaize *et al.*, "Phase sensitive optical near-field mapping using frequency-shifted laser optical feedback interferometry," *Optics Express,* vol. 16, no. 16, pp. 11718-11726, 2008/08/04 2008.
[30] X. Dai, M. Wang, Y. Zhao, and J. Zhou, "Self-mixing interference in fiber ring laser and its application for vibration measurement," *Optics Express,* vol. 17, no. 19, pp. 16543-16548, 2009/09/14 2009.
[31] K. Otsuka, K. Abe, J.-Y. Ko, and T.-S. Lim, "Real-time nanometer-vibration measurement with a self-mixing microchip solid-state laser," *Optics Letters,* vol. 27, no. 15, pp. 1339-1341, 2002/08/01 2002.
[32] Y. Tan, S. Zhang, S. Zhang, Y. Zhang, and N. Liu, "Response of microchip solid-state laser to external frequency-shifted feedback and its applications," *Scientific Reports,* vol. 3, no. 1, p. 2912, 2013/10/09 2013.
[33] L. Mashal, R. M. Nguimdo, G. V. d. Sande, M. C. Soriano, J. Danckaert, and G. Verschaffelt, "Low-Frequency Fluctuations in Semiconductor Ring Lasers With Optical Feedback," *IEEE Journal of Quantum Electronics,* vol. 49, no. 9, pp. 790-797, 2013.
[34] M. Khoder, G. V. d. Sande, J. Danckaert, and G. Verschaffelt, "Effect of External Optical Feedback on Tunable Micro-Ring Lasers Using On-Chip Filtered Feedback," *IEEE Photonics Technology Letters,* vol. 28, no. 9, pp. 959-962, 2016.
[35] F. Grillot, C.-Y. Lin, N. A. Naderi, M. Pochet, and L. F. Lester, "Optical feedback instabilities in a monolithic InAs/GaAs quantum dot passively mode-locked laser," *Applied Physics Letters,* vol. 94, no. 15, p. 153503, 2009.
[36] D. Arsenijević, M. Kleinert, and D. Bimberg, "Phase noise and jitter reduction by optical feedback on passively mode-locked quantum-dot lasers," *Applied Physics Letters,* vol. 103, no. 23, p. 231101, 2013.
[37] S. Donati, "Developing self‐mixing interferometry for instrumentation and measurements," *Laser & Photonics Reviews,* vol. 6, no. 3, pp. 393-417, 2012.
[38] T. Taimre, M. Nikolić, K. Bertling, Y. L. Lim, T. Bosch, and A. D. Rakić, "Laser feedback interferometry: a tutorial on the self-mixing effect for coherent sensing," *Advances in Optics and Photonics,* vol. 7, no. 3, pp. 570-631, 2015/09/30 2015.
[39] S. Xiang, W. Pan, L. Yan, B. Luo, N. Jiang, and L. Yang, "Polarization properties of vertical-cavity surface-emitting lasers subject to feedback with variably rotated polarization angle," *Applied Optics,* vol. 48, no. 27, pp. 5176-5183, 2009/09/20 2009.
[40] W. Chen, S. Zhang, and X. Long, "Angle measurement with laser feedback instrument," *Optics Express,* vol. 21, no. 7, pp. 8044-8050, 2013/04/08 2013.
[41] S. Donati, D. Rossi, and M. Norgia, "Single Channel Self-Mixing Interferometer Measures Simultaneously Displacement and Tilt and Yaw Angles of a Reflective Target," *IEEE Journal of Quantum Electronics,* vol. 51, no. 12, pp. 1-8, 2015.
[42] K. Li, F. Cavedo, A. Pesatori, C. Zhao, and M. Norgia, "Balanced detection for self-mixing

interferometry," *Optics Letters,* vol. 42, no. 2, pp. 283-285, 2017/01/15 2017.
[43] M. Norgia, G. Giuliani, and S. Donati, "Absolute distance measurement with improved accuracy using laser diode self-mixing interferometry in a closed loop," *Instrumentation and Measurement, IEEE Transactions on,* vol. 56, no. 5, pp. 1894-1900, 2007.
[44] D. Guo and M. Wang, "Self-mixing interferometry based on a double-modulation technique for absolute distance measurement," *Applied optics,* vol. 46, no. 9, pp. 1486-1491, 2007.
[45] K. Kou, X. Li, L. Li, H. Li, and T. Wu, "Absolute distance estimation with improved genetic algorithm in laser self-mixing scheme," *Optics & Laser Technology,* vol. 68, pp. 113-119, 2015/05/01/ 2015.
[46] M. Norgia, D. Melchionni, and A. Pesatori, "Self-mixing instrument for simultaneous distance and speed measurement," *Optics and Lasers in Engineering,* vol. 99, pp. 31-38, 2017.
[47] S. Merlo and S. Donati, "Reconstruction of displacement waveforms with a single-channel laser-diode feedback interferometer," *IEEE journal of quantum electronics,* vol. 33, no. 4, pp. 527-531, 1997.
[48] M. Norgia, S. Donati, and D. D'Alessandro, "Interferometric measurements of displacement on a diffusing target by a speckle tracking technique," *IEEE Journal of quantum electronics,* vol. 37, no. 6, pp. 800-806, 2001.
[49] Y. Fan, Y. Yu, J. Xi, and J. F. Chicharo, "Improving the measurement performance for a self-mixing interferometry-based displacement sensing system," *Applied Optics,* vol. 50, no. 26, pp. 5064-5072, 2011/09/10 2011.
[50] K. Zhu, B. Guo, Y. Lu, S. Zhang, and Y. Tan, "Single-spot two-dimensional displacement measurement based on self-mixing interferometry," *Optica,* vol. 4, no. 7, pp. 729-735, 2017/07/20 2017.
[51] D. Guo, Y. Yu, L. Kong, W. Xia, and M. Wang, "Self-Mixing Grating Interferometer With Dual Laser Diodes for Sensing of 2-D Dynamic Displacement," *IEEE Journal of Quantum Electronics,* vol. 54, no. 5, pp. 1-6, 2018.
[52] G. Plantier, N. Servagent, A. Sourice, and T. Bosch, "Real-time parametric estimation of velocity using optical feedback interferometry," *IEEE Transactions on Instrumentation and Measurement,* vol. 50, no. 4, pp. 915-919, 2001.
[53] G. Plantier, N. Servagent, T. Bosch, and A. Sourice, "Real-time tracking of time-varying velocity using a self-mixing laser diode," *IEEE Transactions on Instrumentation and Measurement,* vol. 53, no. 1, pp. 109-115, 2004.
[54] J. Albert *et al.*, "Laser Doppler velocimetry with polarization-bistable VCSELs," *IEEE Journal of Selected Topics in Quantum Electronics,* vol. 10, no. 5, pp. 1006-1012, 2004.
[55] M. Norgia, A. Pesatori, and L. Rovati, "Self-mixing laser Doppler spectra of extracorporeal blood flow: a theoretical and experimental study," *IEEE Sensors Journal,* vol. 12, no. 3, pp. 552-557, 2012.
[56] S. Wu *et al.*, "All-Fiber Configuration Laser Self-Mixing Doppler Velocimeter Based on Distributed Feedback Fiber Laser," *Sensors,* vol. 16, no. 8, p. 1179, 2016.
[57] L. Scalise and N. Paone, "Laser Doppler vibrometry based on self-mixing effect," (in English), *Optics and Lasers in Engineering,* vol. 38, no. 3-4, pp. 173-184, Sep-Oct 2002.
[58] Q. Zhang and X. Su, "High-speed optical measurement for the drumhead vibration," *Optics express,* vol. 13, no. 8, pp. 3110-3116, 2005.
[59] U. Zabit, F. Bony, T. Bosch, and A. D. Rakic, "A self-mixing displacement sensor with fringe-loss compensation for harmonic vibrations," *IEEE Photonics Technology Letters,* vol. 22, no. 6, pp. 410-412, 2010.
[60] U. Zabit, O. D. Bernal, T. Bosch, and F. Bony, "MEMS accelerometer embedded in a self-mixing displacement sensor for parasitic vibration compensation," *Optics Letters,* vol. 36, no. 5, pp. 612-614, 2011/03/01 2011.
[61] V. Annovazzi-Lodi, M. Benedetti, S. Merlo, and M. Norgia, "Spot optical measurements on micromachined mirrors for photonic switching," *IEEE Journal of selected topics in quantum electronics,* vol. 10, no. 3, pp. 536-544, 2004.
[62] M. T. Fathi and S. Donati, "Thickness measurement of transparent plates by a self-mixing interferometer," *Optics Letters,* vol. 35, no. 11, pp. 1844-1846, 2010/06/01 2010.
[63] Y. Niu, H. Niu, N. Liu, and J. Li, "KTP crystal thickness distribution measurements based on laser feedback interferometry," *Applied Optics,* vol. 53, no. 19, pp. 4195-4199, 2014/07/01 2014.
[64] J. Kitching, A. Yariv, and Y. Shevy, "Room Temperature Generation of Amplitude Squeezed Light from a Semiconductor Laser with Weak Optical Feedback," *Physical Review Letters,* vol.

74, no. 17, pp. 3372-3375, 04/24/ 1995.
[65] J. Al Roumy, J. Perchoux, Y. L. Lim, T. Taimre, A. D. Rakić, and T. Bosch, "Effect of injection current and temperature on signal strength in a laser diode optical feedback interferometer," *Applied Optics,* vol. 54, no. 2, pp. 312-318, 2015/01/10 2015.
[66] L. Xu, S. Zhang, Y. Tan, and L. Sun, "Simultaneous measurement of refractive-index and thickness for optical materials by laser feedback interferometry," *Review of Scientific Instruments,* vol. 85, no. 8, p. 083111, 2014.
[67] P. J. Caber, "Interferometric profiler for rough surfaces," *Applied optics,* vol. 32, no. 19, pp. 3438-3441, 1993.
[68] J. Herbert, K. Bertling, T. Taimre, A. D. Rakić, and S. Wilson, "Surface roughness characterisation using optical feedback interferometry," *Electronics Letters*, vol. 53, no. 4, pp. 268-270
[69] M. Suleiman, H. C. Seat, and T. Bosch, "Interrogation of fiber Bragg grating dynamic strain sensors by self-mixing interferometry," *IEEE Sensors journal,* vol. 8, no. 7, pp. 1317-1323, 2008.
[70] M. Dabbicco, A. Intermite, and G. Scamarcio, "Laser-Self-Mixing Fiber Sensor for Integral Strain Measurement," *Journal of Lightwave Technology,* vol. 29, no. 3, pp. 335-340, 2011/02/01 2011.
[71] B. H. Lee *et al.*, "Interferometric Fiber Optic Sensors," *Sensors,* vol. 12, no. 3, pp. 2467-2486, 2012.
[72] K. Lin *et al.*, "A Fiber-Coupled Self-Mixing Laser Diode for the Measurement of Young's Modulus," *Sensors,* vol. 16, no. 6, p. 928, 2016.
[73] G. Giuliani and M. Norgia, "Laser diode linewidth measurement by means of self-mixing interferometry," *IEEE Photonics Technology Letters,* vol. 12, no. 8, pp. 1028-1030, 2000.
[74] K. E. Chlouverakis, K. M. Al-Aswad, I. D. Henning, and M. J. Adams, "Determining laser linewidth parameter from Hopf bifurcation minimum in lasers subject to optical injection," *Electronics Letters,* vol. 39, no. 16, pp. 1185-1187, 2003.
[75] M. C. Cardilli, M. Dabbicco, F. P. Mezzapesa, and G. Scamarcio, "Linewidth measurement of mid infrared quantum cascade laser by optical feedback interferometry," *Applied Physics Letters,* vol. 108, no. 3, p. 031105, 2016/01/18 2016.
[76] Y. Yu, G. Giuliani, and S. Donati, "Measurement of the linewidth enhancement factor of semiconductor lasers based on the optical feedback self-mixing effect," *Photonics Technology Letters, IEEE,* vol. 16, no. 4, pp. 990-992, 2004.
[77] Y. Yu, J. Xi, J. F. Chicharo, and T. Bosch, "Toward Automatic Measurement of the Linewidth-Enhancement Factor Using Optical Feedback Self-Mixing Interferometry With Weak Optical Feedback," *IEEE Journal of Quantum Electronics,* vol. 43, no. 7, pp. 527-534, 2007.
[78] L. Wei, J. Xi, Y. Yu, and J. F. Chicharo, "Linewidth enhancement factor measurement based on optical feedback self-mixing effect: a genetic algorithm approach," *Journal of Optics A: Pure and Applied Optics,* vol. 11, no. 4, p. 045505, 2009.
[79] Y. Yu and J. Xi, "Influence of external optical feedback on the alpha factor of semiconductor lasers," *Optics Letters,* vol. 38, no. 11, pp. 1781-1783, 2013/06/01 2013.
[80] Y. Fan, Y. Yu, J. Xi, G. Rajan, Q. Guo, and J. Tong, "Simple method for measuring the linewidth enhancement factor of semiconductor lasers," *Applied Optics,* vol. 54, no. 34, pp. 10295-10298, 2015/12/01 2015.
[81] S. Holzinger *et al.*, "Determining the linewidth enhancement factor via optical feedback in quantum dot micropillar lasers," *Optics Express,* vol. 26, no. 24, pp. 31363-31371, 2018/11/26 2018.
[82] B. Liu *et al.*, "Laser Self-Mixing Fiber Bragg Grating Sensor for Acoustic Emission Measurement," *Sensors,* vol. 18, no. 6, p. 1956, 2018.
[83] Y. Zhu, L. Hu, Z. Liu, and M. Han, "Ultrasensitive ultrasound detection using an intracavity phase-shifted fiber Bragg grating in a self-injection-locked diode laser," *Optics Letters,* vol. 44, no. 22, pp. 5525-5528, 2019/11/15 2019.
[84] R. Kliese, Y. L. Lim, T. Bosch, and A. D. Rakić, "GaN laser self-mixing velocimeter for measuring slow flows," *Optics letters,* vol. 35, no. 6, pp. 814-816, 2010.
[85] H. Ukita, Y. Uenishi, and Y. Katagiri, "Applications of an extremely short strong-feedback configuration of an external-cavity laser diode system fabricated with GaAs-based integration technology," *Applied optics,* vol. 33, no. 24, pp. 5557-5563, 1994.
[86] C. H. Lu, J. Wang, and K. L. Deng, "Imaging and profiling surface microstructures with noninterferometric confocal laser feedback," *Applied physics letters,* vol. 66, no. 16, pp. 2022-2024, 1995.
[87] B. Zhou, Z. Wang, X. Shen, L. Zhang, and Y. Tan, "High-sensitivity laser confocal tomography

based on frequency-shifted feedback technique," *Optics and Lasers in Engineering,* vol. 129, p. 106059, 2020/06/01/ 2020.
[88] S. Donati and M. Sorel, "A phase-modulated feedback method for testing optical isolators assembled into the laser diode package," *IEEE Photonics Technology Letters,* vol. 8, no. 3, pp. 405-407, 1996.
[89] T. Bosch, N. Servagent, R. Chellali, and M. Lescure, "Three-dimensional object construction using a self-mixing type scanning laser range finder," *IEEE Transactions on Instrumentation and Measurement,* vol. 47, no. 5, pp. 1326-1329, 1998.
[90] P. Dean *et al.*, "Terahertz imaging through self-mixing in a quantum cascade laser," *Optics Letters,* vol. 36, no. 13, pp. 2587-2589, 2011/07/01 2011.
[91] K. Bertling *et al.*, "Imaging of acoustic fields using optical feedback interferometry," *Optics Express,* vol. 22, no. 24, pp. 30346-30356, 2014/12/01 2014.
[92] X. Sun, H. Wang, B. Liu, and Y. Yu, "Measurement of microsurface topography using a self-mixing optical configuration," *Optical Engineering,* vol. 57, no. 5, p. 051503, 2018.
[93] M. B. Spencer and W. E. Lamb, "Laser with a Transmitting Window," *Physical Review A,* vol. 5, no. 2, pp. 884-892, 02/01/ 1972.
[94] R. Lang and K. Kobayashi, "External optical feedback effects on semiconductor injection laser properties," *IEEE Journal of Quantum Electronics,* vol. 16, no. 3, pp. 347-355, 1980.
[95] B. Tromborg, J. Osmundsen, and H. Olesen, "Stability analysis for a semiconductor laser in an external cavity," *IEEE Journal of Quantum Electronics,* vol. 20, no. 9, pp. 1023-1032, 1984.
[96] B. Liu, Y. Yu, J. Xi, Q. Guo, J. Tong, and R. A. Lewis, "Displacement sensing using the relaxation oscillation frequency of a laser diode with optical feedback," *Applied Optics,* vol. 56, no. 24, pp. 6962-6966, 2017/08/20 2017.
[97] K. Petermann, *Laser diode modulation and noise / K. Petermann*. Dordrecht ; Boston : Tokyo : Norwell, MA :: Kluwer Academic Publishers ; KTK Scientific Publishers ; Sold and distributed in the U.S.A. and Canada by Kluwer Academic Publishers, 1988.
[98] W. Wang, K. T. Grattan, A. Palmer, and W. Boyle, "Self-mixing interference inside a single-mode diode laser for optical sensing applications," *Journal of Lightwave Technology,* vol. 12, no. 9, pp. 1577-1587, 1994.
[99] S. Donati, G. Giuliani, and S. Merlo, "Laser diode feedback interferometer for measurement of displacements without ambiguity," *IEEE Journal of Quantum Electronics,* vol. 31, no. 1, pp. 113-119, 1995.
[100] G. Acket, D. Lenstra, A. D. Boef, and B. Verbeek, "The influence of feedback intensity on longitudinal mode properties and optical noise in index-guided semiconductor lasers," *IEEE Journal of Quantum Electronics,* vol. 20, no. 10, pp. 1163-1169, 1984.
[101] R. Tkach and A. Chraplyvy, "Regimes of feedback effects in 1.5-μm distributed feedback lasers," *Journal of Lightwave Technology,* vol. 4, no. 11, pp. 1655-1661, 1986.
[102] S. Donati and R. Horng, "The Diagram of Feedback Regimes Revisited," *IEEE Journal of Selected Topics in Quantum Electronics,* vol. 19, no. 4, pp. 1500309-1500309, 2013.
[103] M. Wang, "Fourier transform method for self-mixing interference signal analysis," *Optics & Laser Technology,* vol. 33, no. 6, pp. 409-416, 2001.
[104] D. Guo, M. Wang, and S. Tan, "Self-mixing interferometer based on sinusoidal phase modulating technique," *Optics express,* vol. 13, no. 5, pp. 1537-1543, 2005.
[105] G. Plantier, C. Bes, and T. Bosch, "Behavioral model of a self-mixing laser diode sensor," *IEEE Journal of Quantum Electronics,* vol. 41, no. 9, pp. 1157-1167, 2005.
[106] C. Bes, G. Plantier, and T. Bosch, "Displacement measurements using a self-mixing laser diode under moderate feedback," *IEEE Transactions on Instrumentation and Measurement,* vol. 55, no. 4, pp. 1101-1105, 2006.
[107] Y. Yu, J. Xi, J. F. Chicharo, and T. M. Bosch, "Optical Feedback Self-Mixing Interferometry With a Large Feedback Factor C: Behavior Studies," *Quantum Electronics, IEEE Journal of,* vol. 45, no. 7, pp. 840-848, 2009.
[108] I. Fischer, O. Hess, W. Elsäβer, and E. Göbel, "High-Dimensional Chaotic Dynamics of an External Cavity Semiconductor Laser," *Physical Review Letters,* vol. 73, no. 16, pp. 2188-2191, 10/17/ 1994.
[109] L. Yun and J. Ohtsubo, "Dynamics and chaos stabilization of semiconductor lasers with optical feedback from an interferometer," *IEEE Journal of Quantum Electronics,* vol. 33, no. 7, pp. 1163-1169, 1997.
[110] F. Rogister, P. Mégret, O. Deparis, M. Blondel, and T. Erneux, "Suppression of low-frequency

fluctuations and stabilization of a semiconductor laser subjected to optical feedback from a double cavity:?theoretical results," *Optics Letters,* vol. 24, no. 17, pp. 1218-1220, 1999/09/01 1999.
[111] M. Wang and G. Lai, "A self-mixing interferometer using an external dual cavity," *Measurement Science and Technology,* vol. 14, no. 7, pp. 1025-1031, 2003/06/17 2003.
[112] S. Huang *et al.*, "Dual-cavity feedback assisted DFB narrow linewidth laser," *Scientific Reports,* vol. 7, no. 1, p. 1185, 2017/04/26 2017.
[113] C. Jiang, Y. Geng, Y. Liu, Y. Liu, P. Chen, and S. Yin, "Rotation velocity measurement based on self-mixing interference with a dual-external-cavity single-laser diode," *Applied Optics,* vol. 58, no. 3, pp. 604-608, 2019/01/20 2019.
[114] Y. Geng, C. Jiang, and L. Kan, "Enhanced laser self-mixing Doppler velocity measurement with pre-feedback mirror," *Applied Optics,* vol. 58, no. 27, pp. 7571-7576, 2019/09/20 2019.
[115] L. Lu, W. Zhang, B. Yang, J. Zhou, H. Gui, and B. Yu, "Dual-Channel Self-Mixing Vibration Measurement System in a Linear Cavity Fiber Laser," *IEEE Sensors Journal,* vol. 13, no. 11, pp. 4387-4392, 2013.
[116] F. P. Mezzapesa, L. L. Columbo, M. Dabbicco, M. Brambilla, and G. Scamarcio, "QCL-based nonlinear sensing of independent targets dynamics," *Optics Express,* vol. 22, no. 5, pp. 5867-5874, 2014/03/10 2014.
[117] J. Chen, H. Zhu, W. Xia, D. Guo, H. Hao, and M. Wang, "Self-mixing birefringent dual-frequency laser Doppler velocimeter," *Optics Express,* vol. 25, no. 2, pp. 560-572, 2017/01/23 2017.
[118] F. P. Mezzapesa *et al.*, "Nanoscale Displacement Sensing Based on Nonlinear Frequency Mixing in Quantum Cascade Lasers," *IEEE Journal of Selected Topics in Quantum Electronics,* vol. 21, no. 6, pp. 107-114, 2015.
[119] W. Zhu, Q. Chen, Y. Wang, H. Luo, H. Wu, and B. Ma, "Improvement on vibration measurement performance of laser self-mixing interference by using a pre-feedback mirror," *Optics and Lasers in Engineering,* vol. 105, pp. 150-158, 2018/06/01/ 2018.
[120] S. Zhang, Y. Hu, J. Cao, S. Zhang, and Q. Hao, "Effect of dual-channel optical feedback on self-mixing interferometry system," *Journal of Optics,* vol. 21, no. 2, p. 025502, 2019/01/11 2019.
[121] Y. Ruan, B. Liu, Y. Yu, J. Xi, Q. Guo, and J. Tong, "Improving Measurement Sensitivity for a Displacement Sensor Based on Self-Mixing Effect," *IEEE Photonics Journal,* vol. 10, no. 6, pp. 1-10, 2018.
[122] L. Scalise, Y. Yanguang, G. Giuliani, G. Plantier, and T. Bosch, "Self-mixing laser diode velocimetry: application to vibration and velocity measurement," *IEEE Transactions on Instrumentation and Measurement,* vol. 53, no. 1, pp. 223-232, 2004.
[123] O. D. Bernal, U. Zabit, and T. M. Bosch, "Robust Method of Stabilization of Optical Feedback Regime by Using Adaptive Optics for a Self-Mixing Micro-Interferometer Laser Displacement Sensor," *IEEE Journal of Selected Topics in Quantum Electronics,* vol. 21, no. 4, pp. 336-343, 2015.
[124] S.-C. Chan, S.-K. Hwang, and J.-M. Liu, "Period-one oscillation for photonic microwave transmission using an optically injected semiconductor laser," *Optics Express,* vol. 15, no. 22, pp. 14921-14935, 2007.
[125] C. Cui and S.-C. Chan, "Performance analysis on using period-one oscillation of optically injected semiconductor lasers for radio-over-fiber uplinks," *IEEE Journal of Quantum Electronics,* vol. 48, no. 4, pp. 490-499, 2012.
[126] L. Fan *et al.*, "Subharmonic Microwave Modulation Stabilization of Tunable Photonic Microwave Generated by Period-One Nonlinear Dynamics of an Optically Injected Semiconductor Laser," *Journal of Lightwave Technology,* vol. 32, no. 23, pp. 4660-4666, 2014.
[127] L. Li, X. Yi, S. X. Chew, S. Song, L. Nguyen, and R. A. Minasian, "Double-pass microwave photonic sensing system based on low-coherence interferometry," *Optics Letters,* vol. 44, no. 7, pp. 1662-1665, 2019/04/01 2019.
[128] B. Liu, Y. Ruan, Y. Yu, Q. Guo, J. Xi, and J. Tong, "Modeling for optical feedback laser diode operating in period-one oscillation and its application," *Optics Express,* vol. 27, no. 4, pp. 4090-4104, 2019/02/18 2019.
[129] S. D. Cohen, A. Aragoneses, D. Rontani, M. Torrent, C. Masoller, and D. J. Gauthier, "Multidimensional subwavelength position sensing using a semiconductor laser with optical feedback," *Optics letters,* vol. 38, no. 21, pp. 4331-4334, 2013.
[130] V. Annovazzi-Lodi, S. Merlo, M. Norgia, and A. Scirè, "Characterization of a chaotic telecommunication laser for different fiber cavity lengths," *IEEE journal of quantum electronics,* vol. 38, no. 9, pp. 1171-1177, 2002.

[131] M. Sciamanna and K. A. Shore, "Physics and applications of laser diode chaos," *Nature Photonics,* Review Article vol. 9, p. 151, 02/27/online 2015.
[132] A. Zhao, N. Jiang, S. Liu, C. Xue, and K. Qiu, "Wideband Time Delay Signature-Suppressed Chaos Generation Using Self-Phase-Modulated Feedback Semiconductor Laser Cascaded With Dispersive Component," *Journal of Lightwave Technology,* vol. 37, no. 19, pp. 5132-5139, 2019.
[133] A. Uchida, *Optical Communication with Chaotic Lasers: Applications of Nonlinear Dynamics and Synchronization*. 2012, pp. 206-208.
[134] R. Teysseyre, F. Bony, J. Perchoux, and T. Bosch, "Laser dynamics in sawtooth-like self-mixing signals," *Optics Letters,* vol. 37, no. 18, pp. 3771-3773, 2012/09/15 2012.
[135] B. Liu *et al.*, "Features of a Self-Mixing Laser Diode Operating Near Relaxation Oscillation," *Sensors,* vol. 16, no. 9, p. 1546, 2016.
[136] N. Servagent, F. Gouaux, and T. Bosch, "Measurements of displacement using the self-mixing interference in a laser diode," (in English), *Journal of Optics-Nouvelle Revue D Optique,* Article vol. 29, no. 3, pp. 168-173, Jun 1998.
[137] M. Wang and G. M. Lai, "Displacement measurement based on Fourier transform method with external laser cavity modulation," (in English), *Review of Scientific Instruments,* Article vol. 72, no. 8, pp. 3440-3445, Aug 2001.
[138] D. M. Guo, M. Wang, and S. Q. Tan, "Self-mixing interferometer based on sinusoidal phase modulating technique," (in English), *Optics Express,* Article vol. 13, no. 5, pp. 1537-1543, Mar 2005.
[139] D. Choi, M. J. Wishon, E. Viktorov, D. Citrin, and A. Locquet, "Nanometric sensing with laser feedback interferometry," *Optics letters,* vol. 44, no. 4, pp. 903-906, 2019.
[140] F. J. Azcona, R. Atashkhooei, S. Royo, J. M. Astudillo, and A. Jha, "A Nanometric Displacement Measurement System Using Differential Optical Feedback Interferometry," *IEEE Photonics Technology Letters,* vol. 25, no. 21, pp. 2074-2077, 2013.
[141] Y. Tan, W. Wang, C. Xu, and S. Zhang, "Laser confocal feedback tomography and nano-step height measurement," *Scientific reports,* vol. 3, p. 2971, 2013.
[142] S. Pullteap, H.-C. Seat, and T. Bosch, "Modified fringe-counting technique applied to a dual-cavity fiber Fabry-Pérot vibrometer," *Optical Engineering,* vol. 46, no. 11, p. 115603, 2007.
[143] X. Cheng and S. Zhang, "Intensity modulation of VCSELs under feedback with two reflectors and self-mixing interferometer," *Optics Communications,* vol. 272, no. 2, pp. 420-424, 2007/04/15/ 2007.
[144] Y. Ruan, B. Liu, Y. Yu, J. Xi, Q. Guo, and J. Tong, "High sensitive sensing by a laser diode with dual optical feedback operating at period-one oscillation," *Applied Physics Letters,* vol. 115, no. 1, p. 011102, 2019.
[145] M. W. Fleming and A. Mooradian, "Fundamental line broadening of single ‐ mode (GaAl)As diode lasers," *Applied Physics Letters,* vol. 38, no. 7, pp. 511-513, 1981.
[146] C. Henry, "Theory of the linewidth of semiconductor lasers," *IEEE Journal of Quantum Electronics,* vol. 18, no. 2, pp. 259-264, 1982.
[147] M. Osinski and J. Buus, "Linewidth broadening factor in semiconductor lasers--An overview," *Quantum Electronics, IEEE Journal of,* vol. 23, no. 1, pp. 9-29, 1987.
[148] T. Fordell and A. M. Lindberg, "Experiments on the Linewidth-Enhancement Factor of a Vertical-Cavity Surface-Emitting Laser," *IEEE Journal of Quantum Electronics,* vol. 43, no. 1, pp. 6-15, 2007.
[149] Z. Toffano, A. Destrez, C. Birocheau, and L. Hassine, "New linewidth enhancement determination method in semiconductor lasers based on spectrum analysis above and below threshold," *Electronics Letters,* vol. 28, no. 1, pp. 9-11, 1992.
[150] S. Barland, P. Spinicelli, G. Giacomelli, and F. Marin, "Measurement of the working parameters of an air-post vertical-cavity surface-emitting laser," *IEEE Journal of Quantum Electronics,* vol. 41, no. 10, pp. 1235-1243, 2005.
[151] T. Fordell, Z. Toffano, and M. L. s, "A Vertical-Cavity Surface-Emitting Laser at Threshold," *IEEE Photonics Technology Letters,* vol. 18, no. 21, pp. 2263-2265, 2006.
[152] M. Bagheri, M. H. Shih, S. J. Choi, J. D. O. Brien, and P. D. Dapkus, "Microcavity Laser Linewidth Close to Threshold," *IEEE Journal of Quantum Electronics,* vol. 45, no. 8, pp. 945-949, 2009.
[153] K. Kikuchi, "Lineshape measurement of semiconductor lasers below threshold," *IEEE Journal of Quantum Electronics,* vol. 24, no. 9, pp. 1814-1817, 1988.
[154] T. Chattopadhyay, P. Bhattacharyya, and C. Ghosh, "Linewidth Enhancement Factor

Measurement of a Fabry Perot Laser Diode through Narrowband Optical FM Generation," in *Journal of Optical Communications* vol. 38, ed, 2017, p. 141.

[155] R. Hui, A. Mecozzi, A. D. Ottavi, and P. Spano, "Novel measurement technique of alpha factor in DFB semiconductor lasers by injection locking," *Electronics Letters,* vol. 26, no. 14, pp. 997-998, 1990.

[156] K. Iiyama, K.-i. Hayashi, and Y. Ida, "Simple method for measuring the linewidth enhancement factor of semiconductor lasers by optical injection locking," *Optics Letters,* vol. 17, no. 16, pp. 1128-1130, 1992/08/15 1992.

[157] A. Thorette, M. Romanelli, and M. Vallet, "Linewidth enhancement factor measurement based on FM-modulated optical injection: application to rare-earth-doped active medium," *Optics Letters,* vol. 42, no. 8, pp. 1480-1483, 2017/04/15 2017.

[158] J. Xi, Y. Yu, J. Chicharo, and T. Bosch, "Estimating the parameters of semiconductor lasers based on weak optical feedback self-mixing interferometry," *Quantum Electronics, IEEE Journal of,* vol. 41, no. 8, pp. 1058-1064, 2005.

[159] Y. Yu, G. Giuliani, and S. Donati, "Measurement of the linewidth enhancement factor of semiconductor lasers based on the optical, feedback self-mixing effect," *Ieee Photonics Technology Letters,* vol. 16, no. 4, pp. 990-992, APR 2004 2004.

[160] E. Lacot, R. Day, and F. Stoeckel, "Coherent laser detection by frequency-shifted optical feedback," *Physical Review A,* vol. 64, no. 4, p. 043815, 09/19/ 2001.

[161] D. M. Kane and J. P. Toomey, "Precision Threshold Current Measurement for Semiconductor Lasers Based on Relaxation Oscillation Frequency," *Journal of Lightwave Technology,* vol. 27, no. 15, pp. 2949-2952, 2009/08/01 2009.

[162] Y. Ruan, B. Liu, Y. Yu, J. Xi, Q. Guo, and J. Tong, "Measuring Linewidth Enhancement Factor by Relaxation Oscillation Frequency in a Laser with Optical Feedback," *Sensors,* vol. 18, no. 11, p. 4004, 2018.